ADAPTIVE OPTICS IMAGING OF THE TEMPORAL RAPHE IN NORMAL AND GLAUCOMATOUS SUBJECTS

Gang Huang

Submitted to the faculty of the University Graduate School

in partial fulfillment of the requirements

for the degree

Doctor of Philosophy

in the School of Optometry,

Indiana University

June 2015

Accepted by the Graduate faculty, Indiana University,

in partial fulfillment of the requirements for the degree

Doctor of Philosophy

Doctoral Committee

_____

Stephen A. Burns, Ph.D., Chair

_____

Ann E. Elsner, Ph.D.

_____

Donald T. Miller, Ph.D.

_____

Andrew J. Hanson, Ph.D.

30 June 2014

Acknowledgements

One of the joys of completion is to look over the journey past and remember all the friends and family who have helped and supported me along this long but fulfilling road.

I would like to express my sincere gratitude to my advisor Dr. Stephen Burns for his support throughout my Ph.D study. I was given considerable freedom to pursue my own research interests. Meanwhile, he shared with me his vision, and provided guidance and resources necessary for me to proceed through all the projects and complete my Ph.D dissertation.

I would also like to express my appreciation to Dr. Donald Miller, Dr.Ann Elsner, and Dr. Andrew Hason. I thank them for all the constructive comments as well as their efforts and expertise that lead to the completion of the thesis.

My sincere thanks also go to Dr. Williams Swanson, who is an expert in the area of glaucoma research, for his exemplary guidance throughout the glaucoma studies in Chapter 4 and 5. I would like to thank him for all the discussions of these projects, from their earliest stages through their completion.

I am also very grateful to Dr. Thomas Gast. As an experienced ophthalmologist, he offered valuable clinical insights into my projects, and provided thoughtful feedbacks on experiment designs and data analysis. As a colleague, his enthusiasm and warm interest for my projects encouraged me to stay positive and optimistic throughout my projects.

I would like to thank all my fellow lab members: Dr. Xiaofeng Qi, Ting Luo, Jake Hillard, Dr. Lucie Sawides, Dr. Alberto de Castro Arribas, and the lab alumni including Dr. Zhangyi Zhong, Dr. Weiyao Zou, Dr. Hongxin Song, and Dr. Toco Chui, for all the assistance and collaborations in the past few years. Acknowledge also goes to Mr. William Monette and Tom Kemerly, who are engineers in the machine shop of Optometry School, for all their help in the past few years.

I also want to thank my fellow students in the Vision Science/Physiological Optics program for all the help and friendship. Many of them voluntarily participated in my experiments, offering valuable control data. Outside the school, hanging out with them and their families was one of my happiest memories of my staying in Bloomington.

Finally, I would like to thank my parents, Zhong Huang and Huiduan Zeng, for their support in all my pursuits. It was their love that helped me get through difficult times. I feel extremely lucky and blessed to have them as my parents. I owe them everything and wish I could show them just how much I love and appreciate them.

Gang Huang

ADAPTIVE OPTICS IMAGING OF THE TEMPORAL RAPHE IN NORMAL AND GLAUCOMATOUS SUBJECTS

Adaptive optics scanning laser ophthalmoscopy (AOSLO) allows high-resolution *in vivo* imaging of the retina. It provides us a new way to observe and measure the RNFL *in vivo*. Especially, it opens a possibility of imaging the RNFL in the temporal raphe which can be affected in early glaucoma.

The main objective of this thesis is to use an AOSLO to observe and measure the RNFL in the temporal raphe in both normal and glaucomatous subjects. To do this, we first improved the AOSLO imaging with the following efforts: 1) A novel adaptive optics (AO) image processing algorithm was developed to improve the contrast of AO images. 2) A clinical planning module was developed to enhance the data acquisition efficiency, especially for large-scale RNFL imaging. With the improved AOSLO imaging, we investigated the temporal raphe in young healthy subjects. Moreover, we evaluated changes of the RNFL in the temporal retina between patients with glaucoma and age-similar controls.

The results shed light on the generalization that has been drawn about the retinal anatomy. We found that the temporal raphe was not a perfect horizontal dividing line. Its angle varied between individuals but was related to the optic disc position. The angle between the temporal raphe and the line that connects the fovea and the center of optic

disc was about 170 degrees on average.

The temporal raphe changed with aging and glaucoma. Aging increased the separation between nerve fiber bundles in superior and inferior retina, forming a larger gap in the temporal raphe in AO images. In glaucomatous subjects, this gap significantly increased even when the corresponding local visual-field loss was relatively mild. A bundle index, which integrates information about the density and relative reflectivity of nerve fiber bundles, also decreased in glaucomatous subjects.

The thesis demonstrated that AOSLO imaging can elucidate the normal anatomy of the temporal raphe *in vivo*, and the AOSLO can serve as a tool for understanding individual differences of the temporal raphe. This thesis also opened the possibility of using the temporal raphe as a site for glaucoma research and clinical assessment.

_____
Stephen A. Burns, Ph.D., Chair

_____
Ann E. Elsner, Ph.D.

_____
Donald T. Miller, Ph.D.

_____
Andrew J. Hanson, Ph.D.

Table of Contents

CHAPTER 1: INTRODUCTION

The retinal nerve fiber layer (RNFL) is essential to maintain functionality of the retina in human eyes. The RNFL receives information from other retinal layers, and carries it across the retinal surface and to the brain. Damage to the RNFL can disrupt information transportation, leading to vision loss.

One common retinal disease that affects the RNFL is glaucoma, one of the leading causes of blindness in the industrialized world. There are about 60 million people with glaucoma, and about 8 million people blind as the result of glaucoma (Quigley & Broman, 2006). In spite of its prevalence, our understanding of glaucoma is still limited, posing challenges to the detection and management of glaucoma in clinics.

A RNFL region that could help advance our understanding of glaucoma is the temporal raphe, which is an anatomical boundary between the superior and inferior sides of the temporal retina. The raphe's geometry relative to other parts of the RNFL is fundamental to understanding of the relation of glaucomatous damage between various retinal regions. The raphe also has an advantage for studying early structural and functional loss in glaucoma because it is believed to be one of the major sites where early visual function abnormalities appear. However, imaging of the raphe *in vivo* is not possible with regular clinical imaging approaches.

In this thesis, we develop adaptive optics scanning laser ophthalmoscopy (AOSLO) techniques to image the raphe *in vivo*, and compare the RNFL difference between healthy and glaucomatous eyes. The following part of this chapter is divided into six parts: 1) anatomy of the RNFL and optic disc, 2) visual field of human eyes, 3) primary open angle glaucoma (POAG), 4) structural and functional measures for evaluation of POAG and 5) scope of thesis.

1.1 Anatomy of the RNFL and optic disc

1.1.1 The RNFL

The RNFL is mainly composed of retinal ganglion cell axons which can be also referred to as nerve fibers. The size of individual axons can range from 0.2 μm to 3 μm in diameter (Ogden, 1984). As axons extend further away from the ganglion cells, they are gradually grouped into individual nerve fiber bundles. The small bundles are grouped to large bundles as they extend towards the optic disc, where all the bundles converge and proceed through the eye wall and to the brain. Near the optic disc, the diameter of individual bundles could reach more than 35 μm (Takayama et al., 2012).

Nerve fibers and bundles form a unique pattern on the retina, as indicated in Fig. 1. In the temporal retina, inferior and superior retinal hemispheres are separated by a boundary,

referred to as the temporal raphe. All the fibers from the temporal retina travel above or below the macular region, joining the fibers of superior and inferior retina and forming larger and larger bundles as they course into the optic disc. They eventually enter the disc on its superior or inferior side. In the nasal retina between the fovea and temporal side of the optic disc, the fibers are oriented in an approximately horizontal pattern and reach to the temporal side of the disc. They are usually referred to as the papillomacular bundle. In the retina region that is nasal to the disc, the fibers are organized in an approximately radial fashion.

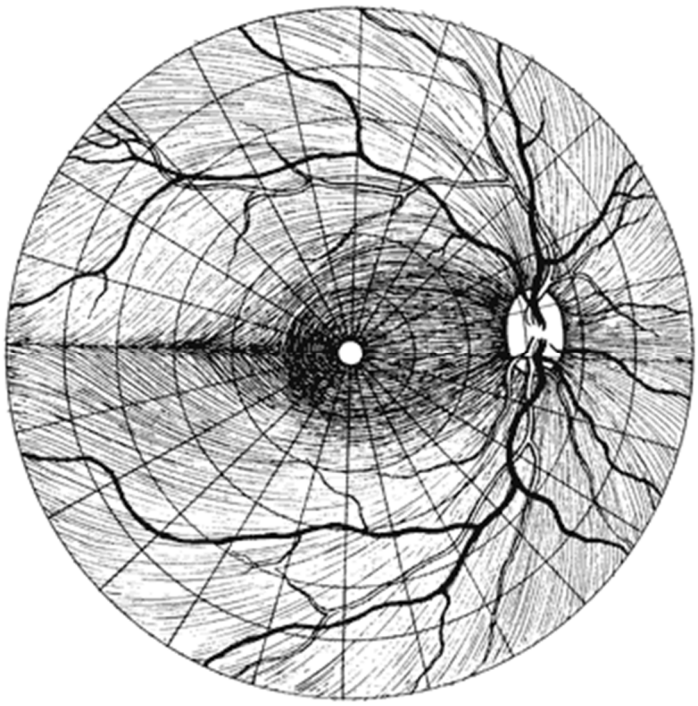

Figure 1. Illustration of the retinal nerve fiber pattern in the human eye (Harrington DO, 1990). The white circle in the center represents the fovea, the center of the retina. Its surround region is macular region. The region left to the fovea is the temporal retina, and the horizontal midline is the

temporal raphe. The white oval on the right is the optic disc. The curved bundles between the fovea and disc are papillomacular bundles.

Besides nerve fibers, there are two other major components in the RNFL: blood vessels and glial cells. The vessels maintain the basic nutritional supply to the RNFL. Glial cells have three types: Muller cells, astrocytes, and microglial cells. The Muller cells stretch across layers of the entire retina, providing both architectural support and physiological support for the specialized neurons. In the RNFL, the end feet of the Muller cells separate the nerve fiber bundles, appearing as dark bands in the RNFL when viewed histologically (Radius & Anderson, 1979). Astrocytes originate in the central nervous system (CNS). They enter the eye during the development of the optic nerve (Chan-Ling & Stone, 1991; Stone & Dreher, 1987). In the RNFL, it is found that astrocytes, as well as blood vessels, surround the surface of individual nerve fiber bundles (Trivino, Ramirez, Salazar, Ramirez, & Garcia-Sanchez, 1996). They exhibit significant homeostatic interaction with nerve fibers and bundles. For instance, they can provide the energy support to axons. The last type of glial cells, the microglia, is the macrophage of the retina. Its function is to phagocytose degenerating cells in the RNFL and other layers.

The thickness of the RNFL varies with locations. At the disc margin, the thickness can reach to 300 μm. The thickness decreases with distance from the optic disc. In the temporal retina, the thickness is minimal near the temporal raphe and in the far peripheral retina. The averaged thickness in the raphe is less than 30 μm (Hood et al., 2012). The

thickness is majorly contributed by axons, but histology shows that the proportion of glial cells within a given bundle was never less than 18%, and on average it was 20-30% (Ogden, 1983).

The RNFL thickness also varies with aging. The average decay rate of the thickness is 0.16 μm per year around the disc margin (Parikh et al., 2007). This can be explained by the loss of ganglion cells and their axons with the aging. The decay rate in healthy subject is estimated as 5000 cells per year (Balazsi, Rootman, Drance, Schulzer, & Douglas, 1984).

1.1.2 Optic Disc

The optic disc, also referred to as the optic nerve head, is the place where all the retinal ganglion cell axons leave the eye. Within the disc, the superficial portion, called the prelaminar region, is comprised primarily of nerve fiber bundles and astrocytes. The central part of the prelaminar region usually contains a depression that lacks axons and appears as a cup in its cross-sectional anatomical image. This is formed by the geometry of axons' convergence upon the disc. Beneath the prelaminar region, the axons go through a mesh-like structure, called the lamina cribrosa. It is a multilayered connective tissue consisting largely of collagen fibers. These fibers form numerous small pores which function as the tunnels for passage of axonal bundles. The central pores of the lamina cribrosa also allow the central retinal artery and vein to enter and leave the eye. Below the lamina cribrosa is generally defined as the retrolaminar region where the

astrocytes decrease and axons become myelinated and are surrounded by connective tissue septa rather than pores.

The size of optic disc is highly variable between individuals. In general, the disc appears as an oval when examined by ophthalmoscopy. The vertical diameter is typically larger than the horizontal diameter. The short diameter can range from 0.85 mm to 2.43 mm and the longer one can vary from 1.21 to 2.86 mm (Jonas, Gusek, Guggenmoos-Holzmann, & Naumann, 1988), or on average 1.77 mm horizontally and 1.88 mm vertically (Quigley, Brown, Morrison, & Drance, 1990). The disc area can vary from 0.68 to 4.42 mm^2 (Jonas et al., 1988; Jonas, Mardin, & Grundler, 1998; Ramrattan, Wolfs, Jonas, Hofman, & de Jong, 1999). This high individual variability is a major limitation when disc appearance is used to diagnose glaucoma.

1.2 Visual field of human eyes

The field of vision for a given eye is defined as the area perceived when the eye is fixating on a single point. The normal field of vision is not symmetric in different directions. Generally, it is 60° in the superior field, 75° in the inferior field, 110° temporally, and 60° nasally from the point of fixation.

The visual sensitivity is usually defined as the minimum luminance of the light that can produce a visual sensation on top of a uniform background luminance. The

sensitivity changes across the field of vision. Typically, it is highest in the central vision and gradually drops in locations further from the central region, and falls abruptly at the peripheral limits. Within the normal field, there is a deep depression defined as the blind spot, which anatomically corresponds to the optic disc where there is no photoreceptor cell and therefore no light response can be produced.

1.3 Primary open angle glaucoma (POAG)

Glaucoma is not a single disease process but a group of optic neuropathies that result in a loss of retinal ganglion cells and impaired visual function. It is often classified into several subtypes based on our current understanding of glaucoma's etiology and mechanisms: angle-closure glaucoma, developmental glaucoma, secondary glaucoma, normal-tension glaucoma and primary open-angle glaucoma (POAG). Among them, POAG draws most attention in the research of glaucoma. This is because, although it represents more than 50% of glaucoma cases (Allingham, 2005), it develops slowly, often going for years without patients' noticing and without clinicians detecting it on regular eye exams.

1.3.1 POAG clinical pathologies

In clinics, the pathologies of POAG can be classified into two types: structural and functional pathologies. The structural pathologies typically include the morphological

changes in the optic disc and RNFL. The function defects are usually referred to visual sensitivity defects in the field of vision as determined by the perimetry.

1.3.1.1 Functional pathology

The variation in detectability of light as a function of visual angle is defined as a visual-field profile. Statistically significant deviations from the normative visual field are referred to as visual field defects. In POAG, there are two defect measures that are commonly computed: diffuse depressions of the visual field and localized defects. Diffuse depression of the visual field results from a widespread reduction of sensitivity and may reflect diffuse loss of the axons in the RNFL.

Localized defects are of more importance to the current work, since they are typically caused by localized damage to retinal ganglion cells and/or their axons. There are various forms of localized defects. One that is related to the current work is the nasal step. This is an asymmetry defect across the temporal raphe, indicating asymmetric loss of nerve fiber bundles in the superior and inferior hemispheres. The width of the nasal step also varies. The nasal step frequently occurs in association with other field defects, but it can also occur in isolation.

Nasal steps can be observed in early glaucoma. In one longitudinal study (Werner & Drance, 1977), nasal steps were involved in more than 50% of the earliest defects in POAG. Another study (Hart & Becker, 1982) found a similar result in 98 eyes where

54% of glaucomatous eyes were found to have nasal steps.

1.3.1.2 Structural pathology

An optic disc with glaucoma is characterized by an enlarged cupping due to the loss of the axons. The ratio of the cup diameter in the vertical direction to the disc diameter is defined as vertical-cup-to-disc-ratio (VCDR), which has been widely used in the diagnosis and follow-up of glaucoma suspects. The higher the ratio, the worse the glaucoma condition is. A VCDR of 0.7 is regarded as the upper limit of normal population (Wolfs et al., 2000) .

RNFL changes in glaucoma are quantified by RNFL thickness. Typically, the thickness of the RNFL is measured along a circular path around the optic disc and compared to the normative values. Glaucomatous eyes often show significant reduction in RNFL thickness compared to normal eyes (Schuman et al., 1995).

1.4 Structural and functional measures for evaluation of POAG

Monitoring and evaluating POAG's pathology relies upon measures that can either test the visual function or image the retina or both. Generally, the measures can be divided into two categories: 1) visual field testing for functional measurements 2) optical imaging techniques for structural measurements

1.4.1 Visual Field testing

The history of the visual field testing started about more than 2000 years ago, when Hippocrates observed and described the hemianopsia that is characteristic of the decreased vision in half of the visual field. Since then, the technique was gradually improved and eventually evolved into automated perimetry (Johnson, Wall, & Thompson, 2011), which is widely used in clinics nowadays.

There are two major types of automated perimetry: kinetic and static perimetry. In kinetic perimetry, a stimulus is moved from a non-seeing area to a seeing area. The location where the stimulus is first seen is recorded. The procedure is repeated along different sets of meridians, usually spaced every 15°, with the use of the same stimulus. By connecting these locations, an isopter (line of constant sensitivity) is defined. The luminance and the size of the target are changed to plot other isopters. All these isopters build up a field of vision and can be compared to the normal field of vision. In static perimetry, the retinal sensitivity at specific locations is recorded, forming a map of visual sensitivity of the retina.

The most common implementation of static perimetry is the standard automated perimetry (SAP). In its protocol, a white spot is used as a stimulus. The typical size of the stimulus spot is 0.43 degrees in diameter, often referred to as a Goldmann-Three target. The stimulus of SAP is presented on a white background and can be placed at

various retinal locations. For each location, the testing algorithm can adjust the intensity of the spot to find the intensity level that can be detected 50% of the time by the subject. The sensitivity on that location is then defined as the ratio of the threshold luminance to the background, recorded in logarithmic units or decibels (DB). The procedures are repeated based on a testing position map. The most common map is the 24-2 program in which the 54 different retinal locations are tested. The locations are uniformly distributed over a 24-degree-radius region centered at the fovea. The locations are spaced uniformly at 6 degree intervals. Once all the local sensitivities are measured, they form a visual field map for the retina.

1.4.2 Retinal Imaging Techniques

In vivo retinal imaging techniques plays an essential role in evaluation of structural pathology of the retina *in vivo*. Currently, the majority of these techniques are based on optical imaging principle. In this section, we will review these optical imaging techniques, especially those that are commonly used for POAG's detection and management.

1.4.2.1 Important parameters of human eyes relevant to optical retinal imaging

Most of retinal imaging techniques use the anterior part of the eye as the final objective and system aperture. Therefore, physical properties of the eye can affect retinal imaging

quality and image analysis in many ways. In the following paragraphs, we will discuss three factors that are related to this thesis.

First, the pupil, located right behind the cornea of the eye and seen as the aperture of a retinal imaging system, can influence imaging quality with its size. The pupil size can vary approximately between 2mm and 8mm, depending mainly on the ambient light luminance as well as other physiological factors (Winn, Whitaker, Elliott, & Phillips, 1994). A larger pupil could improve the image quality mainly because it improves higher numerical aperture and higher-resolution in all three dimensions. For example, providing an 8 mm pupil without any ocular aberration, an 830-nm laser beam of 8 mm in diameter can get focused into a 2 μm spot on the retina, capable of imaging single cone photoreceptors in the retina. However, in reality, a large pupil always comes with increasing optical aberrations and could degrade the resolution of the image. This side-effect can be reduced with adaptive optics techniques and will be discussed in details in section 1.4.2.4.

Second, aging process of the eye indirectly degrades imaging quality by compromising the functionality of components of the eye. As the eye ages, the ocular media in front of the retina is less transparent to the light, for example, the cataract development of the lens of the eye. The opacity of the media can cause more absorption or scattering of the light, and thus lower the signal to noise ratio of the retinal images.

The aging process can also affect the pupil's response to degrade the image. The aged eye, on average, shows a much smaller pupil size than a young eye (McLellan, Marcos,

& Burns, 2001; Winn et al., 1994). Even worse, there is a chance that the muscle of the pupil could be harmed during an inappropriate cataract surgery and stop the pupil from dilating, even with the use of mydriatics. This could prevent getting high-resolution images, as discussed above.

Third, the eye is constantly moving, producing distortions and blur in retinal images. Motion during fixation is referred to as 'physiological nystagmus' or 'fixational eye movements'. A typical fixational movement includes three major components: 1) a slow random drift, 2) a periodic rapid micro-saccade movement, with amplitudes in the range of 10 arcmin, 3) tremor, high-frequency component, with amplitudes between 5-40 arcsec, and frequencies observed between 50-100Hz) (Martinez-Conde, Macknik, & Hubel, 2004). These three types of eye movements can cause different blurring effects on high-resolution retinal images (Stevenson SB, 2005b). The slow random movements can cause an imaging field on the retina to be displaced between the images that are obtained in a video-recording sequence. The microsaccade can produce severe distortions even within one single image when the movement occurs. The tremor is too small to be observed in most of retinal images.

1.4.2.2 Confocal Scanning laser ophthalmoscopy (cSLO)

Confocal scanning laser ophthalmoscopy is a retinal imaging technique that can obtain *in vivo* high-contrast *en face* retinal images (Webb, Hughes, & Delori, 1987). In cSLO imaging, a laser beam is focused and scanned on the *en face* plane of the retina.

The scattered light from each position, after passing through an optics pinhole, is collected by a detector and registered into a two-dimensional retinal image based on the time sequence. There are two key features in this imaging scheme: the optical sectioning capability and the flying-spot-scanning scheme. The optical sectioning ensures the light is only collected from the focal plane and its neighboring regions. The out-of-focus scattered light is greatly suppressed, for instance, the light scattered from the anterior part of the eye. The sectioning is realized by a pinhole, which is placed on the image-conjugate plane to only allow the passage of the light from the focal plane. However, this sectioning ability is always degraded by the ocular aberration (discussed later) and not able to further optically distinguish retinal sub-layers for most of the subjects.

The second feature is using the flying-spot-scanning scheme. At a given time instance, the laser beam only illuminates one spot on the retina and the scattered light can be strictly registered to one pixel in the image, which effectively prevents the optic cross-talking between adjacent pixels.

In the past decades, cSLO has been widely used to help evaluate retinal diseases. The cSLO imaging on the optic disc can evaluate the cupping size and the disc diameter (Cioffi et al., 1993; Weinreb, Shakiba, & Zangwill, 1995). The cSLO combined with the polarization technique can examine the structural regularity of the RNFL and infer the thickness of the RNFL (Weinreb et al., 1995). In recent years, cSLO can be also used as a wide-field *en face* imaging tool to guide other smaller-imaging-field retinal imaging systems (Burns, Tumbar, Elsner, Ferguson, & Hammer, 2007; Ferguson et al., 2010;

Vienola et al., 2012).

1.4.2.3 Optical coherence tomography (OCT).

Optical coherence tomography is a technique that enables *in vivo* high-resolution cross-sectional imaging on the retina (D. Huang et al., 1991). The technique uses the principle of low coherence interferometry to optically section the object in depth. The size of the sectioning in depth is defined as the depth resolution of the system. Most OCT can achieve ~10 μm depth resolution, much better than cSLO. The reflections of the light from different depths are mapped to form a cross-sectional image, always referred to as an 'A-Scan' image. OCT can also obtain B-scan or C scan image by scanning the imaging beam in one or two dimensions on the *en face* plane. With a high-resolution C-scan, OCT can recover the three-dimensional structure of the object.

The retina is actually the first biological tissue that OCT successfully imaged. Since the first retina image captured by OCT was published in 1991 (D. Huang et al., 1991), the power of this new technique has widely been recognized. With OCT, the layers of the retina can be imaged and their thickness can be quantified (Jaffe & Caprioli, 2004; Sakata, Deleon-Ortega, Sakata, & Girkin, 2009). Their associations with various retinal diseases can be studied (Jaffe & Caprioli, 2004).More recently, the technique has been extended from structural measurements to functional measurements (Wang, Bower, Izatt, Tan, & Huang, 2008).

Although OCT has superior depth resolution, its *en face* resolution for the retina is not satisfying, largely due to the slow acquisition speed of OCT. The A-scan speed of a commercial OCT is typically ~20 kHz. To construct a regular 10 by 10 degree wide-field *en face* image, it usually takes minutes to finish. Therefore, it suffers from the eye movements and always requires post-processing to re-register images. This limitation restricts commercial OCT as a useful tool for high-resolution *en face* imaging in real-time.

1.4.2.4 Adaptive Optics (AO) and AO-SLO

Although both cSLO and OCT are able to obtain high-contrast retinal images, their *en face* image resolutions are limited by ocular aberrations. Optical aberrations originate from the anterior part of the eye and can greatly reduce imaging quality. To further improve imaging quality, it is necessary to develop a technique to measure and correct the aberrations.

Adaptive optics is a technique that can measure and correct optical aberrations for an optical system. The most common way is to use a wavefront sensor to measure the aberration, and employ deformable mirrors to correct the aberrations. This technique was introduced to the retina imaging field in 1997, capable of imaging retinal photoreceptors *in vivo* (Liang, Williams, & Miller, 1997). Since that, various retinal imaging techniques have been combined with the AO to image retinal features with high-resolution (Rha et al., 2006; Roorda et al., 2002; Zhang, Rha, Jonnal, & Miller, 2005). For example, the

combination of the AO and SLO technique yields the AO-SLO.

The AO-SLO has been widely used because it can combine the advantages of both techniques, forming high-resolution high signal-to-noise ratio *en face* images. The combination is not just a simple add-up. With the AO, the focusing spot on the retina is much smaller, which makes it possible to use smaller apertures in the SLO part. This further improves the sectioning ability of SLO part, making the AO-SLO able to distinguish different layers of the retina. The RNFL and photoreceptor layers have been successfully imaged in both normal and diseased eyes (Chui, Song, & Burns, 2008; Ooto, Hangai, Takayama, Arakawa, et al., 2011; Ooto, Hangai, Takayama, Sakamoto, et al., 2011; Ooto, Hangai, & Yoshimura, 2011; Park, Chung, Greenstein, Tsang, & Chang, 2013; Takayama et al., 2013). Beside the structure measurements, the AOSLO can be customized to perform function measurements. The combination of AOSLO with the visual field testing make it possible to test the visual sensitivity of single photoreceptor cells (Roorda, 2011).

Despite the great success in retinal imaging, the AOSLO has two major limitations that may prevent it from clinical studies. The first one is the vulnerability to the eye movements. Although the AOSLO images show the information with high-resolution, these details can be distorted by eye movements, making the image quality worse and measurement of the spatial relation on the retina inaccurate (Sahin, Lamory, Levecq, Harms, & Dainty, 2012; Stevenson SB, 2005a). The second limitation is the small field of view. The angle of the imaging field is dependent upon the isoplanatic angle that

defines the maximum extent of the imaging field that can be corrected by AO system without loss of the image quality. The isoplanatic angle for most of the eyes is between 1-2 degrees (Dubinin, 2004), which makes the wide-field imaging more time consuming. Either the subject would be asked to fixate at different targets during the imaging, or the system would be required to enable moving the small imaging field over a larger field. Consequentially, a typical imaging section over a 10 by 10 degree region could last more than 20 minutes. Such a long imaging time further increases the fatigue of the subject, making more frequent eye movements and more fluctuating aberrations, and worsening image quality. In sum, these two limitations bring down the throughput of an AOSLO system, but could be reduced by hardware or software improvements (Ferguson et al., 2010; Yang, Arathorn, Tiruveedhula, Vogel, & Roorda, 2010).

1.5 The relation between the structural and functional measures

1.5.1 Variability of structural and functional measures

The clinical value of measuring the VCDR and RNFL thickness for glaucoma evaluation is limited by large individual differences, even in healthy individuals. For VCDR, there is a large variability of the optic disc size, as well as a the non-linear relation between optic disc size and cupping size (Garway-Heath, Ruben, Viswanathan, & Hitchings, 1998). For the RNFL around the optic disc, its thickness can vary significantly with age, ethnicity, axial length, and optic disc area (Budenz et al., 2007). In addition, there are

concerns about the effect of the non-neuronal components which can add additional variance to thickness measurement. (Hood et al., 2008).

The clinical value of using the visual field for glaucoma evaluation is also limited by large individual variability. For example, the ganglion cell density can vary two-fold between individuals(Curcio & Allen, 1990). Aging can change in optical clarity and neural sensitivity (Johnson, Adams, & Lewis, 1989; Spry & Johnson, 2001), affecting visual sensitivity measurements. Other factors include pupil size (Heuer, Anderson, Feuer, & Gressel, 1989; Lindenmuth, Skuta, Rabbani, Musch, & Bergstrom, 1990), subjective errors including subjects' understanding of the test (Drance, Berry, & Hughes, 1966), his/her fatigue (Hudson, Wild, & O'Neill, 1994), learning effects in the follow-up tests (Heijl & Bengtsson, 1996; Heijl, Lindgren, & Olsson, 1989), and etc.

1.5.2 Combination of structural and functional measures

With all these sources of variability, the sensitivity for glaucoma diagnosis and evaluation with either measure alone is relatively low. One approach of improving the sensitivity is to combine both measures, using evidence from one measure to support the evident from another. Therefore, there has been an increased attention to investigate the relation between the functional and structural measures, which is defined as structure-function relation (Heijl et al., 2002; Kass et al., 2002; Keltner et al., 2006; Leske et al., 2003).

In recent years, people have proposed and validated several models for the structure-

function relation. All the models are based on the assumption that both function and structure measures are measuring the same pathophysiological process in glaucoma, namely the loss of the ganglion cells and their axons, and therefore both measures are expected to be related. At present, there are four quantitative models: The hockey-Stick model (Anderson, 1988), the Drasdo model (Drasdo, Millican, Katholi, & Curcio, 2007; Drasdo, Mortlock, & North, 2008), the Harwerth model (Harwerth, Wheat, Fredette, & Anderson, 2010), and the Hood model (Hood & Kardon, 2007). The first three models all study the relation between the visual sensitivity and ganglion cell numbers. They found that the relation can be linear or non-linear depending on the eccentricities, the severity of damage, etc.. However, these models haven't been tested *in vivo* because there is no direct way of measuring the number of ganglion cells *in vivo*.

The fourth one, the Hood model, investigates the relation between the visual sensitivity and RNFL thickness. This model assumes there is a linear relation between the RNFL thickness loss and visual sensitivity loss, and was tested with data from healthy and glaucomatous subjects. Although the data was generally in agreement with the curve predicted by the model, there is one limitation for this model. That is, to relate local visual field with the corresponding global RNFL thickness around the optic disc, the model employs a map of the RNFL trajectory, which was developed by Garway-Heath (Garway-Heath, Poinoosawmy, Fitzke, & Hitchings, 2000; Jansonius et al., 2009). This map could be affected by anatomical variability of the RNFL trajectory between eyes. In fact, latest evidence has shown that the position of the optic disc relative to the fovea and temporal raphe can influence on the RNFL trajectory (Hood, Raza, de Moraes,

Liebmann, & Ritch, 2013). Therefore, to validate the hood model, a more generic RNFL trajectory map or an individual-based RNFL map is required.

One important part of the RNFL trajectory map is the temporal raphe. Its geometry relative to the fovea and optic disc is key to modelling the function-structure relationship. However, in spite of the progress in optical retinal imaging techniques, the temporal raphe in the human retina hasn't been systematically explored *in vivo*.

1.6 Scope of thesis

The thesis develops new approaches to improve the AOSLO imaging technique, and uses the improved AOSLO imaging technique to explore the effects of aging and glaucoma on the temporal raphe. In particular, we imaged the raphe in young healthy eyes to explore the anatomy of the temporal raphe and its geometry relative to other parts of the retina, and imaged and analyzed differences of the temporal raphe between healthy and glaucomatous conditions in elder eyes.

Chapter2 presents a new image processing approach for generating high-contrast images. The approach uses different image metrics to analyze an AOSLO image stack of the same retina region. The pixels that are least affected by ocular aberrations are chosen and combined into a single image that yields better contrast and resolution. The improvement over the traditional processing method was demonstrated by imaging and analyzing the photoreceptor images of the AOSLO. The details of the processing scheme

have been published (Huang, Zhong, Zou, & Burns, 2011).

Chapter 3 presents a clinical planning module to enhance the AOSLO data acquisition efficiency. With the module, it is efficient to relate high-resolution but small field size images acquired with the AOSLO to clinical imaging. The improvement of the efficiency was demonstrated by imaging the retina in healthy and diseased eyes, especially the RNFL in a large region. The experiment and results have been published (Huang, Qi, Chui, Zhong, & Burns, 2012).

Approaches presented in Chapter 2 and 3 generally improve the quality and efficiency of AOSLO imaging. We used these approaches to image the temporal raphe as presented in Chapter 4 and 5. In the work presented in Chapter 4, the raphe was imaged from the fovea to at least 15-degree in temporal retina. The trajectories of the NFL bundles were found qualitatively consistent to the findings from *ex vivo* histology studies. In addition, we observed that the raphe was not always lined up with the centers of the fovea and optic disc, which could be attributed to the large variability of visual field testing results observed in population. The experiment and results have been published (Huang, Gast, & Burns, 2014).

Chapter 5 presents imaging and analyzing the difference of the temporal RNFL in normal and glaucomatous subjects. Detailed visualization of the RNFL and the impact of the mild local visual-field defects on the RNFL appearance were observed. The difference between the healthy and diseased RNFL was quantified, showing statistically

significant differences between the control and diseased groups. The experiment and results have been published (Huang, Luo, Gast, Burns, Malinovsky, & Swanson 2015).

1.7 References

Allingham, R. R., Damji Karim, Freedman Sharon, Moroi Satoko, Shafranov George. (2005). *Shields' textbook of Glaucoma*: Lippincott Williams & Wilkins.

Anderson, D. R., Kinghton, R.W. (1988). *perimetry and acuity perimetry*. Thorofare, NJ;: Slack,Inc.

Balazsi, A. G., Rootman, J., Drance, S. M., Schulzer, M., & Douglas, G. R. (1984). The effect of age on the nerve fiber population of the human optic nerve. *Am J Ophthalmol, 97*(6), 760-766.

Budenz, D. L., Anderson, D. R., Varma, R., Schuman, J., Cantor, L., Savell, J., . . . Tielsch, J. (2007). Determinants of normal retinal nerve fiber layer thickness measured by Stratus OCT. *Ophthalmology, 114*(6), 1046-1052. doi: 10.1016/j.ophtha.2006.08.046

Burns, S. A., Tumbar, R., Elsner, A. E., Ferguson, D., & Hammer, D. X. (2007). Large-field-of-view, modular, stabilized, adaptive-optics-based scanning laser ophthalmoscope. *J Opt Soc Am A Opt Image Sci Vis, 24*(5), 1313-1326.

Chan-Ling, T., & Stone, J. (1991). Factors determining the migration of astrocytes into the developing retina: migration does not depend on intact axons or patent vessels. *J Comp Neurol, 303*(3), 375-386. doi: 10.1002/cne.903030304

Chui, T. Y., Song, H., & Burns, S. A. (2008). Adaptive-optics imaging of human cone photoreceptor distribution. *J Opt Soc Am A Opt Image Sci Vis, 25*(12), 3021-3029. doi: 10.1364/josaa.25.003021

Cioffi, G. A., Robin, A. L., Eastman, R. D., Perell, H. F., Sarfarazi, F. A., & Kelman, S. E. (1993). Confocal laser scanning ophthalmoscope. Reproducibility of optic nerve head topographic measurements with the confocal laser scanning ophthalmoscope. *Ophthalmology, 100*(1), 57-62.

Curcio, C. A., & Allen, K. A. (1990). Topography of ganglion cells in human retina. *J Comp Neurol, 300*(1), 5-25. doi: 10.1002/cne.903000103

Drance, S. M., Berry, V., & Hughes, A. (1966). Studies in the reproducibility of visual field areas in normal and glaucomatous subjects. *Can J Ophthalmol, 1*(1), 14-23.

Drasdo, N., Millican, C. L., Katholi, C. R., & Curcio, C. A. (2007). The length of Henle fibers in the human retina and a model of ganglion receptive field density in the visual field. *Vision Res, 47*(22), 2901-2911. doi: 10.1016/j.visres.2007.01.007

Drasdo, N., Mortlock, K. E., & North, R. V. (2008). Ganglion cell loss and dysfunction: relationship to perimetric sensitivity. *Optom Vis Sci, 85*(11), 1036-1042. doi: 10.1097/OPX.0b013e31818b94af

Dubinin, A. V. B., Alexey I.; Cherezova, Tatyana Y.; Kudryashov, Alexis V. (2004). *Anisoplanatism in adaptive optics compensation of human eye aberrations.* Paper presented at the Proceedings of the SPIE.

Ferguson, R. D., Zhong, Z., Hammer, D. X., Mujat, M., Patel, A. H., Deng, C., Burns, S. A. (2010). Adaptive optics scanning laser ophthalmoscope with integrated wide-

field retinal imaging and tracking. *J Opt Soc Am A Opt Image Sci Vis, 27*(11), A265-277. doi: 10.1364/JOSAA.27.00A265
Garway-Heath, D. F., Poinoosawmy, D., Fitzke, F. W., & Hitchings, R. A. (2000). Mapping the visual field to the optic disc in normal tension glaucoma eyes. *Ophthalmology, 107*(10), 1809-1815.
Garway-Heath, D. F., Ruben, S. T., Viswanathan, A., & Hitchings, R. A. (1998). Vertical cup/disc ratio in relation to optic disc size: its value in the assessment of the glaucoma suspect. *Br J Ophthalmol, 82*(10), 1118-1124.
Harrington DO, D. M. (1990). *The Visual Fields: Textbook and Atlas of Clinical Perimetry*. St Louis: CV Mosby
Hart, W. M., Jr., & Becker, B. (1982). The onset and evolution of glaucomatous visual field defects. *Ophthalmology, 89*(3), 268-279.
Harwerth, R. S., Wheat, J. L., Fredette, M. J., & Anderson, D. R. (2010). Linking structure and function in glaucoma. *Prog Retin Eye Res, 29*(4), 249-271. doi: 10.1016/j.preteyeres.2010.02.001
Heijl, A., & Bengtsson, B. (1996). The effect of perimetric experience in patients with glaucoma. *Arch Ophthalmol, 114*(1), 19-22.
Heijl, A., Leske, M. C., Bengtsson, B., Hyman, L., Bengtsson, B., Hussein, M., & Early Manifest Glaucoma Trial, G. (2002). Reduction of intraocular pressure and glaucoma progression: results from the Early Manifest Glaucoma Trial. *Arch Ophthalmol, 120*(10), 1268-1279.
Heijl, A., Lindgren, G., & Olsson, J. (1989). The effect of perimetric experience in normal subjects. *Arch Ophthalmol, 107*(1), 81-86.
Heuer, D. K., Anderson, D. R., Feuer, W. J., & Gressel, M. G. (1989). The influence of decreased retinal illumination on automated perimetric threshold measurements. *Am J Ophthalmol, 108*(6), 643-650.
Hood, D. C., Anderson, S., Rouleau, J., Wenick, A. S., Grover, L. K., Behrens, M. M., . . . Kardon, R. H. (2008). Retinal nerve fiber structure versus visual field function in patients with ischemic optic neuropathy. A test of a linear model. *Ophthalmology, 115*(5), 904-910. doi: 10.1016/j.ophtha.2007.06.001
Hood, D. C., & Kardon, R. H. (2007). A framework for comparing structural and functional measures of glaucomatous damage. *Prog Retin Eye Res, 26*(6), 688-710. doi: 10.1016/j.preteyeres.2007.08.001
Hood, D. C., Raza, A. S., de Moraes, C. G., Johnson, C. A., Liebmann, J. M., & Ritch, R. (2012). The Nature of Macular Damage in Glaucoma as Revealed by Averaging Optical Coherence Tomography Data. *Transl Vis Sci Technol, 1*(1), 3. doi: 10.1167/tvst.1.1.3
Hood, D. C., Raza, A. S., de Moraes, C. G., Liebmann, J. M., & Ritch, R. (2013). Glaucomatous damage of the macula. *Prog Retin Eye Res, 32*, 1-21. doi: 10.1016/j.preteyeres.2012.08.003
Huang, D., Swanson, E. A., Lin, C. P., Schuman, J. S., Stinson, W. G., Chang, W., et al. (1991). Optical coherence tomography. *Science, 254*(5035), 1178-1181.
Huang, G., Gast, T. J., & Burns, S. A. (2014). In vivo adaptive optics imaging of the temporal raphe and its relationship to the optic disc and fovea in the human retina. *Invest Ophthalmol Vis Sci, 55*(9), 5952-5961. doi: 10.1167/iovs.14-14893

Huang, G., Qi, X., Chui, T. Y., Zhong, Z., & Burns, S. A. (2012). A clinical planning module for adaptive optics SLO imaging. *Optom Vis Sci, 89*(5), 593-601. doi: 10.1097/OPX.0b013e318253e081

Huang, G., Zhong, Z., Zou, W., & Burns, S. A. (2011). Lucky averaging: quality improvement of adaptive optics scanning laser ophthalmoscope images. *Opt Lett, 36*(19), 3786-3788. doi: 10.1364/OL.36.003786

Huang, G., Tuo, L., Gast, T.J., Burns, S.A., Malinovsky V.E., & Swanson W.H. (2015). Imaging Glaucomatous Damage Across the Temporal Raphe. *Invest Ophthalmol Vis Sci, 56*(15). doi: 10.1167

Hudson, C., Wild, J. M., & O'Neill, E. C. (1994). Fatigue effects during a single session of automated static threshold perimetry. *Invest Ophthalmol Vis Sci, 35*(1), 268-280.

Jaffe, G. J., & Caprioli, J. (2004). Optical coherence tomography to detect and manage retinal disease and glaucoma. *Am J Ophthalmol, 137*(1), 156-169.

Jansonius, N. M., Nevalainen, J., Selig, B., Zangwill, L. M., Sample, P. A., Budde, W. M., . . . Schiefer, U. (2009). A mathematical description of nerve fiber bundle trajectories and their variability in the human retina. *Vision Res, 49*(17), 2157-2163. doi: 10.1016/j.visres.2009.04.029

Johnson, C. A., Adams, A. J., & Lewis, R. A. (1989). Evidence for a neural basis of age-related visual field loss in normal observers. *Invest Ophthalmol Vis Sci, 30*(9), 2056-2064.

Johnson, C. A., Wall, M., & Thompson, H. S. (2011). A history of perimetry and visual field testing. *Optom Vis Sci, 88*(1), E8-15. doi: 10.1097/OPX.0b013e3182004c3b

Jonas, J. B., Gusek, G. C., Guggenmoos-Holzmann, I., & Naumann, G. O. (1988). Size of the optic nerve scleral canal and comparison with intravital determination of optic disc dimensions. *Graefes Arch Clin Exp Ophthalmol, 226*(3), 213-215.

Jonas, J. B., Mardin, C. Y., & Grundler, A. E. (1998). Comparison of measurements of neuroretinal rim area between confocal laser scanning tomography and planimetry of photographs. *Br J Ophthalmol, 82*(4), 362-366.

Kass, M. A., Heuer, D. K., Higginbotham, E. J., Johnson, C. A., Keltner, J. L., Miller, J. P., . . . Gordon, M. O. (2002). The Ocular Hypertension Treatment Study: a randomized trial determines that topical ocular hypotensive medication delays or prevents the onset of primary open-angle glaucoma. *Arch Ophthalmol, 120*(6), 701-713; discussion 829-730.

Keltner, J. L., Johnson, C. A., Anderson, D. R., Levine, R. A., Fan, J., Cello, K. E., . . . Ocular Hypertension Treatment Study, G. (2006). The association between glaucomatous visual fields and optic nerve head features in the Ocular Hypertension Treatment Study. *Ophthalmology, 113*(9), 1603-1612. doi: 10.1016/j.ophtha.2006.05.061

Leske, M. C., Heijl, A., Hussein, M., Bengtsson, B., Hyman, L., Komaroff, E., & Early Manifest Glaucoma Trial, G. (2003). Factors for glaucoma progression and the effect of treatment: the early manifest glaucoma trial. *Arch Ophthalmol, 121*(1), 48-56.

Liang, J., Williams, D. R., & Miller, D. T. (1997). Supernormal vision and high-resolution retinal imaging through adaptive optics. *J Opt Soc Am A Opt Image Sci Vis, 14*(11), 2884-2892.

Lindenmuth, K. A., Skuta, G. L., Rabbani, R., Musch, D. C., & Bergstrom, T. J. (1990). Effects of pupillary dilation on automated perimetry in normal patients. *Ophthalmology, 97*(3), 367-370.

Martinez-Conde, S., Macknik, S. L., & Hubel, D. H. (2004). The role of fixational eye movements in visual perception. *Nat Rev Neurosci, 5*(3), 229-240. doi: 10.1038/nrn1348

McLellan, J. S., Marcos, S., & Burns, S. A. (2001). Age-related changes in monochromatic wave aberrations of the human eye. *Invest Ophthalmol Vis Sci, 42*(6), 1390-1395.

Ogden, T. E. (1983). Nerve fiber layer of the primate retina: thickness and glial content. *Vision Res, 23*(6), 581-587.

Ogden, T. E. (1984). Nerve-Fiber Layer of the Primate Retina - Morphometric Analysis. *Invest Ophthalmol Vis Sci, 25*(1), 19-29.

Ooto, S., Hangai, M., Takayama, K., Arakawa, N., Tsujikawa, A., Koizumi, H., . . . Yoshimura, N. (2011). High-resolution photoreceptor imaging in idiopathic macular telangiectasia type 2 using adaptive optics scanning laser ophthalmoscopy. *Invest Ophthalmol Vis Sci, 52*(8), 5541-5550. doi: 10.1167/iovs.11-7251

Ooto, S., Hangai, M., Takayama, K., Sakamoto, A., Tsujikawa, A., Oshima, S., . . . Yoshimura, N. (2011). High-resolution imaging of the photoreceptor layer in epiretinal membrane using adaptive optics scanning laser ophthalmoscopy. *Ophthalmology, 118*(5), 873-881. doi: 10.1016/j.ophtha.2010.08.032

Ooto, S., Hangai, M., & Yoshimura, N. (2011). Photoreceptor restoration in unilateral acute idiopathic maculopathy on adaptive optics scanning laser ophthalmoscopy. *Arch Ophthalmol, 129*(12), 1633-1635. doi: 10.1001/archophthalmol.2011.345

Parikh, R. S., Parikh, S. R., Sekhar, G. C., Prabakaran, S., Babu, J. G., & Thomas, R. (2007). Normal age-related decay of retinal nerve fiber layer thickness. *Ophthalmology, 114*(5), 921-926. doi: 10.1016/j.ophtha.2007.01.023

Park, S. P., Chung, J. K., Greenstein, V., Tsang, S. H., & Chang, S. (2013). A study of factors affecting the human cone photoreceptor density measured by adaptive optics scanning laser ophthalmoscope. *Exp Eye Res, 108*, 1-9. doi: 10.1016/j.exer.2012.12.011

Quigley, H. A., & Broman, A. T. (2006). The number of people with glaucoma worldwide in 2010 and 2020. *Br J Ophthalmol, 90*(3), 262-267. doi: 10.1136/bjo.2005.081224

Quigley, H. A., Brown, A. E., Morrison, J. D., & Drance, S. M. (1990). The size and shape of the optic disc in normal human eyes. *Arch Ophthalmol, 108*(1), 51-57.

Radius, R. L., & Anderson, D. R. (1979). The histology of retinal nerve fiber layer bundles and bundle defects. *Arch Ophthalmol, 97*(5), 948-950.

Ramrattan, R. S., Wolfs, R. C., Jonas, J. B., Hofman, A., & de Jong, P. T. (1999). Determinants of optic disc characteristics in a general population: The Rotterdam Study. *Ophthalmology, 106*(8), 1588-1596. doi: 10.1016/S0161-6420(99)90457-8

Rha, J., Jonnal, R. S., Thorn, K. E., Qu, J., Zhang, Y., & Miller, D. T. (2006). Adaptive optics flood-illumination camera for high speed retinal imaging. *Opt Express, 14*(10), 4552-4569.

Roorda, A. (2011). Adaptive optics for studying visual function: a comprehensive review. *J Vis, 11*(7). doi: 10.1167/11.5.6

Roorda, A., Romero-Borja, F., Donnelly Iii, W., Queener, H., Hebert, T., & Campbell, M. (2002). Adaptive optics scanning laser ophthalmoscopy. *Opt Express, 10*(9), 405-412. doi: 68843 [pii]

Sahin, B., Lamory, B., Levecq, X., Harms, F., & Dainty, C. (2012). Adaptive optics with pupil tracking for high resolution retinal imaging. *Biomed Opt Express, 3*(2), 225-239. doi: 10.1364/BOE.3.000225

Sakata, L. M., Deleon-Ortega, J., Sakata, V., & Girkin, C. A. (2009). Optical coherence tomography of the retina and optic nerve - a review. *Clin Experiment Ophthalmol, 37*(1), 90-99. doi: 10.1111/j.1442-9071.2009.02015.x

Schuman, J. S., Hee, M. R., Puliafito, C. A., Wong, C., Pedut-Kloizman, T., Lin, C. P., . . . Fujimoto, J. G. (1995). Quantification of nerve fiber layer thickness in normal and glaucomatous eyes using optical coherence tomography. *Arch Ophthalmol, 113*(5), 586-596.

Spry, P. G., & Johnson, C. A. (2001). Senescent changes of the normal visual field: an age-old problem. *Optom Vis Sci, 78*(6), 436-441.

Stevenson SB, R. A. (2005a). *Correcting for miniature eye movements in high resolution scanning laser ophthalmoscopy.* Paper presented at the Ophthalmic Technologies XV, Proceedings of SPIE, Bellingham, WA.

Stevenson SB, R. A. (2005b). *Correcting for miniature eye movements in high resolution scanning laser ophthalmoscopy.* Paper presented at the Proc SPIE, Bellingham, WA.

Stone, J., & Dreher, Z. (1987). Relationship between astrocytes, ganglion cells and vasculature of the retina. *J Comp Neurol, 255*(1), 35-49. doi: 10.1002/cne.902550104

Takayama, K., Ooto, S., Hangai, M., Arakawa, N., Oshima, S., Shibata, N., . . . Yoshimura, N. (2012). High-Resolution Imaging of the Retinal Nerve Fiber Layer in Normal Eyes Using Adaptive Optics Scanning Laser Ophthalmoscopy. *PLoS One, 7*(3). doi: ARTN e33158

DOI 10.1371/journal.pone.0033158

Takayama, K., Ooto, S., Hangai, M., Ueda-Arakawa, N., Yoshida, S., Akagi, T., . . . Yoshimura, N. (2013). High-resolution imaging of retinal nerve fiber bundles in glaucoma using adaptive optics scanning laser ophthalmoscopy. *Am J Ophthalmol, 155*(5), 870-881. doi: 10.1016/j.ajo.2012.11.016

Trivino, A., Ramirez, J. M., Salazar, J. J., Ramirez, A. I., & Garcia-Sanchez, J. (1996). Immunohistochemical study of human optic nerve head astroglia. *Vision Res, 36*(14), 2015-2028.

Vienola, K. V., Braaf, B., Sheehy, C. K., Yang, Q., Tiruveedhula, P., Arathorn, D. W., . . . Roorda, A. (2012). Real-time eye motion compensation for OCT imaging with tracking SLO. *Biomed Opt Express, 3*(11), 2950-2963. doi: 10.1364/BOE.3.002950

Wang, Y., Bower, B. A., Izatt, J. A., Tan, O., & Huang, D. (2008). Retinal blood flow measurement by circumpapillary Fourier domain Doppler optical coherence tomography. *J Biomed Opt, 13*(6), 064003. doi: 10.1117/1.2998480

Webb, R. H., Hughes, G. W., & Delori, F. C. (1987). Confocal scanning laser ophthalmoscope. *Appl Opt, 26*(8), 1492-1499. doi: 10.1364/AO.26.001492

Weinreb, R. N., Shakiba, S., & Zangwill, L. (1995). Scanning laser polarimetry to measure the nerve fiber layer of normal and glaucomatous eyes. *Am J Ophthalmol, 119*(5), 627-636.

Werner, E. B., & Drance, S. M. (1977). Early visual field disturbances in glaucoma. *Arch Ophthalmol, 95*(7), 1173-1175.

Winn, B., Whitaker, D., Elliott, D. B., & Phillips, N. J. (1994). Factors affecting light-adapted pupil size in normal human subjects. *Invest Ophthalmol Vis Sci, 35*(3), 1132-1137.

Wolfs, R. C., Borger, P. H., Ramrattan, R. S., Klaver, C. C., Hulsman, C. A., Hofman, A., . . . de Jong, P. T. (2000). Changing views on open-angle glaucoma: definitions and prevalences--The Rotterdam Study. *Invest Ophthalmol Vis Sci, 41*(11), 3309-3321.

Yang, Q., Arathorn, D. W., Tiruveedhula, P., Vogel, C. R., & Roorda, A. (2010). Design of an integrated hardware interface for AOSLO image capture and cone-targeted stimulus delivery. *Opt Express, 18*(17), 17841-17858. doi: 10.1364/OE.18.017841

Zhang, Y., Rha, J., Jonnal, R., & Miller, D. (2005). Adaptive optics parallel spectral domain optical coherence tomography for imaging the living retina. *Opt Express, 13*(12), 4792-4811.

CHAPTER 2: "LUCKY AVERAGING": QUALITY IMPROVEMENT ON ADAPTIVE OPTICS SCANNING LASER OPHTHALMOSCOPE IMAGES

ABSTRACT

Adaptive optics (AO) has greatly improved retinal image resolution. However, even with AO, temporal and spatial variations in image quality still occur due to wavefront fluctuations, intra-frame focus shifts and other factors. As a result, aligning and averaging images can produce a mean image that has lower resolution or contrast than the best images within a sequence. To address this, we propose an image post-processing scheme called "lucky averaging", analogous to lucky imaging (Fried, 1978) based on computing the best local contrast over time. Results from eye data demonstrate improvements in image quality.

2.1 Introduction

Adaptive optics scanning laser ophthalmoscopy (AOSLO) provides high-resolution *in vivo* retinal images and has become a reliable tool for studying the structure and function of the retina (Roorda, 2010). AOSLO systems typically provide real-time imaging, and thus record images over time. However, in almost all real-time image sequences, image quality varies slightly over both space and time. That is, local regions have higher contrast in one frame than another. Based on the point-scanning mechanism of an AOSLO, the variance can be attributed to both time-related and space-related factors, most likely including: dynamic changes in human eye aberrations such as the tear film, local retinal shape changes due to ocular pulse, accommodative fluctuations, and variations in the retinal shape which can interact with the above factors. In addition, images from subjects who have retinal defects such as detachments, drusen and edema produce even more pronounced variations in the retinal shape, which interact to enhance these variations in image quality.

Conventionally, AOSLO raw images are post-processed to decrease the impact of noise. Typically this is achieved by either manually or automatically choosing acceptable frames, omitting those with very large eye movements or blinks, aligning them to minimize the effect of both intra- and inter-frame movements (Stevenson SB, 2005), or then averaging the aligned frames. The more frames used for the averaging, the greater the increase in signal to noise ratio. On the other hand, since the averaging is frame-based, the intra-frame contrast variance is not altered. Therefore the calculation of the

mean can degrade the optimal image quality achieved from the image sequence. That is, the frame averaging is not taking the best advantage of the sequential nature of AOSLO imaging.

This problem is also true if recording views of the sky from a ground based telescope. By choosing only the best frames, images are selected when the atmospheric turbulence along the line of sight is minimal. That is, the process takes advantage of lucky moments when turbulence has a minimal effect and has therefore been called "lucky imaging" (Fried, 1978). In analogy the AOSLO is measuring the retina point-by-point, and its high frequency pixel clock makes it well suited for this "lucky imaging" approach, but now within a frame as well as between frames.

2.2 Methods

We propose a region-based averaging scheme we call "lucky averaging". Image acquisition and alignment are performed in the normal manner described above. However, before averaging, the image sequence is analyzed region by region. Small areas in the image represent short-exposure times and small spatial scales, greatly eliminating the intra-region variance in optical quality and enabling the process to capture those "lucky moments" when small region's image quality is at its best**.** The region quality is evaluated using an appropriate objective image quality metric and assigned to the central pixel of the region. Each pixel becomes the center of a region, and consequently, pixel

quality maps are built up in sequence. The final image is remapped by only including the times when each pixel has the highest image quality as evaluated using the metric. The scheme is shown in Fig.1.

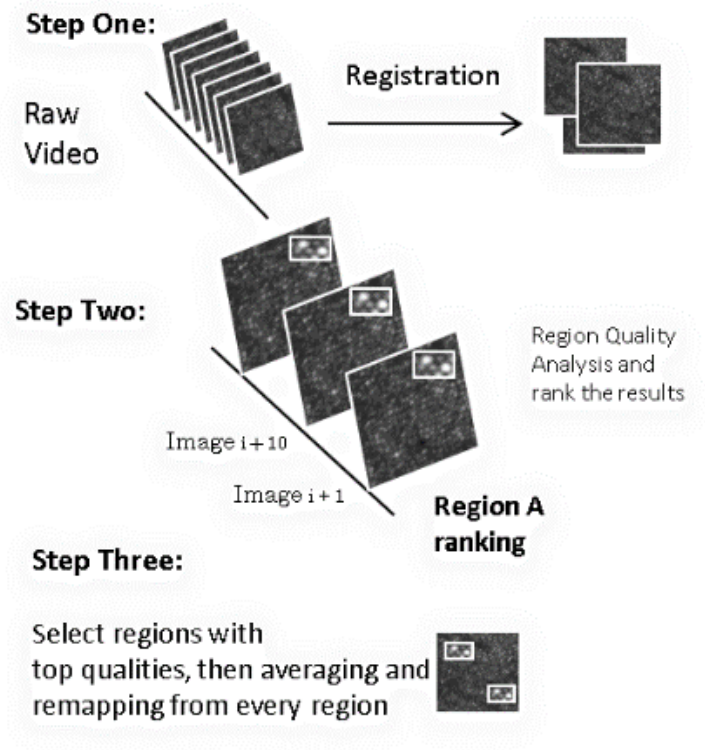

Figure 2. Schematic information flow for lucky averaging

To test this approach, cone photoreceptor images were acquired from different subjects and processed. The AOSLO system has been described previously (Ferguson et al., 2010). The pixel clock was 30MHz, and the frame rate was 30Hz. The AO control loop operated at 15Hz. Each image was 800 by 520 pixels, corresponding to 2.79°×1.78° imaging field in the retina. Each image series consisted of approximately 100 frames acquired sequentially in ~3 second. Once aligned, a window of 9 by 7 pixels was created and swept across the image, pixel-by-pixel to compute an image quality metric. A window of this size represented 450 μs in time and about 70 μm^2 in space.

While any appropriate image quality metric can be used, for this paper we implemented two examples - a sharpness metric and a gray level co-occurrence matrix (GLCM). The sharpness metric has been used for incoherent imaging in astronomy and synthetic radar image reconstructions (Muller R.A., 1974). It represents a sum of a nonlinear point transformation of the image and is generally defined as

$$s = \sum_{(x,y)} w(x,y) I(x,y)^{\beta} \qquad (1)$$

where *x,y* are pixel coordinates , and β is the power of the pixel intensity, *w(x,y)* is the weight for each pixel, and *I*(x,y) is the pixel intensity.

In practice, we set β as 2, and *w(x,y)* as 1. Normalization is also considered, as (Geng et al., 2011) indicates. The metric is finally defined as,

$$s_{(x_0,y_0,index)} = \frac{\sum_{(x_0-\Delta x \le x \le x_0+\Delta x, y_0-\Delta y \le y \le y_0+\Delta y)} I_{index}(x,y)^2}{(\sum_{(x_0-\Delta x \le x \le x_0+\Delta x, y_0-\Delta y \le y \le y_0+\Delta y)} I_{index}(x,y))^2} \qquad (2)$$

where *x, y* are pixel coordinates, x_0 and y_0 represent the coordinates of central pixels of the sampling window. Δx and Δy represent half the sampling window width and height respectively. The index represents the frame index number of the analyzed image within the sequence.

The second image metric is GLCM, measuring how often different combinations of gray levels co-occur in an image region (Haralick R.M., 1973), computed as in equation(3). For a given Δd which represents pixel separation between a pair of pixels, we compute $GLCM_{\Delta d}$ by examining pixel pair along 8 different directions from 0 degree to 315 degree with 45 degree increment, where the element $GLCM_{\Delta d}$ (i,j) represents the number of the pixel pair with gray level pair(i,j). The parameter *d* represents the two dimensional position vector of the pixel in the image. We typically normalize the GLCM by dividing the whole matrix with the sum of all elements in the matrix. Once a GLCM has been constructed, several types of statistical analysis can be performed. Local contrast is one of these measures, taking GLCM as contrast weights, computed as in equation(4), where α is the power of the gray level difference between a pixel pair , and β is the power of GLCM. In practice, for cone photoreceptor images, we calculated $GLCM_3$ or $GLCM_4$. α and β are set as 2 and 1 respectively.

$$GLCM_{(\Delta d)}(i,j) = \sum_{d \le AnalyzedRegion} \begin{cases} 1, if\ I(d) = i, I(d+\Delta d) = j \\ 0, \ otherwise; \end{cases} \quad (3)$$

$$Contrast(\alpha,\beta) = \sum_i \sum_j (i-j)^{\alpha} GLCM(i,j)^{\beta} \quad (4)$$

The calculation result $S(x_0, y_0,$ frame index) from equation (2) or equation (4) is then assigned to the central pixel (x_0,y_0). A quality metric S(x, y, frame index) is then generated for every pixel in the image sequence.

For either metric the final step is to set a threshold for including a pixel. That is, for a given pixel position(x,y), we can include (for instance) the 30%of the instances within the sequence when those pixel instances have the highest value of the image quality metric. The final image is then the average of those pixels. This is computationally fairly simple, taking about 3 minutes for 100 frames, using a 2.8 GHz PC with 8GB of memory and implemented in MATLAB.

2.3 Results and discussion

Figure 2 and 3 compare results from the different averaging methods. Similar results were obtained on two other subjects. In single frame images, we observe noise and contrast variance across the image (Fig.2a). The average image is less noisy(Fig.2b) and in an enlargement more details can be observed due to the decreased noise(Fig.3b). However, some cones are dim and some regions are still blurry. For the lucky averaging (Fig.2c, 2d and Fig.3c, 3d), the contrast reduction is decreased. Cones are somewhat brighter and more distinct, suggesting local contrast and resolution improvement. To quantify the difference between lucky-averaging and normal averaging, a power spectral analysis was performed. We calculated the power ratio, as a function of frequency

between lucky averaging and standard averaging (Fig.4). Thus, a ratio greater than one indicates a higher spectral power for lucky averaging at a given frequency. The average increase in powers between either lucky averaging imaging metric and standard averaging is 20% and the improvement extends all the way to the optical cut-off frequency which is about 0.4 cycles/pixels based on the system resolution 2.5μm (Zou, Qi, & Burns, 2011) for this subject's pupil size of 6 mm. Beyond the cut-off frequency, the ratio fluctuates around one, indicating that the noise level is close between the two schemes. The two metrics used for lucky averaging produced similar improvements for these images, but because the scheme can be used with most local quality evaluation metrics the approach is general and can be tuned to optimize extraction of the most appropriate information.

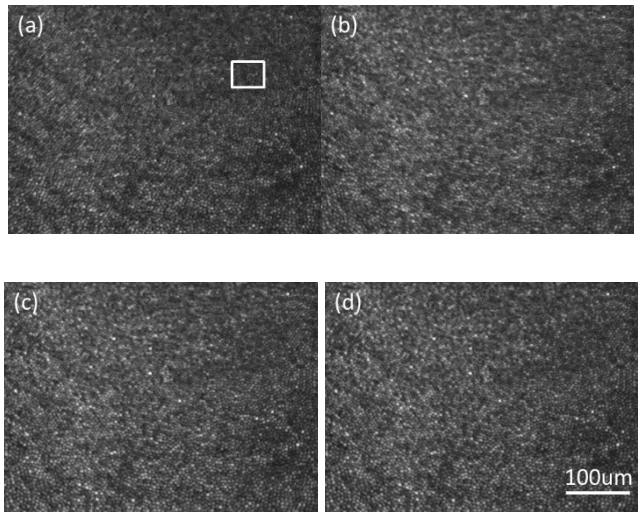

Figure 3. Image Comparison. Each image is 1.39° by 1.17° cropped from original frames. (a) a single-frame image (b) the image with normal averaging scheme, 20% frames are selected. (c) image after lucky averaging top 30% pixels from image sequence, with

GLCM contrast metric (d) image after lucky averaging top 30% pixels from image sequence, with sharpness metric

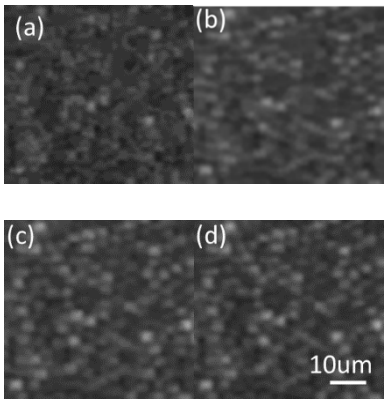

Figure 3. Enlarged regions location indicated in white in figure2. Fig 3(a-d) correspond to the same region in figure 2(a-d).

To investigate the role of the criterion for including pixels, we processed the same region in Fig.3 with varied criteria to include the best 20%, 30% and 40% of pixels using GLCM method (Fig.5). As expected, the improvement is largest with the lowest percentage criterion; however there is a limit, since as the criterion uses fewer samples, the impact of photon noise increases. Thus, the choice of criterion will be a balance between reducing random noise through averaging and improving contrast by picking the best "moments". One simple solution to this tradeoff is to collect more data for the same region of interest. It is also possible to base the criterion on the information itself, optimizing S/N ratio.

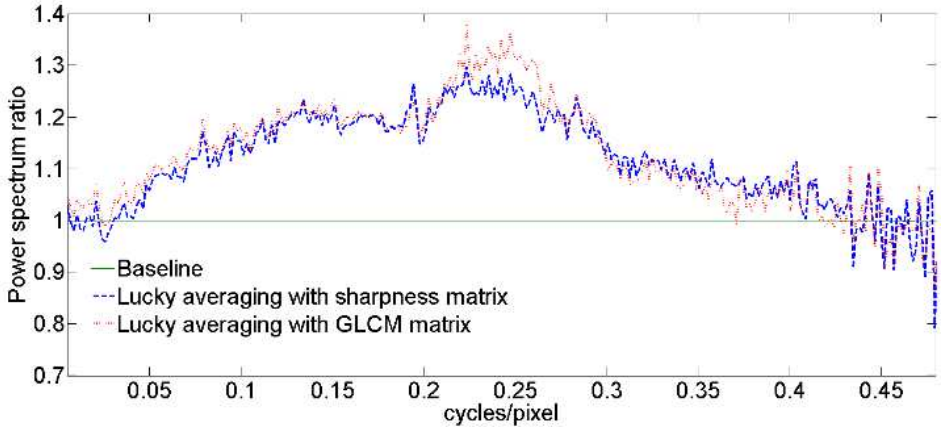

Figure 4. The spectral power ratio between lucky and conventional averaging. Dotted curve in red: ratio of Fig.3(c) to Fig.3(b) ; Dashed curve in blue: spectrum ratio of Fig.3(d) to Fig.3(b);

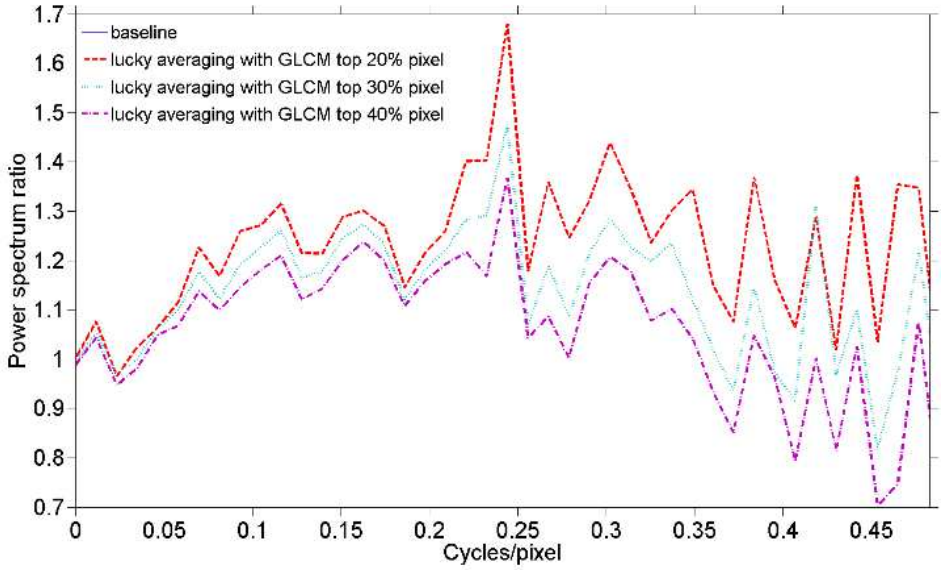

Figure 5. The spectral power ratios for different inclusion criteria; The baseline was based on conventional averaging. The dash-dot line in purple, the dotted line in light

blue and the dashed line in red represent inclusion criteria for the best 20%, 30% and 40% of pixels respectively

2.4 Conclusions

In summary, “lucky averaging”, analogous to “lucky imaging”, has been applied to AOSLO image post-processing. The image sequence is evaluated based on small regions instead of frames. The quality is enhanced by 20%, suggesting a better use of the data by this processing scheme. A larger dataset is necessary but collecting 3 or 4 seconds worth of data for each retinal region is realistic.

2.5 Acknowledgements

This work was supported by National Institutes of Health grants EY14375, EY04395 and P30EY019008.

2.6 References

Ferguson, R. D., Zhong, Z., Hammer, D. X., Mujat, M., Patel, A. H., Deng, C., . . . Burns, S. A. (2010). Adaptive optics scanning laser ophthalmoscope with integrated wide-field retinal imaging and tracking. *J Opt Soc Am A Opt Image Sci Vis, 27*(11), A265-277. doi: 10.1364/JOSAA.27.00A265

Fried, D. L. (1978). Probability of getting a lucky short-exposure image through turbulence. *Optical Society of America, Journal, 68*.

Geng, Y., Schery, L. A., Sharma, R., Dubra, A., Ahmad, K., Libby, R. T., & Williams, D. R. (2011). Optical properties of the mouse eye. *Biomed Opt Express, 2*(4), 717-738. doi: 10.1364/BOE.2.000717

Haralick R.M., S. K., Dinstein I. . (1973). Textural Features for Image Classification. *IEEE Trans. on Systems, Man, and Cybernetics, 3(6), pp. 610-621, 1973*.

Muller R.A., B. A. (1974). Real-time correction of atmospherically degraded telescope images through image sharpening. *J. Opt. Soc. Am. 64(9), 1200 -1210*.

Roorda, A. (2010). Applications of adaptive optics scanning laser ophthalmoscopy. *Optom Vis Sci, 87*(4), 260-268. doi: 10.1097/OPX.0b013e3181d39479

Stevenson SB, R. A. (2005). *Correcting for miniature eye movements in high resolution scanning laser ophthalmoscopy.* Paper presented at the Proc SPIE, Bellingham, WA.

Zou, W., Qi, X., & Burns, S. A. (2011). Woofer-tweeter adaptive optics scanning laser ophthalmoscopic imaging based on Lagrange-multiplier damped least-squares algorithm. *Biomed Opt Express, 2*(7), 1986-2004. doi: 10.1364/BOE.2.001986

CHAPTER 3: A CLINICAL PLANNING MODULE FOR AOSLO IMAGING

ABSTRACT

Purpose: To develop a clinical planning module (CPM) to improve the efficiency of imaging subjects with a steerable wide-field adaptive optics scanning laser ophthalmoscope (AOSLO) and to evaluate the performance of this module by imaging the retina in healthy and diseased eyes.

Methods: We developed a software-based CPM with two submodules: a navigation module and a montage acquisition module. The navigation module guides the AOSLO to image identified retinal regions from a clinical imaging platform using a matrix-based mapping between the two. The montage acquisition module systematically moves the AOSLO steering mirrors across the retina in predefined patterns. The CPM was calibrated using a model eye and tested on five normal subjects and one patient with a retinal nerve fiber layer defect.

Results: Within the central ±7° from the fixation target, the CPM can direct the AOSLO beam to the desired regions with localization errors of <0.3°. The navigation error increases with eccentricity, and larger errors (up to 0.8°) were evident for regions beyond 7°. The repeatability of CPM navigation was tested on the same locations from two subjects. The localization errors between trials on different days did not differ

significantly ($p > 0.05$). The region with a size of approximately 13° × 10° can be imaged in about 30 min. An approximately 12° × 4.5° montage of the diseased region from a patient was imaged in 18 min.

Conclusions: We have implemented a clinical planning module to accurately guide the AOSLO imaging beam to desired locations and to quickly acquire high-resolution AOSLO montages. The approach is not only friendly for patients and clinicians but also convenient to relate the imaging data between different imaging platforms.

3.1 Introduction

Adaptive optics scanning laser ophthalmoscopes (AOSLO) allow real-time imaging of cellular and sub-cellular structure in the living human eye. In recent years, AOSLO systems have been employed for a growing range of scientific and clinical applications, including detailed measurements of the photoreceptors (Chui, Song, & Burns, 2008; Dubra et al., 2011; Merino, Duncan, Tiruveedhula, & Roorda, 2011; Song, Chui, Zhong, Elsner, & Burns, 2011), vasculature (Chui, Zhong, Song, & Burns, 2012; Martin & Roorda, 2005; Tam et al., 2011; Zhong, Petrig, Qi, & Burns, 2008) and other retinal structures (Morgan, Dubra, Wolfe, Merigan, & Williams, 2009; Roorda, Zhang, & Duncan, 2007). However, adaptive optics (AO) imaging systems typically have a field of view (FOV) of only a few degrees due to optical limitations (Bedggood, Daaboul, Ashman, Smith, & Metha, 2008) and this can lead to problems of targeting the high resolution imaging to specified regions of interest on the retina. A typical approach is to image a recognizable landmark first and then move the imaging region towards the target region by asking the subject to fixate different targets in spatial sequence, often using a movable fixation spot or a fixation array. If a montage of the affected retinal region is required, the patient is asked to sequentially fixate a series of neighboring fixation targets or a movable target. Burns et.al (Burns, Tumbar, Elsner, Ferguson, & Hammer, 2007) introduced a different approach by designing a steerable AOSLO combined with a wide-field line scanning ophthalmoscope (LSO). The steering angle in the most recent version is extended to almost 30 degrees of the posterior pole without requiring re-fixation by the subject.13 The wide-field imaging video can guide the high resolution imaging session in

real-time. Both approaches are convenient for both the experimenter and the subject, but can be difficult to relate to other clinical imaging modalities. For Burns' approach (Burns et al., 2007; Ferguson et al., 2010), this arises because the wide field image quality was made subordinate to AOSLO image quality and thus identifying and navigating to specific clinical features can be difficult. Therefore, for both of these currently used approaches for AOSLO imaging, there can be difficulties in relating the very high resolution images to clinical images during the measurement session and thus be assured that the entire region of interest has been imaged.

For this reason we developed a clinical planning module intended to relate regions of interest from a common clinical imaging system directly to the AOSLO steering system. This module would allow the experimenter to guide the AOSLO directly to regions of interest using a fundus image available in clinics, and then to rapidly acquire a montage of the region around that location without requiring re-fixation by the subject. The overall goal of this development was to simplify the imaging session for the patient and also to improve the efficiency and throughput of an AOSLO imaging session without sacrificing the high quality of AOSLO imaging that has been widely demonstrated. In the current paper we present the techniques involved and provide initial data generated using this clinical planning module.

3.2 Methods

3.2.1 The Indiana adaptive optics scanning laser ophthalmoscope

The wide-field AOSLO has been described previously (Ferguson et al., 2010; Zou, Qi, & Burns, 2011). In brief, two deformable mirrors (DM) are employed to correct the ocular monochromatic aberrations in a closed-loop feedback system. Of these two DMs, one is a 52-actuator, 50um stroke DM (Imagine Eyes) for the correction of large-amplitude low-order aberrations and the other is a 140-actuator, 4um stroke DM (Boston Micromachines Corp) which is used for high-order aberration correction. The imaging wavelength is 840 nm and the size of each AO image is 2.00°×1.8°. The size of the confocal aperture in the system is approximately twice the size of the theoretical Airy disc. The optical resolution of the system is 2.4 microns for a 7mm pupil, although the system works with any size pupil from 3 to 8 mm and has been shown to produce images meeting the expectations of a confocal system operating near the diffraction limit (Zou et al., 2011). Videos are recorded at a frame rate of 30 Hz, using a maximum of 150 microwatts of 840 nm light (measured at the pupil plane). Light levels are safe according to the American National Standards Institute (ANSI) standards.

In order to achieve wide-field steering capability, the system incorporates a field mirror that subtends approximately 30 degrees at the retina. The AOSLO imaging beam can be moved to any location within this field by adding offset voltages to the horizontal and/or vertical steering mirror. A fixation target is provided by either a LED mounted

outside the 30 degree field of view, or by a programmable video fixation system that is mapped within the wide field of view of the system.

3.2.2 Clinical planning module

The clinical planning module consists of two sub-modules. The first sub-module is a navigation module which allows clinicians or operators to identify regions of interest on a clinical image by clicking on the central pixels of the clinical regions of interest. The field size of each clicked region is the same as the AOSLO's. Multiple regions (clicks) are typically necessary to cover both the normal and pathological regions. The location (s) of the region (s) as well as the clinical image are then used to control the AOSLO navigation module. This module guides the steerable AOSLO to the region of interest for high-resolution imaging by transforming the coordinates of those regions on the clinical image to the steering mirror's position. Because both the AOSLO and clinical fundus imaging platforms define the image pixel position as the visual angles subtended at the pupil plane of the eye (Rudnicka, Burk, Edgar, & Fitzke, 1998), the transformation is used to match the pixel angular position of one platform to the other. The actual spatial position of the pixel on the retina is not involved in the transformation. In addition to angular size or scale differences between systems, it is also necessary to correct translation and rotations of the pixel position between the two imaging platforms. Therefore, a 2 by 2 transformation matrix was used, where the four coefficients of the matrix can model any combination of scale, rotation and translation between the imaging coordinates of the AOSLO and the clinical fundus imaging platform.

In this study, a Spectralis OCT (Heidelberg Engineering, Heidelberg, Germany) was selected as the clinical fundus imaging platform and its confocal scanning laser ophthalmoscope (cSLO) Infra-Red (IR) image was used as the clinical image. The cSLO IR image from the Spectralis is referred as a cSLO image throughout the paper. The mapping between the steerable AOSLO and the Spectralis was measured in a series of steps. First, we created a "model eye" with a 30 degree field of view. The model eye consists of an achromatic lens of 100mm focus length in the pupil plane and a patterned paper target located 100mm from the lens. By imaging the model eye under identical conditions on both instruments we can be confident that a given location on the target of the model eye represented identical pixel angles for both systems. For the Spectralis the entire region was imaged in a single cSLO image. The corresponding coordinates of the AOSLO steering mirror were then determined by steering the AOSLO image field such that the same features of the target were located in the center of the AOSLO video frame and recording the steering mirror positions. For a given location, its pixel position in the cSLO image and the corresponding position of the AOSLO steering mirror were defined as a corresponding-point pair. The transformation matrix was then computed by least square fitting the coefficients of the matrix with five corresponding-point pairs. During the matrix computation, one of the pairs was defined as the fovea pair for the model eye. The relative distance of the other four pairs to the fovea pair was then calculated and used to compute the four coefficients of the matrix. Typically we select the center of the cSLO image and its corresponding AOSLO steering mirror position as the fovea-pair for the model eye. With this matrix and the fovea pair, pixel positions on the cSLO image can be transformed to steering mirror positions of the AOSLO.

With the same model eye three sets of transformation matrices were determined by different strategies for selecting corresponding-point pairs, and the performance of the strategies were evaluated. To perform this evaluation, one hundred features were identified within a circular region with a radius of 10 degrees centered on the "fovea" of the model eye's cSLO image such that there were 10 features within each 1 degree annular ring. Their positions in the two imaging platforms form 100 corresponding-point pairs. The first strategy selected five pairs of points within the central +/- 2 degree circular region of the cSLO image. It was expected that high mapping precision would be achieved in the central region using this strategy but the accuracy was expected to decrease with increased distance. The second strategy selected five uniformly distributed pairs within the central +/- 10 degree circular region to better model the global transformation as opposed to the foveal transformation. The third strategy divided the whole +/- 10 degree circular region of the cSLO image into five circular bands with a 2 degree separation, and then five features from each band were used to calculate the transformation matrix for that band, resulting in five transformation matrices. The aim of the third approach was to test if the global performance could be further optimized by adopting different matrices as opposed to the second strategy which only used a single matrix. Performance for each strategy was determined by first using the matrix to direct the AOSLO steering mirror to position the imaging field at the feature determined from the cSLO image and then computing the difference between a feature's actual location in the AOSLO frame and the center of the AOSLO frame in units of degrees. The difference was defined as the mapping error. For all three strategies, those corresponding-point pairs not used to determine the matrix were used to evaluate the

performance of the corresponding matrices. For the third strategy, the system would first determine which circular band the pair fell into, and then use the appropriate matrix. For an error-free case, the selected feature would fall onto the center of the AOSLO image frame and the mapping error would be zero.

When the navigation module was applied to a subject, the same matrix determined from the model eye was used while the fovea pair used in the model eye required updating. The fixation target position in the AOSLO and the fovea pixel position of the cSLO image form a new fovea-pair for the subject. An additional step of manual identification of the fovea was required before applying the navigation module to human subjects. This was required because the Spectralis cSLO did not have a sufficiently precise method for placing its fixation target and thus the fovea was not always located in the center of the cSLO field. We therefore first click on the approximate location of the fovea on the cSLO image, and then calculated a transform matrix for that approximate foveal point pair. There could still be an error however arising from inaccurate identification of the fovea position on the cSLO image. The error causes an extra translation of the fovea-pair and thus generates a new offset error. Therefore, after aligning the subject to the AOSLO, we identified a landmark near the fovea on the cSLO image such as a recognizable vessel crossing, and the AOSLO steering mirror moved the imaging field to the location calculated by the first estimate of the transform. The operator then made a fine adjustment of the AOSLO steering mirror to center the vessel crossing in the AOSLO image. The fovea pair was then updated automatically with this offset correction. If the experimenter intentionally moved the fixation target, for instance

to image peripheral retina, then the procedure was repeated.

The second sub-module is a montage acquisition module. This module allows the experimenter to predefine one or a series of montage sampling patterns for the AOSLO imaging and quickly sample the whole region. For a given imaging region, a montage pattern is defined by a series of locations in a text file. These locations represent the specified offset values relative to the starting location of the montage. To use the montage acquisition module the AOSLO imaging field is first navigated to a region of interest using a mouse click on the cSLO image displayed in the navigation module, and then the montage acquisition module automatically moves the imaging field to each relative location in sequence. The module requires the operator to decide to either accept the image sequence at a location or to repeat the imaging at that location. This allows the operator to give the subject an opportunity to blink or to retake the image of a region if image quality is not acceptable. The montage pattern and sizes are easily generated by the operator. For example, for a small defect less than 1 degree, a sampling pattern of 3 by 3 raster sampling grid with 1degree separation can be defined. For a large region of interest a larger set of offsets would be used.

3.2.3 Data acquisition

Six subjects participated in this study to evaluate the performance of the module. The right eyes of each subject were imaged. All subjects were dilated using 0.5% Tropicamide. No corrective lenses were worn during the study. Subject ages were

between 25 and 65 years. Subject 1-5 were healthy and had no ocular disease. Subject 6 was diagnosed with cotton wool spots and the retinal nerve fiber layer (RNFL) defects can be visualized on the subject's fundus image (Chui, Thibos, Bradley, & Burns, 2009). Research procedures were performed in accordance with the Declaration of Helsinki. The study protocol was approved by the institutional review boards of Indiana University and all subjects provided written informed consent after explanation of the risks and benefits of the study were explained and before participation in the studies.

For Subject 2 and Subject 3, the navigation module was evaluated by measuring the mapping errors of selected retinal features. At least twenty vasculature features on each subject's cSLO image were determined prior to the AOSLO imaging. Features were chosen within +/- 10 degree retinal eccentricity. During imaging, each feature was clicked and the AOSLO was guided by the navigation module to the calculated position. As soon as the subject's fixation stabilized, the video was acquired. Following the testing session, the first acceptable quality frame in the video was selected as the reference frame. The distance between the center of the target feature in the reference frame and the center of the frame was measured as the mapping error for that feature. To test the repeatability of the method, both subjects were imaged twice, selecting the same features on different days.

To test the montage acquisition module, the operator systematically imaged the RNFL using a predefined region of approximately 13 degrees by 10 degrees for all normal subjects. Two extra regions of RNFL were imaged from Subject 4 and Subject 5 to

assess the feasibility of acquiring larger montage data within a single session. For Subject 6 who has a RNFL defect, an approximately 12 degrees by 4.5 degrees region covering the affected region and nearby unaffected regions was imaged. To test if operators could satisfactorily operate the system without simultaneous wide-field imaging, the LSO13 in the AOSLO was turned off. All data acquisition was completed using only the steerable AOSLO and offline cSLO images.

Following the testing session, image frames were extracted from the video and processed offline to reduce the inter-frame and intra-frame eye movement (Stevenson SB, 2005). For each imaging location, multiple frames (typically 5 to 20 frames) were aligned and averaged to improve the signal to noise ratio. Multiple small field images were then stitched together to create a retinal montage using Adobe Photoshop CS4 (Adobe Systems Inc., San Jose, CA).

3.2.4 Statistical Analysis

For the results obtained on the model eye, the probability of differences in performance for the three strategies arising by chance was computed using the Student's t-test (2 tails, paired) in two approaches. In the first, the entire central +/- 10 degree circular region with 75 pairs of mapping errors was compared. In the second, individual t-tests were run for binning data in 2 degree annular bins. For the second test, 15 pairs of mapping error were used for each t-test. For human eyes, the repeatability of the navigation module between trials was examined using a t-test (2 tails, paired comparisons). Twenty features

in each trial were used for the comparison. Where multiple tests were performed, a Bonferroni correction was applied to the significance level such that we considered a result as significant if it had less than 5% probability of occurring by chance.

3.3 Results

The navigation module performed better at the center of the imaging systems than at higher eccentricities when the module was tested on the model eye with the transformation matrix computed by any of the three strategies (Fig. 1). The averaged errors were calculated by averaging the mapping error in one degree bins. The standard errors (SE) of each averaged error were also computed. No significant difference was found between three strategies ($p>0.05$). The averaged errors within the central +/- 2 degree circular region are less than 0.1 degrees, approximately 6% of the frame size of the AOSLO. When the imaging field of the AOSLO was moved further from the center, the error increased, suggesting that the mapping relation between the two instruments changed with distance from the center of the field. However, between the central 2-6 degree region, the averaged errors of strategy two (0.12 degrees; SE +/- 0.02 degrees) and strategy three (0.10 degrees; SE +/- 0.02 degrees) are smaller than that of strategy one (0.18 degrees; SE +/- 0.02 degrees). Strategy one differed from strategy two and strategy three ($p<0.05$) but the latter two strategies did not differ. This result suggests that strategy two and strategy three have better global mapping capabilities than strategy one, as we expected. We also looked at the maximum error of each strategy since the

maximum error can limit practical use, and here the maximum errors over the central +/- 10 degree circular region were between 0.7- 0.8 degrees, which means that the feature selected in the cSLO image would appear at the margin of the AOSLO frame. However for strategy two and strategy three these large errors occurred only when the eccentricities were larger than approximately 7 degrees and only for some locations within the field. To guarantee that selected features appear within the central region of the frame, the imaging region could be restricted to be within +/- 7 degree region where the maximum errors of both strategies were under 0.3 degrees, approximately 20% of the frame size. Since strategies two and three were not reliably different in their performance, and strategy two was simpler, the matrix computed with strategy two was used to test the human subjects.

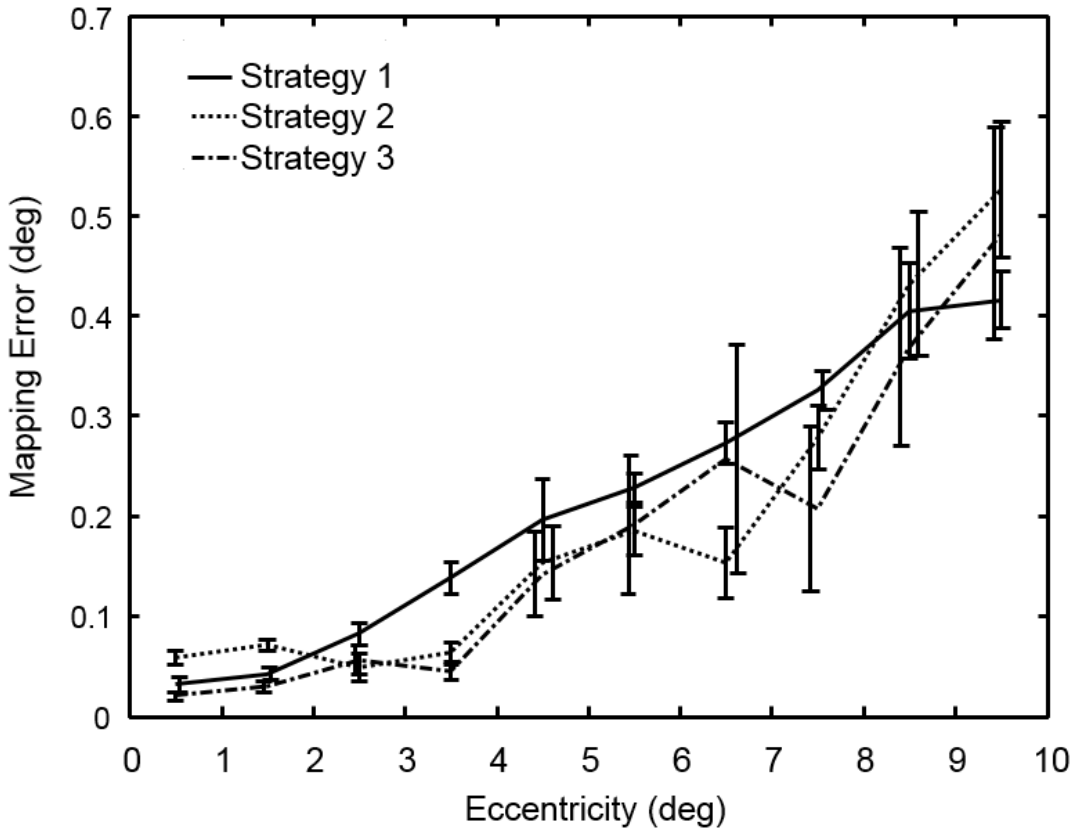

Figure 1. Mapping error as a function of eccentricity on the model eye. Data represents average errors within 1 degree intervals from the fovea (the center of the cSLO image). Strategy 1 involved fitting only points within the central region. Strategy 2 fit data points further from the center of the field. Strategy 3 fit the transform within annuli (see text). Error bars represent standard errors and show that not only does the average error increase but there is variability in the error depending upon the exact eccentricity.

The performance of the navigation module was similar when tested on human subjects to performance measured with the model eye. The displacement of features selected from the cSLO image from the center of the AOSLO image increased with increasing eccentricity. Within the central +/- 7 degree circular region, the feature selected by mouse-clicking on the cSLO image was always within the central region of the AOSLO imaging field. Example images are shown in Fig. 2. The averaged error was computed by averaging the mapping error per trial for each subject for the desired region. Within this central +/- 7 degree circular region the averaged error was less than approximately 0.3 degrees or 20% of the frame size (Fig. 3, left) and thus always appeared within the AOSLO image as a recognizable feature. The region outside the central +/- 7 degree circular region was also tested and the averaged mapping error for these more peripheral locations was more than twice as large as for the central region (Fig. 3, right). In the repeatability test, the average mapping error of the second trials on the same subjects were similar to the first trials, as shown in Fig. 3 and no significant difference in accuracy was found ($p>0.05$) between the two trials.

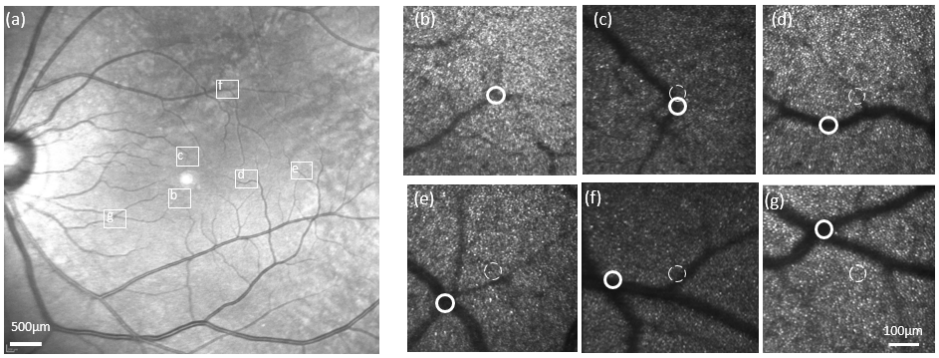

Figure 2. An example of the navigation module performance from Subject 3. (a) The cSLO mode image acquired from the Heidelberg Spectralis. The white squares in the image represent the locations where AOSLO images were requested via mouse click. Panels (b)-(f) The actual AOSLO images acquired by clicking at the locations indicated by the white squares in (a). Ideally the targeted feature from (a) would be at the center of the AOSLO frame. The solid circle in (b)-(f) show the feature and the dashed circles represent the frame centers. The error is the distance between these two locations and represents the combination of the algorithm error, and the error from head and eye movements by the subject.

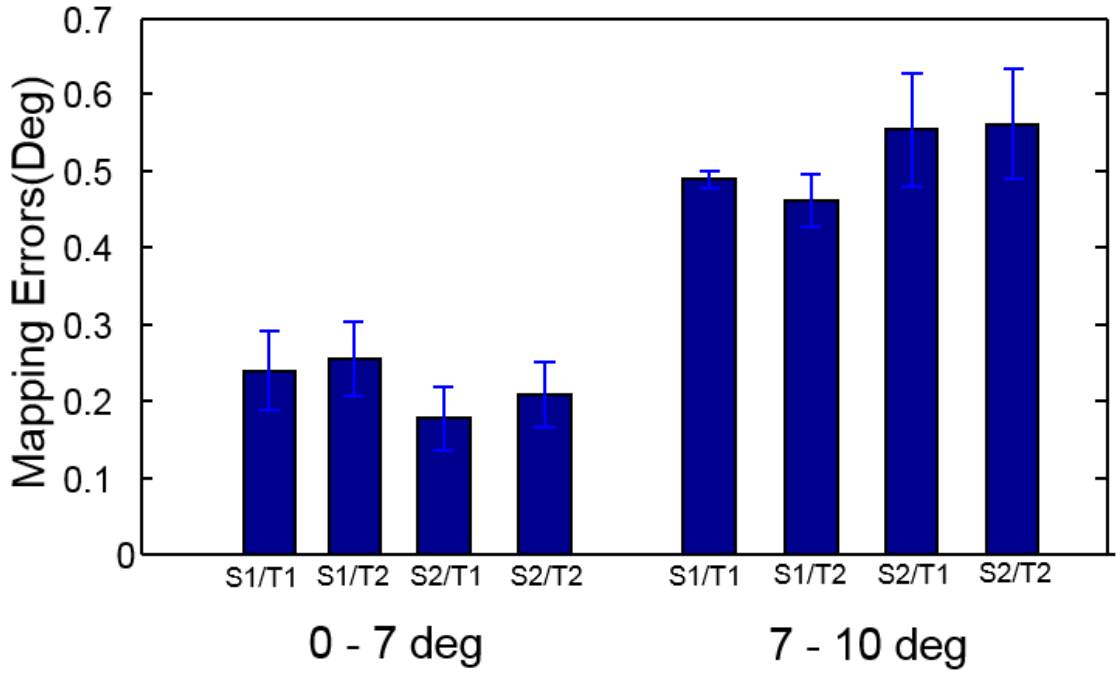

Figure 3. The averaged repeat mapping error measured by imaging multiple locations for Subject 2 and Subject 3 in two different imaging sessions on different days. The error bars represent the standard error for all location within the central +/-7 degrees retinal eccentricity (left) or for regions outside the central +/-7 degrees (right). S1 = Subject1, S2 = Subject2, T1 = Trial 1, T2 = Trial 2. For either subject, two trials were tested at each location on each of two days.

Imaging using the clinical planning module was efficient in terms of subject time, as shown in Table 1. This time does not include administering informed consent or aligning the subject to the system. The alignment of the subjects to the AOSLO took approximately two minutes for each subject although this was variable depending on the need to adjust the patient chair and headrest. The in-vivo foveal localization calibration required approximately one minute once the subject was aligned to the system. For healthy subjects, montages of approximately 13 degrees x 10 degrees required 30 minutes on average. For two experienced subjects, two extra montages were obtained and the total imaging lasted for about one hour and 15minutes. For Subject 6 who has the RNFL defect, an approximately 12 degrees x 4.5 degrees montage was acquired in approximately 18 minutes. We found that the major time-limiting factor was the time required to allow the subject to blink and for AO to stabilize on the selected retinal layer between locations in order to maximize image quality.

Subject List	Montage size(deg)	Imaging time(min)
Subject 1	13 degree × 8.5	27
Subject 2	13 degree × 9.4	35
Subject 3	12.8 degree × 7.4	20
Subject 4	Montage 1: 11.8 degree × 10 Montage 2: 13 degree × 10 Montage 3: 7 degree × 10.5	60
Subject 5	Montage 1: 12 degree × 11.6 Montage 2: 11 degree × 10.4 Montage 3: 6 degree × 16.7	63
Subject 6	12 degree ×4.5	18

Table 1. AOSLO imaging times for acquiring images from each subjects. Times only represent the imaging sessions and do not include administering informed consent and aligning the subject to the imaging system. Note, for subject 4 and subject 5, three montages were acquired from each subject thus the imaging time represents the total elapsed time for all three montages.

Montages were successfully built up from the images of all subjects. Fig. 4 shows montages of three large regions of RNFL from Subject 5, with the regions indicated by the white boxes on the SLO image from the Heidelberg Spectralis. Nerve fiber bundles can be seen proceeding across the retina from temporal and nasal regions, arcing above and below the fovea and finally approaching the optic disc. At the raphe isolated bundles, interdigitating from the upper and lower retina can also be seen (Fig. 4e). In the videos (not shown) the peripapillary vasculature can be identified due to moving cells within the capillaries. The montage of a region straddling a nerve fiber defect in Subject 6 is shown in Fig. 5. Note that the bundle defect appears as a lower contrast and darker region bounded by normal nerve fiber layer near the center of the montage.

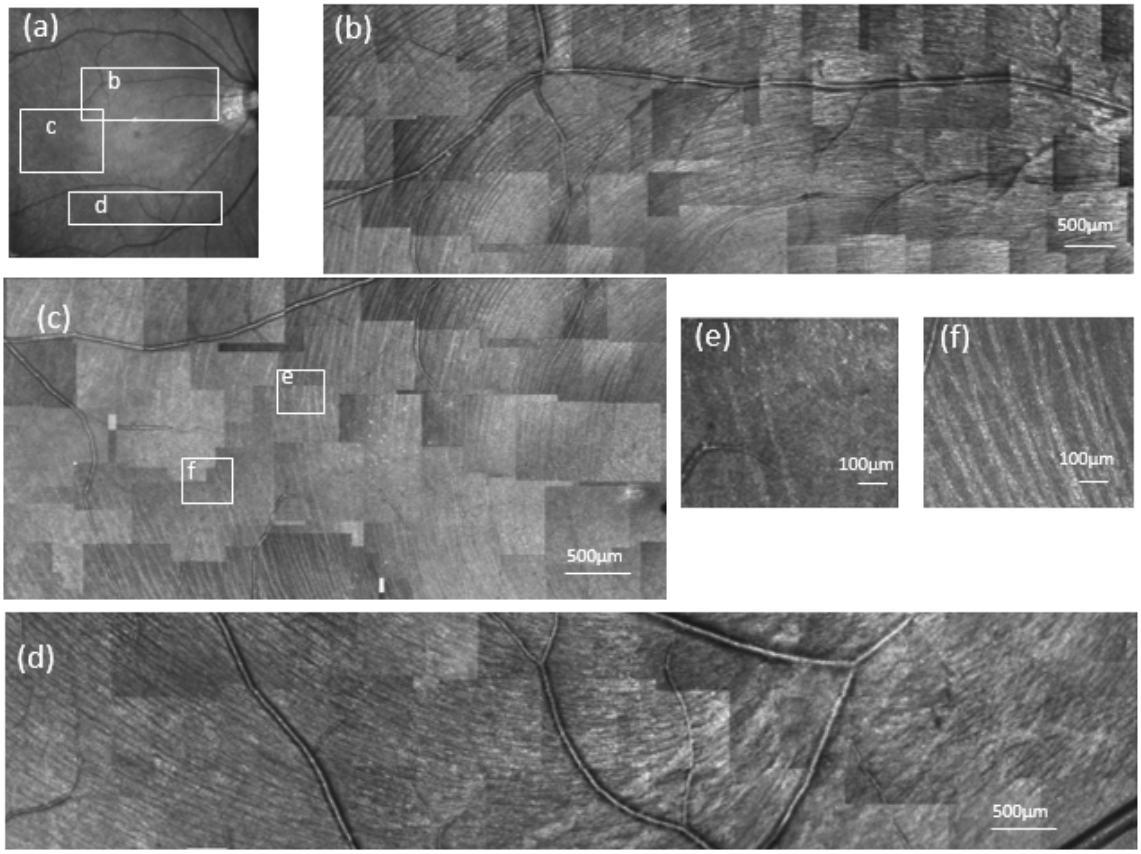

Figure 4. An example of the montage generated using the montage acquisition sub-module from Subject 5. (a) The SLO fundus image of Subject 5. (b)-(d) Montages constructed from three regions indicated by white squares in (a). Note that while montages b and c were collected separately with a rest between them, they actually overlap as shown schematically in (a). The white squares in (c) show regions that appear enlarged in (e) and (f).

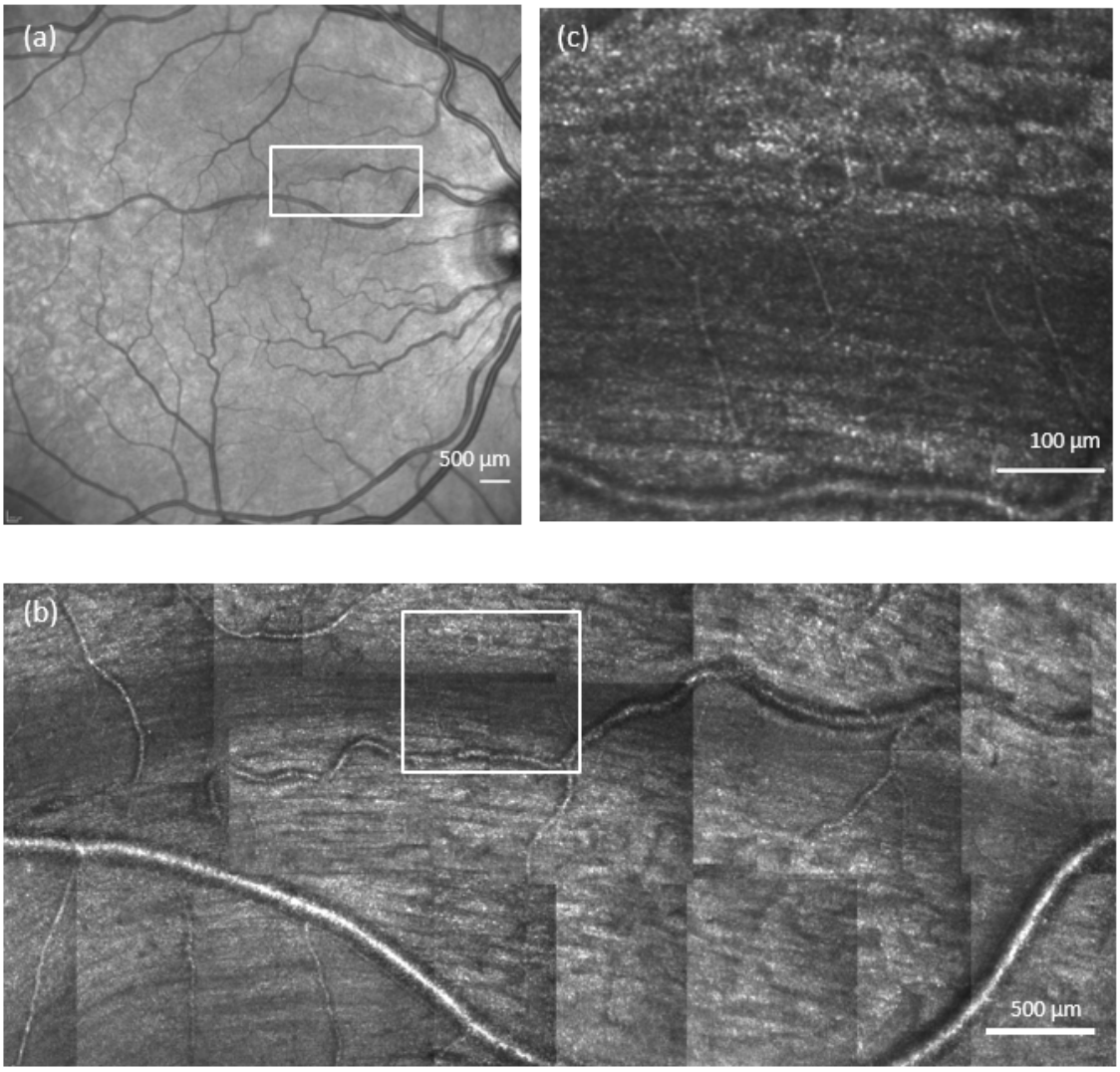

Figure 5. Example of AOSLO imaging of a nerve fiber defect from subject 6. (a) The cSLO image from the Heidelberg Spectralis. The white square in the image schematically indicates the AOSLO imaging region of the RNFL defect. The defect is due to a cotton wool spot and the resulting infarct caused the bundle in the superior nasal quadrant to be damaged. This damaged region can be seen in the SLO image as a dimming of the retinal reflection. (b) The AOSLO montage automatically acquired by

clicking within the defect and running a montage file for an approximately 12 degrees by 4.5 degrees region outlined by the white square region in (a). (c) An enlarged view of the section outlined by the white square in (b).

3.4 Discussion

The mapping approach we developed for the clinical planning module is a generic technique for mapping any standard fundus imaging platform to a steerable AOSLO system. The requirement is that the imaging system be constructed according to the telecentric principle. The systems used in this study meet this requirement, as do many other retinal imaging systems (Rudnicka et al., 1998). In a telecentric retinal imaging system the angular pixel position of the retinal images depends only on the visual angle at the pupil of the eye, and not on the focus of the system nor the axial length of the eye. This property simplifies the spatial relationship between two telecentric imaging systems allowing us to use a single transformation matrix. As long as the eye being imaged can be assumed not to change significantly between imaging sessions, then the mapping from external angles to internal retinal locations will be similar for a wide field imaging system and an AOSLO. The mapping itself is required because each imaging platform will have some field distortions and they will not be identical from system to system, rather they depend on the optical design of the particular system. Therefore, the procedures we describe for mapping between the AOSLO and the Spectralis system could be followed for many other fundus imaging systems. However, it is worth noting that there are

limitations to the mapping process. First, the mapping matrix itself is not generic for all the systems because each system will have different imaging coordinates, depending on the optical design of the particular system. Second, since the transformation matrix we implemented only incorporates translation, rotation and scaling, any distortion that changes with field angle, for example field distortion in the steerable AOSLO, cannot be well modeled by this particular transformation matrix. This is the most likely reason that the transformation matrix performed better towards the center of the field where the field distortion has less impact. Third, as mentioned, we assume that there are not major optical changes in the eye between measurements on the two systems. The most likely optical change that would occur is a change in the accommodative state of the subject. However, we regularly image individuals who are accommodating and we never see major shifts in retinal location with accommodation. The most important limitation is that fixational eye movements are unavoidable (Stevenson SB, 2005). While stabilization is possible, and we have used it,13 in general it is easier and faster to image a patient without using stabilization. During imaging a patient may exhibit horizontal, vertical and torsional eye movements which can occur even within the imaging time for a single frame and cause the images to distort and drift. This places a limit on mapping system accuracy and is the most likely cause for the increased errors we measured in real subjects as opposed to the model eye.

It is important to note that in principle, when mapping, it is possible to construct a more complex matrix where the coefficients of the transformation change with retinal field angle. We did not deem that the extra complexity was justified over the angles

subtended by our current systems, because, based on the testing result, the mapping error within the central ± 7 degree range is less than 20% of the frame size. In addition, for any intended location, we typically use the montage acquisition module to acquire images from more than a single frame location with the smallest likely target region being about 3x3 degrees. For regions outside of the central ± 7 degrees we simply move the fixation target to a predetermined eccentric location, placing the region of interest within the central field of the AOSLO and redo the in situ calibration.

The implementation of the clinical planning module also provides the possibility of spatially separating the choice of imaging locations, which could be done in the clinic by clicking on regions of clinical interest, and the high resolution imaging which is performed in the lab. The fundus image, together with a list of the coordinates of the regions of interest could then be transmitted electronically to the AOSLO site. The planning module then could quickly test the indicated locations by reading them in through the montage acquisition interface. Although we haven't implemented this remote capability, the process would be no different from the test we did in this study. Thus, the mapping process we have implemented between the two systems makes the remote communications between the two imaging sites more efficient and has the potential to make high resolution examinations more efficient in terms of both clinician and patient time.

Our approach can be used for imaging any retinal features. In this study we have demonstrated results for both photoreceptors and RNFL. We have used the RNFL data to

reveal a number of structural features of the RNFL. For instance, while anatomical studies (Henkind & Levitzky, 1969; Radius & Anderson, 1979) have shown that nerve fiber bundles combine and split apart, it has not often been possible to see this in vivo except for eyes with localized RNFL defects (Jeoung et al., 2008). However the AOSLO images show this quite clearly, especially near the raphe where the bundles are relatively sparse in normal eyes. One example is shown in Fig. 4 (f). Here the fiber bundles appear non-parallel to each other and even cross. We also saw that bundles separated and recombined as they crossed blood vessels (not shown) as documented by Zhang et al.(Zhang, Mitchell, Wen, & Laties, 2002). Finally, we saw that this indeterminacy of the location of the fiber bundles also occurred along the raphe. In this region, the reflectivity of the retina is relatively weak compared to regions where the RNFL is thicker. This darker appearance is expected based on the high reflectivity over an extended depth that can be seen on OCT imaging near the optic nerve (Guedes et al., 2003). However, near the raphe the darker background actually allows very high contrast for the sparse bundles that are present, as shown in Fig. 4(e). Because of this we were able to reliably image bundles down to approximately 4 microns in size. In 2 of those subjects (Subject 4 and Subject 5), it can be occasionally observed that, the bundles projecting across the superior and inferior retina were interdigitated, which indicates that the raphe may not represent a sharp horizontal boundary between the upper and lower visual fields on these two subjects (FitzGibbon, 1997). Ganglion cells in this region could be sending axons along either direction.

The montage acquired from the region of the bundle defect matches the expectation

from the arcuate scotoma, typically found to occur with glaucoma and cotton wool spots (Chui et al., 2009) and interestingly it is clear that despite the deep scotoma previously documented in this subject (Chui et al., 2009), there are some features still oriented within the bundle defect that appear similar to nerve fiber bundles, as shown in Fig. 5 (b) and (c). It is not clear if these are glial, or surviving bundles, but their presence is consistent with OCT images of this region where the RNFL layer is thinner, but some tissue remains (Chui et al., 2009; Kocaoglu et al., 2011). A similar result is also found in severe glaucoma where the RNFL thickness does not go to zero even when the eye is essentially blind (Sakamoto et al., 2010). In addition, although the density of fiber bundles is greatly reduced, it is still possible to see a capillary network crossing the defect and with a higher contrast due to the decreased scattered light from fiber bundles as shown in Fig. 5(c). The video recordings (not shown) reveal that the capillaries are functional with blood flow within them.

Overall, the high-resolution images and montages confirm the expected RNFL anatomy. While the larger maps, such as those presented in Fig. 4 still require imaging sessions of an hour or more, and therefore are not desirable for many clinic patients, they can provide insights into the basic properties of the retina and are realistic to perform in normal subjects or motivated research patients using the clinical planning module. For clinical patients, the clinical planning module allows the constructions of montages of about 15 degrees by 10 degrees. This size is realistic for research studies on patients, and may provide an alternative way of elucidating structural changes associated with eye diseases as well as monitoring of disease progression. While testing subjects with very

poor fixation stability will increase the time for testing, approaches to minimize the impact of eye movements are a topic of active research (Vogel, Arathorn, Roorda, & Parker, 2006; Yang et al., 2014).

3.5 Conclusions

We have implemented a clinical planning module to accurately guide the AOSLO imaging beam to desired locations, and to quickly acquire high resolution AOSLO montages of different sizes. The approach is not only friendly for patients and clinicians, but also convenient to relate imaging results across different imaging platforms.

3.6 Acknowledgements

This research was supported by NIH grants R01 EY07624, EY014375, NEI-P30EY019008.

3.7 References

Bedggood, P., Daaboul, M., Ashman, R., Smith, G., & Metha, A. (2008). Characteristics of the human isoplanatic patch and implications for adaptive optics retinal imaging. *J Biomed Opt, 13*(2), 024008. doi: 10.1117/1.2907211

Burns, S. A., Tumbar, R., Elsner, A. E., Ferguson, D., & Hammer, D. X. (2007). Large-field-of-view, modular, stabilized, adaptive-optics-based scanning laser ophthalmoscope. *J Opt Soc Am A Opt Image Sci Vis, 24*(5), 1313-1326.

Chui, T. Y., Song, H., & Burns, S. A. (2008). Individual variations in human cone photoreceptor packing density: variations with refractive error. *Invest Ophthalmol Vis Sci, 49*(10), 4679-4687. doi: 10.1167/iovs.08-2135

Chui, T. Y., Thibos, L. N., Bradley, A., & Burns, S. A. (2009). The mechanisms of vision loss associated with a cotton wool spot. *Vision Res, 49*(23), 2826-2834. doi: 10.1016/j.visres.2009.08.017

Chui, T. Y., Zhong, Z., Song, H., & Burns, S. A. (2012). Foveal avascular zone and its relationship to foveal pit shape. *Optom Vis Sci, 89*(5), 602-610. doi: 10.1097/OPX.0b013e3182504227

Dubra, A., Sulai, Y., Norris, J. L., Cooper, R. F., Dubis, A. M., Williams, D. R., & Carroll, J. (2011). Noninvasive imaging of the human rod photoreceptor mosaic using a confocal adaptive optics scanning ophthalmoscope. *Biomed Opt Express, 2*(7), 1864-1876. doi: 10.1364/BOE.2.001864

Ferguson, R. D., Zhong, Z., Hammer, D. X., Mujat, M., Patel, A. H., Deng, C., . . . Burns, S. A. (2010). Adaptive optics scanning laser ophthalmoscope with integrated wide-field retinal imaging and tracking. *J Opt Soc Am A Opt Image Sci Vis, 27*(11), A265-277. doi: 10.1364/JOSAA.27.00A265

FitzGibbon, T. (1997). The human fetal retinal nerve fiber layer and optic nerve head: a DiI and DiA tracing study. *Vis Neurosci, 14*(3), 433-447.

Guedes, V., Schuman, J. S., Hertzmark, E., Wollstein, G., Correnti, A., Mancini, R., . . . Mattox, C. (2003). Optical coherence tomography measurement of macular and nerve fiber layer thickness in normal and glaucomatous human eyes. *Ophthalmology, 110*(1), 177-189.

Henkind, P., & Levitzky, M. (1969). Angioarchitecture of the optic nerve. I. The papilla. *Am J Ophthalmol, 68*(6), 979-986.

Jeoung, J. W., Kim, T. W., Kang, K. B., Lee, J. J., Park, K. H., & Kim, D. M. (2008). Overlapping of retinal nerve fibers in the horizontal plane. *Invest Ophthalmol Vis Sci, 49*(5), 1753-1757. doi: 10.1167/iovs.07-1408

Kocaoglu, O. P., Cense, B., Jonnal, R. S., Wang, Q., Lee, S., Gao, W., & Miller, D. T. (2011). Imaging retinal nerve fiber bundles using optical coherence tomography with adaptive optics. *Vision Res, 51*(16), 1835-1844. doi: 10.1016/j.visres.2011.06.013

Martin, J. A., & Roorda, A. (2005). Direct and noninvasive assessment of parafoveal capillary leukocyte velocity. *Ophthalmology, 112*(12), 2219-2224. doi: 10.1016/j.ophtha.2005.06.033

Merino, D., Duncan, J. L., Tiruveedhula, P., & Roorda, A. (2011). Observation of cone and rod photoreceptors in normal subjects and patients using a new generation adaptive optics scanning laser ophthalmoscope. *Biomed Opt Express, 2*(8), 2189-2201. doi: 10.1364/BOE.2.002189

Morgan, J. I., Dubra, A., Wolfe, R., Merigan, W. H., & Williams, D. R. (2009). In vivo autofluorescence imaging of the human and macaque retinal pigment epithelial cell mosaic. *Invest Ophthalmol Vis Sci, 50*(3), 1350-1359. doi: 10.1167/iovs.08-2618

Radius, R. L., & Anderson, D. R. (1979). The histology of retinal nerve fiber layer bundles and bundle defects. *Arch Ophthalmol, 97*(5), 948-950.

Roorda, A., Zhang, Y., & Duncan, J. L. (2007). High-resolution in vivo imaging of the RPE mosaic in eyes with retinal disease. *Invest Ophthalmol Vis Sci, 48*(5), 2297-2303. doi: 10.1167/iovs.06-1450

Rudnicka, A. R., Burk, R. O., Edgar, D. F., & Fitzke, F. W. (1998). Magnification characteristics of fundus imaging systems. *Ophthalmology, 105*(12), 2186-2192. doi: 10.1016/S0161-6420(98)91214-3

Sakamoto, A., Hangai, M., Nukada, M., Nakanishi, H., Mori, S., Kotera, Y., . . . Yoshimura, N. (2010). Three-dimensional imaging of the macular retinal nerve fiber layer in glaucoma with spectral-domain optical coherence tomography. *Invest Ophthalmol Vis Sci, 51*(10), 5062-5070. doi: 10.1167/iovs.09-4954

Song, H., Chui, T. Y., Zhong, Z., Elsner, A. E., & Burns, S. A. (2011). Variation of cone photoreceptor packing density with retinal eccentricity and age. *Invest Ophthalmol Vis Sci, 52*(10), 7376-7384. doi: 10.1167/iovs.11-7199

Stevenson SB, R. A. (2005). *Correcting for miniature eye movements in high resolution scanning laser ophthalmoscopy.* Paper presented at the Ophthalmic Technologies XV, Proceedings of SPIE, Bellingham, WA.

Tam, J., Dhamdhere, K. P., Tiruveedhula, P., Manzanera, S., Barez, S., Bearse, M. A., Jr., . . . Roorda, A. (2011). Disruption of the retinal parafoveal capillary network in type 2 diabetes before the onset of diabetic retinopathy. *Invest Ophthalmol Vis Sci, 52*(12), 9257-9266. doi: 10.1167/iovs.11-8481

Vogel, C. R., Arathorn, D. W., Roorda, A., & Parker, A. (2006). Retinal motion estimation in adaptive optics scanning laser ophthalmoscopy. *Opt Express, 14*(2), 487-497.

Yang, Q., Zhang, J., Nozato, K., Saito, K., Williams, D. R., Roorda, A., & Rossi, E. A. (2014). Closed-loop optical stabilization and digital image registration in adaptive optics scanning light ophthalmoscopy. *Biomed Opt Express, 5*(9), 3174-3191. doi: 10.1364/BOE.5.003174

Zhang, X., Mitchell, C., Wen, R., & Laties, A. M. (2002). Nerve fiber layer splaying at vascular crossings. *Invest Ophthalmol Vis Sci, 43*(7), 2063-2066.

Zhong, Z., Petrig, B. L., Qi, X., & Burns, S. A. (2008). In vivo measurement of erythrocyte velocity and retinal blood flow using adaptive optics scanning laser ophthalmoscopy. *Opt Express, 16*(17), 12746-12756.

Zou, W., Qi, X., & Burns, S. A. (2011). Woofer-tweeter adaptive optics scanning laser ophthalmoscopic imaging based on Lagrange-multiplier damped least-squares algorithm. *Biomed Opt Express, 2*(7), 1986-2004. doi: 10.1364/BOE.2.001986

CHAPTER 4: *IN VIVO* ADAPTIVE OPTICS IMAGING OF THE TEMPORAL RAPHE AND ITS RELATIONSHIP TO THE OPTIC DISC AND FOVEA IN THE HUMAN RETINA

ABSTRACT

Purpose: To investigate the anatomy of the temporal raphe and its angular relationship to the optic disc and fovea in the human retina *in vivo*.

Methods: Adaptive optics scanning laser ophthalmoscope (AOSLO) was used to image the temporal raphe in 11 young subjects. The raphe's angle relative to a horizontal line and the raphe-fovea-disc angle (angle between the raphe and the line connecting the disc and fovea center) were determined. In addition, to investigate the impact of aging on the raphe, we imaged the raphe at 9-degrees eccentricity in 10 additional older healthy subjects, and compared the raphe's anatomy between the two age groups.

Results: The raphe's *in vivo* appearance was generally in agreement with major findings of *ex vivo* studies. The raphe angle was -1.67 ± 4.8 degrees, with the ranges from -9 degrees to 6 degrees. It was related to the angle of the foveal depression relative to the disc. The raphe-fovea-disc angle was 170.3 ± 3.6 degrees. The raphe gap, defined as the averaged distance between superior and inferior bundles, was significantly larger in the

older subjects than younger subjects (230.83 ± 113.22 μm versus 1.93 ± 68.73 μm, $p<0.0001$).

Conclusions: The angle of the raphe in the study was not consistent with classic raphe models. While the angle showed relatively large individual variability, there seems to be a systematic relation between the disc, fovea and raphe. It may be useful for individualizing retinal measurement strategies with regard to perimetry.

4.1 Introduction

The temporal raphe is generally described as a horizontal boundary separating the superior and inferior retinal nerve fiber bundles in the temporal retina. Detailed anatomy of the temporal raphe in the human retina is mainly based on observations of enucleated eyes (Ballantyne, 1947; Vrabec, 1966). However, these anatomical descriptions have never been validated by *in vivo* observations and these early anatomical studies did not address the angular relationship of the temporal raphe to the fovea and disc.

In vivo details of the spatial properties of the temporal raphe are fundamental in interpreting glaucomatous visual field defects and their relation to structural changes measured at the optic disc. For instance, the nerve fiber bundles in the area of the temporal raphe are frequently affected in early glaucoma. Studies have shown that a nasal step, which is characterized by a vertically asymmetric visual function loss across the temporal raphe, is a major visual field defect in early glaucoma (Armaly, 1971; Hart & Becker, 1982; Lee et al., 2003; Werner & Drance, 1977). In addition, a recent study showed that the geometric relation of the raphe to the optic disc and fovea is variable (Hood, Raza, de Moraes, Liebmann, & Ritch, 2013), and this variability can further complicate the work of modelling the trajectory of nerve fiber bundles and constructing structure-function maps for glaucoma diagnosis and management on an individual level (Garway-Heath, Poinoosawmy, Fitzke, & Hitchings, 2000; Jansonius et al., 2009; Jansonius, Schiefer, Nevalainen, Paetzold, & Schiefer, 2012; Lamparter et al., 2013; Schiefer et al., 2003; Weber & Ulrich, 1991).

Unfortunately, only a few *in vivo* imaging techniques will allow adequate visualization of the nerve fiber bundles defining the temporal raphe. Traditional optical imaging methods such as fundus photography cannot image the temporal raphe due to resolution and contrast limitations. Optical coherence tomography (OCT) can provide high axial resolution *in vivo*(D. Huang et al., 1991) and has been widely used to measure the thickness of retinal sub layers, especially the retinal nerve fiber layer (RNFL) thickness(Schuman et al., 1995). However, the thickness of the RNFL at the raphe has been shown to be less than 30 μm(Hood et al., 2012; Hood et al., 2013), which is equivalent to only a few pixels in OCT images acquired by commercial OCT imaging systems. Therefore, the accuracy of using an RNFL thickness map to determine *en face* morphology of the raphe is limited.

Adaptive optics scanning laser ophthalmoscopy (AOSLO) allows high resolution imaging of the *en face* plane by correcting ocular aberrations in real-time(Roorda et al., 2002). It has been widely used for retinal imaging, for instance, imaging of photoreceptors (Chui, Song, & Burns, 2008; Dubra & Sulai, 2011; Merino, Duncan, Tiruveedhula, & Roorda, 2011), blood flow(Chui, Gast, & Burns, 2013; Tam, Tiruveedhula, & Roorda, 2011; Zhong, Huang, Chui, Petrig, & Burns, 2012; Zhong, Song, Chui, Petrig, & Burns, 2011), and nerve fiber bundles(G. Huang, Qi, Chui, Zhong, & Burns, 2012; Kocaoglu et al., 2011; Takayama et al., 2012; Takayama et al., 2013). In one recent study, AOSLO imaging demonstrated the ability to image the RNFL near the raphe(G. Huang et al., 2012).

In the current study we used AOSLO imaging to image the RNFL at the temporal raphe in 11 healthy eyes of 11 young subjects. For each subject, the temporal raphe was imaged from the temporal parafovea to at least 15 degrees temporal to the fovea. The morphology of the raphe and its angular relationship to the optic disc and fovea were analyzed. In addition, to investigate the impact of aging on the RNFL in this region, we imaged the raphe at the 9-degree eccentricity in an additional set of 10 older subjects and compared the results between the two age groups.

4.2 Methods

4.2.1 Subjects

We tested 11 healthy young subjects (Group 1, mean age 25 years old, SD 6.7 years; 5 men and 6 women) and 10 healthy older subjects (Group 2, mean age 66.3 years old, SD 6.8 years; 5 men and 5 women). Each subject was examined by an ophthalmologist at least once in the past twelve months, and found to be free of ocular disease or diabetes. Only one eye of each subject was studied. All studied eyes were dilated using 0.5% Tropicamide. Each subject signed an approved consent form after the individual received a full explanation of the procedures and consequences of this study. The study protocol was approved by the Indiana University Institutional Review Board and the research is in compliance with the Declaration of Helsinki.

4.2.2 The Indiana Adaptive Optics Scanning Laser Ophthalmoscope

The wide-field AOSLO developed at the Indiana University Bloomington has been presented previously(Ferguson et al., 2010). In brief, the AOSLO uses wavelengths of 820-840 nm for retinal imaging. The system is capable of correcting ocular aberrations in real-time by employing a woofer-tweeter dual deformable-mirror closed-loop system. The imaging field size is programmable, ranging from approximately1 degree by 1 degree to 3 degrees by 3 degrees. Either field size is much smaller than imaging field sizes of regular fundus cameras. This is because the imaging field size for AO imaging is limited by the isoplanatic angle in human eyes(Bedggood, Daaboul, Ashman, Smith, & Metha, 2008; Nowakowski, Sheehan, Neal, & Goncharov, 2012). The fixation targets for subjects are optically projected to the retina by a custom digital projector incorporated within the AOSLO.

4.2.3 Procedures

Imaging for the young subjects (Group 1)

Each subject participated in three imaging stages sequentially during a single session lasting a total of approximately 80 minutes. In the first stage, we measured the axial length of each studied eye using a biometer (IOL Master; Carl Zeiss Meditec, Dublin, CA). In the second stage, we imaged each studied eye using an SLO/OCT system (Spectralis, Heidelberg Engineering, Heidelberg, Germany). For the SLO imaging, we

acquired three wide-field SLO images in sequence, with fixation targets presented at the fovea, at 15 degrees nasally from the fovea, and at 15 degrees temporally. The field size for each SLO image was set as 30 degrees by 30 degrees. After image acquisition, these three images were stitched into a mosaic using the Heidelberg's built-in software. We also performed two orthogonal OCT volume scans centered at the fovea. Each scan had a scanning size of 15 degrees by 5 degrees, with longer dimension placed along the OCT B-scans' direction. Adjacent OCT A-scans in each volume scan were 30 μm apart.

In the third stage, we imaged the temporal raphe of each studied eye using the AOSLO. The imaging field of the AOSLO was set as 3 degrees by 3 degrees which was adequate for detecting the details of the RNFL as was determined in pilot studies. We started the imaging just temporal to the fovea where nerve fiber bundles can be first detected by the AOSLO. After imaging bundles in this region, we repositioned the imaging field to the next location that was temporal to the current position with 0.5 degrees or more of overlap between imaging locations. Images were recorded in the new location. This process was repeated until we reached at least 15 degrees temporal to the fovea. In each step, we needed to adjust the imaging location slightly to ensure that the raphe appeared within the field of view of the images. For each location, the optical beam of the AOSLO was focused on the RNFL and 75 images (~2.3 seconds) were recorded. During the session, the subject's pupil was maintained in alignment with the AOSLO system by adjusting the position of a motorized chin rest. The subject was given breaks every 5 to 10 minutes. The whole AOSLO session for each subject took between 30 and 45 minutes.

Imaging for the older subjects (Group 2)

We simplified the imaging protocol for the older subjects to further shorten the testing time. For each studied eye, we measured the axial length using a biometer (IOL Master; Carl Zeiss Meditec, Dublin, CA). We performed AOSLO imaging of the raphe only between 8 to 10-degree eccentricities, with the same imaging field size and step size as for the young subjects.

4.2.4 Processing of AOSLO images and formation of montages

Following imaging, we processed raw AOSLO videos to align individual images and generate average images at each location(Song, Chui, Zhong, Elsner, & Burns, 2011). We then manually constructed a montage for each eye using image-analysis software (Photoshop CS6; Adobe Systems, San Jose, CA), as described below. First, AOSLO images from the same retina were aligned to each other based on overlapping portions of spatially-adjacent images. Second, the montage was aligned into the wide-field SLO mosaic. Figure 1a shows a wide-field SLO mosaic and Figure 1b shows an AOSLO montage. The red arrow in Figure 1a and 1b points to the same blood vessel to allow comparison of the relative positions.

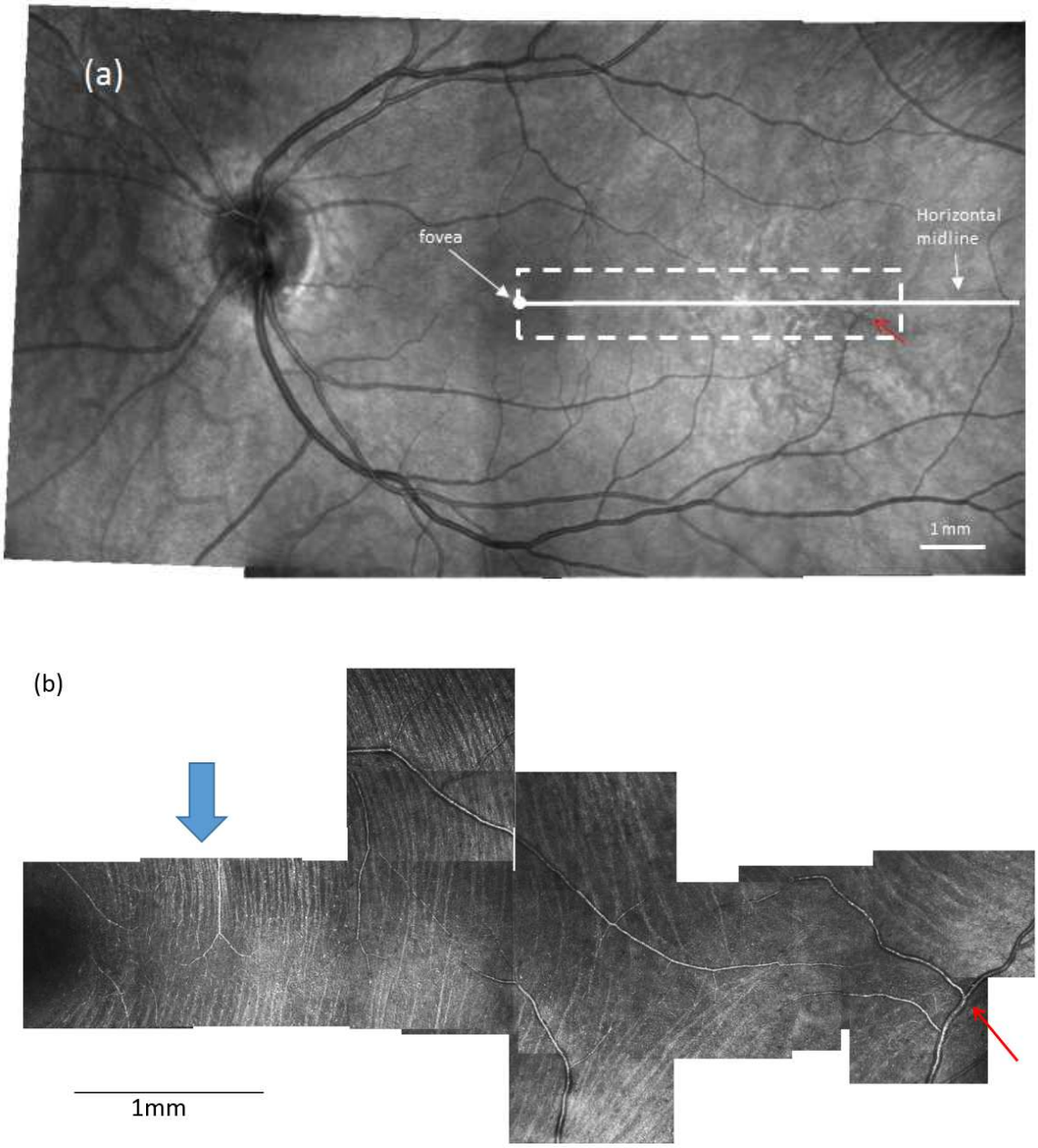

Figure 1. A wide-field fundus mosaic and an AOSLO raphe montage from the same subject in Group 1. **(a)** Fundus mosaic composed from three 30 degrees by 30 degrees Spectralis SLO images. The solid white circle represents the fovea as determined from OCT scans (see text). The white dashed box indicates the approximate region of AOSLO imaging. For all subjects, the AOSLO image was at least 15 degrees in horizontal extent.

The white solid line indicates the horizontal midline. **(b)** Raphe montage constructed from a series of AOSLO images. Contrast and brightness of each image has been adjusted to maximize the visibility of bundles and to approximately balance intensities. The blue arrows in Fig. 1(b) indicate the regions that are enlarged in Fig. 2. The red arrow in Fig. 1(a) and (b) point to the same blood vessel to allow comparison of the relative positions. Scale bars are 1 mm on both images.

4.2.5 Image analysis:

4.2.5.1 Analysis of images of the young subjects (Group 1)

Measurement of the raphe's gaps and locations in AOSLO montages

The nerve fiber bundles become thin and undetectable near the raphe. To quantify the size and location of this region without detectable nerve fiber bundles, we first manually marked the ends of the detectable nerve fiber bundles that were closest to the raphe for both the superior and inferior nerve fiber bundles. Next, for each side of the raphe, we used a linear model to interpolate positions of the bundle boundary between every two adjacent bundle tips that were marked in the first step, generating a continuous boundary for the bundles on the superior and inferior side of the raphe. Figure 2 shows examples of these measurements.

The superior and inferior boundaries were used to compute the raphe's gaps and locations. The gap was measured as the vertical distance between the two boundaries as a

function of retinal eccentricity. Note that, if the superior and inferior bundles interleave, the raphe gap becomes negative. The raphe position was computed as the average of the positions of the superior and inferior bundle boundaries for every retinal eccentricity. These raphe positions were further used to define a straight raphe line, using a least squares fit, for the computation of the raphe's angle in the next step.

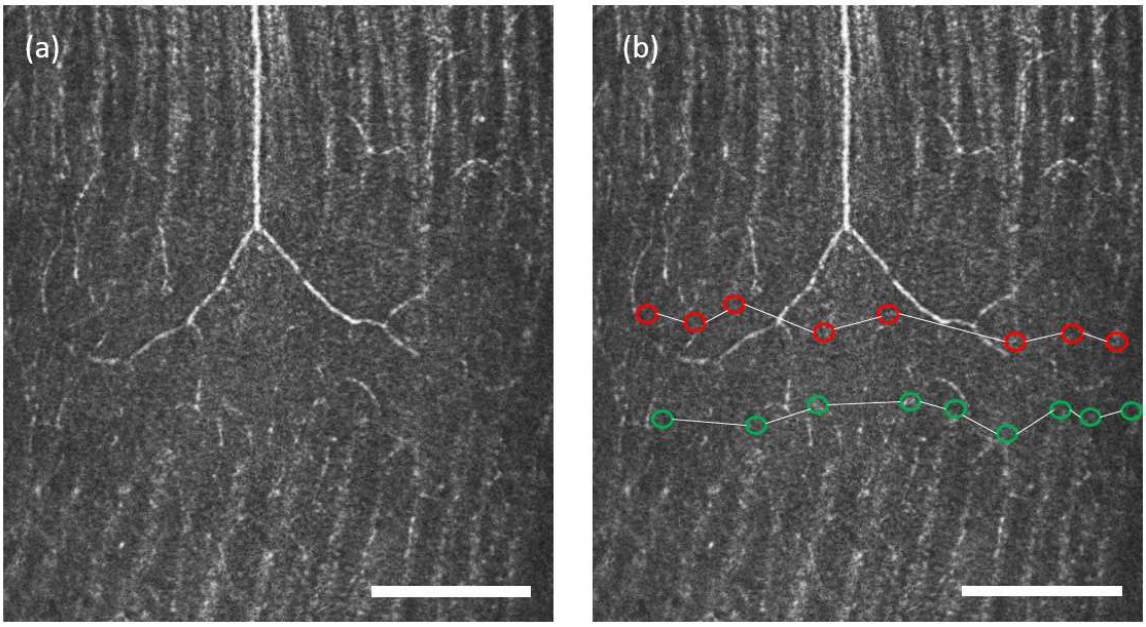

Figure 2. Enlargement of an AOSLO image from Figure 1b demonstrating the method for raphe location determination. This region is approximately 1mm from the fovea. (a) An image cropped from the montage in Figure 1b. (b) The figure shows boundaries for inferior bundles (green circles) and superior bundles (red circles). The raphe location is computed as the mean position between the two boundaries. This subject has a positive raphe gap at this eccentricity. Scale bar: 200 μm.

Measurement of raphe's position relative to the optic disc

1) Determination of fovea center

The fovea location was identified on each SLO montage using data from the OCT volume scans. The fovea region of each studied eye had been scanned with two OCT volume scans that were orthogonal to each other. In each pair of volume scans, we picked out that OCT B-scan image that was across or closest to the foveal pit. Its corresponding location on the SLO image was automatically identified as a line by the Heidelberg's built-in software. Thus, the crossing point of the two orthogonal lines was selected as the foveal center on the wide-field SLO mosaic, as shown in Figure 3a.

2) Determination of the optic disc center and its angle

The center of the optic disc was marked on each SLO montage by the following steps. First, we manually marked the four disc margins on the nasal, temporal, superior, and inferior sides. Second, we averaged the vertical positions of the inferior and superior margins, and the horizontal positions of the temporal and nasal margins. The averaged results were used as the position of the optic disc center, as shown in Figure 3a. The angle of foveal depression was then computed using the positions of the fovea and optic disc center, as shown in Figure 3b.

3) Determination of the raphe's angle and its angular relation to the optic disc

We used the fitted raphe line described in Section 1.1 to compute the raphe's angle relative to the horizontal midline of the retina. Sample results are presented in Figure 3b. We then computed the angle between the raphe and the line that connects the disc center and fovea, and defined this angle as the raphe-fovea-disc angle.

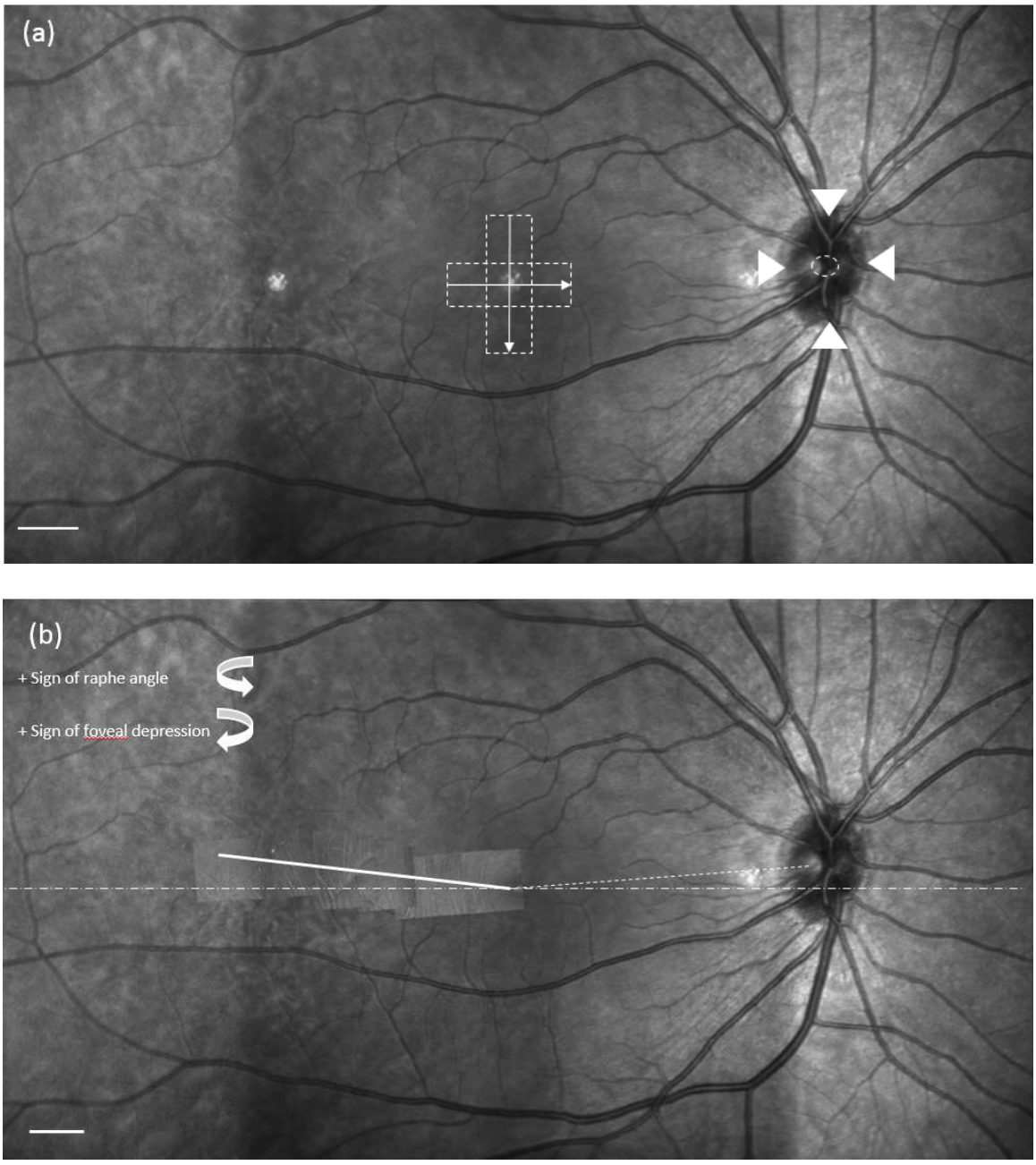

Figure 3. Example of the angular relation between the raphe, fovea, and optic disc. (a) Determination of the fovea and optic disc center. Dashed boxes in the center represent locations of OCT volume scans used to locate the center of the foveal pit. The arrows represent the orientations of B-scans. The arrowheads around the optic disc identify the upper, lower, left and right boundaries of the optic disc. The dashed circle is taken as the

center (see text). Scale Bar: 1 mm. (b) The dotted line connects the center of the optic disc and fovea. The dashed line represents the horizontal midline across the fovea. The solid line is the raphe determined from the AO montage and represents the least square linear fit to the measurements. Details of identifying the raphe and its angle are described in the text. Scale Bar: 1 mm.

4.2.5.2 Analysis of the effect of aging

For the older subjects (Group2), only the raphe gap was measured. The raphe's positions and angle were not measured for this group to avoid measurement errors due to the smaller imaging extent (between 8 and 10-degree eccentricities).

To analyze the aging effect, the raphe gaps between 8 and 10-degree eccentricity for each subject of the study were averaged and compared between the two groups. An unpaired t-test was used to test for statistical differences between the averaged gaps of the younger and older subjects.

4.3 Results

Appearance of the raphe and nerve fiber bundles in eyes of the young subjects (Group1)

Nerve fiber bundles were observed on both the superior and inferior temporal retina for all subjects tested. The bundles appeared as reflective strips with intervening dark strips (Figure 1b). As the bundles from the superior and inferior retina approach each other in the temporal retina, they become thinner and the raphe is formed.

The appearance of the raphe changed with eccentricity. For all subjects' locations that were within approximately 3 to 5 degrees temporal to the fovea, the bundles from the superior and inferior sides were narrow and ceased to be visible before they met; therefore the raphe appeared as a relatively dark band. The directions of bundles were approximately perpendicular to the raphe in this area, as shown in Figure 2a. In locations that were slightly further from the fovea, we observed that bundles' directions gradually became somewhat oblique relative to the vertical orientation seen closer to the fovea. In 3 young subjects, we observed that bundles in this region extended to the opposite side such that the inferior and superior bundles were interleaved, as shown in Figure 4. For the other 8 young subjects interleaving was not observed. In all cases the approach defined in 1.1 determined the raphe location. At large eccentricities the bundles formed a quasi-triangular pattern, as shown in Figures 1 and 5. In the region temporal to the triangular zone, the superior and inferior bundles gradually became more horizontal and parallel to each other. Here the raphe can be described as a narrow zone between relatively horizontal bundles which travel to the superior and inferior portions of the disk. In older subjects the raphe was wider and bundle interleaving was not detectable in any of the subjects. The other features observed in young subjects cannot be commented on as they were not included in the imaged area.

In addition to nerve fiber bundles, we also observed non-RNFL elements. Blood vessels were seen throughout the temporal retina as expected. Some crossed the raphe, even in locations that are close to the fovea. We measured the crossing location of the vessel closest to the fovea for each subject. The locations ranged from 2.6 degrees to

14.3 degrees, with an average at 6.4 degrees. In addition, we often observed patches of highly reflective structures in this part of the retina. They often appeared in peripheral retina beyond about 10 degrees, located near vessels and did not show any evidence of distorting the surrounding retina. One example of these structures can be seen in Figure 4b, however many were detected.

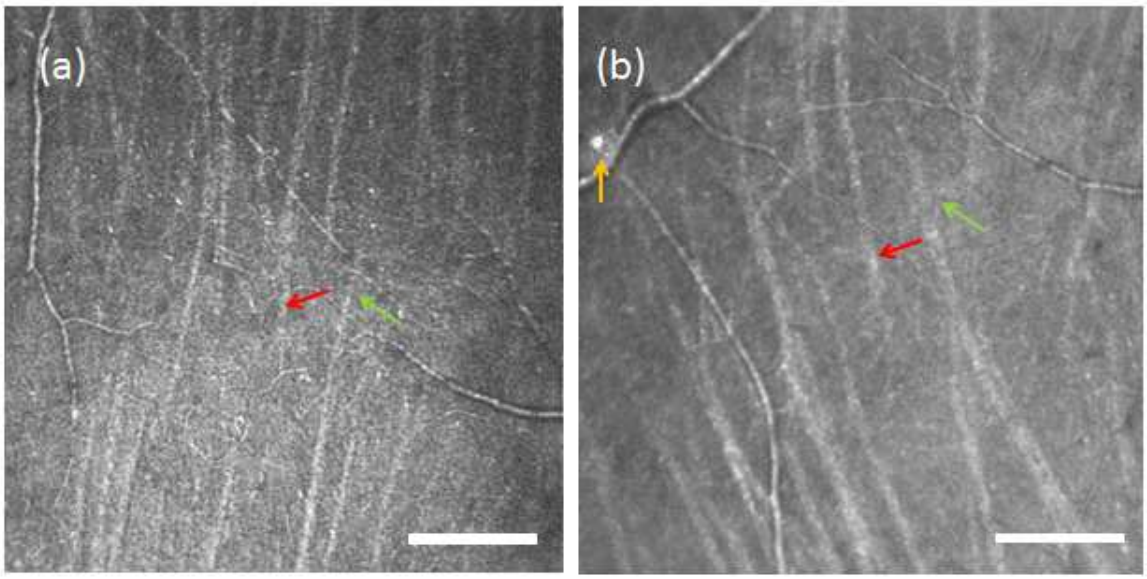

Figure 4. An example of a raphe with intermingling bundles from two Group 1 subjects. (a) The location is approximately 2 mm relative to the fovea. (b) The location is approximately 2.8 mm temporal to the fovea. Scale Bar: 200 μm. The red and green

arrows point to examples of bundles that interdigitate. Occasional reflective cells along vessels can be observed, as shown by the yellow arrow in (b).

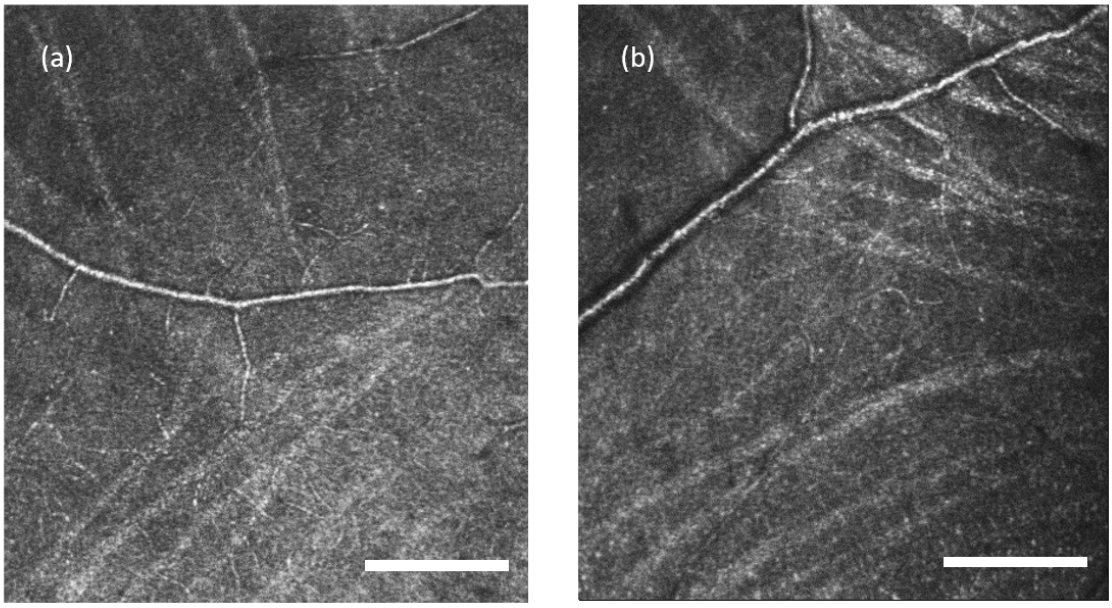

Figure 5. Raphe with oblique bundles forming a triangle bundle pattern. Images are from two subjects in Group 1. (a) A region approximately 3.7 mm from the fovea in a 26 year

old female. (b) A region approximately 3.8mm from the fovea in a 26 year old female. Scale Bar: 200 μm.

The raphe angle and its relation to the optic disc

On average, the raphe angle was -1.67 ±4.8 degrees relative to a horizontal line, with a range of angles from -9 to +6 degrees, as shown in Figure 6. The raphe-fovea-optic angle was 170.3 ± 3.6 degrees, as shown in Figure 7. The angle of the raphe was related to the angle of the foveal depression. A linear regression shows the slope was- 0.766 ± 0.604 ($p = 0.0185$), as shown in Figure 8. As the angle of the foveal depression increased, such that fovea was lower relative to the disc, the raphe was also rotated downward so the two rotate together.

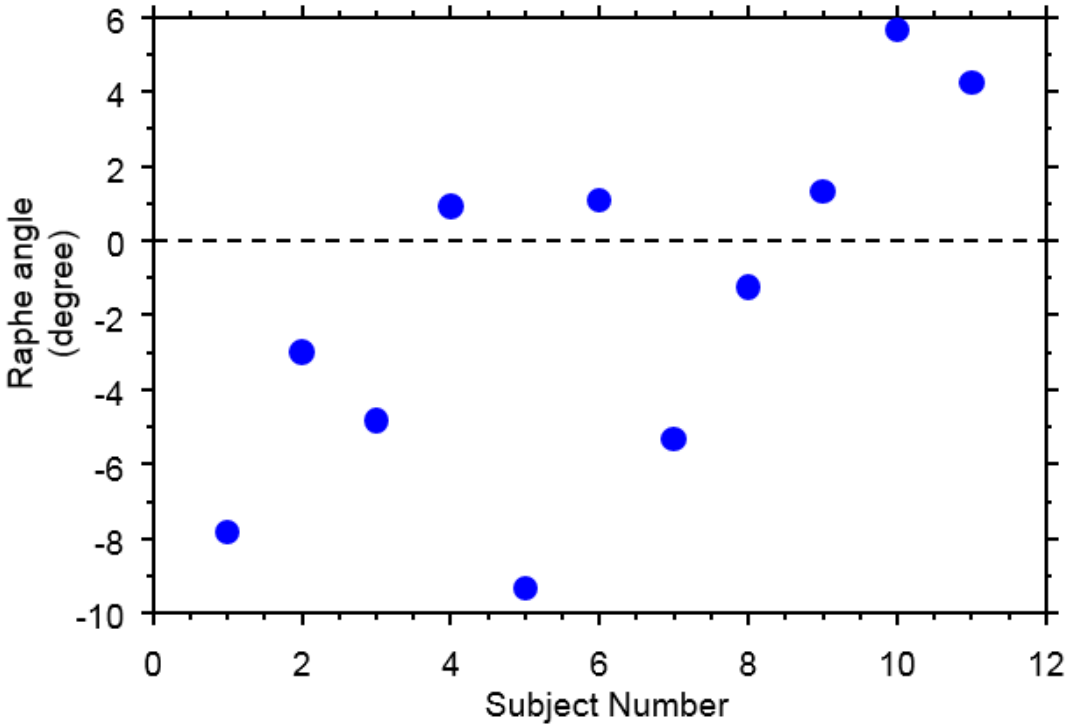

Figure 6. Raphe angles across subjects in the younger subjects (Group 1).

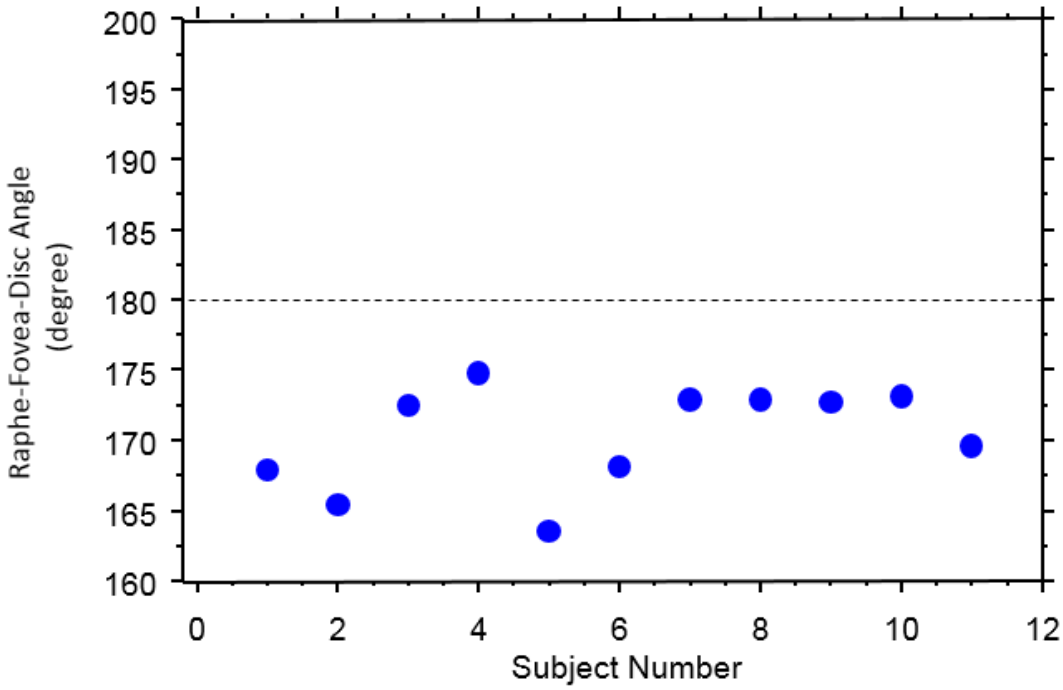

Figure 7. The raphe-fovea-disc angle of the subjects in the younger subjects (Group 1).

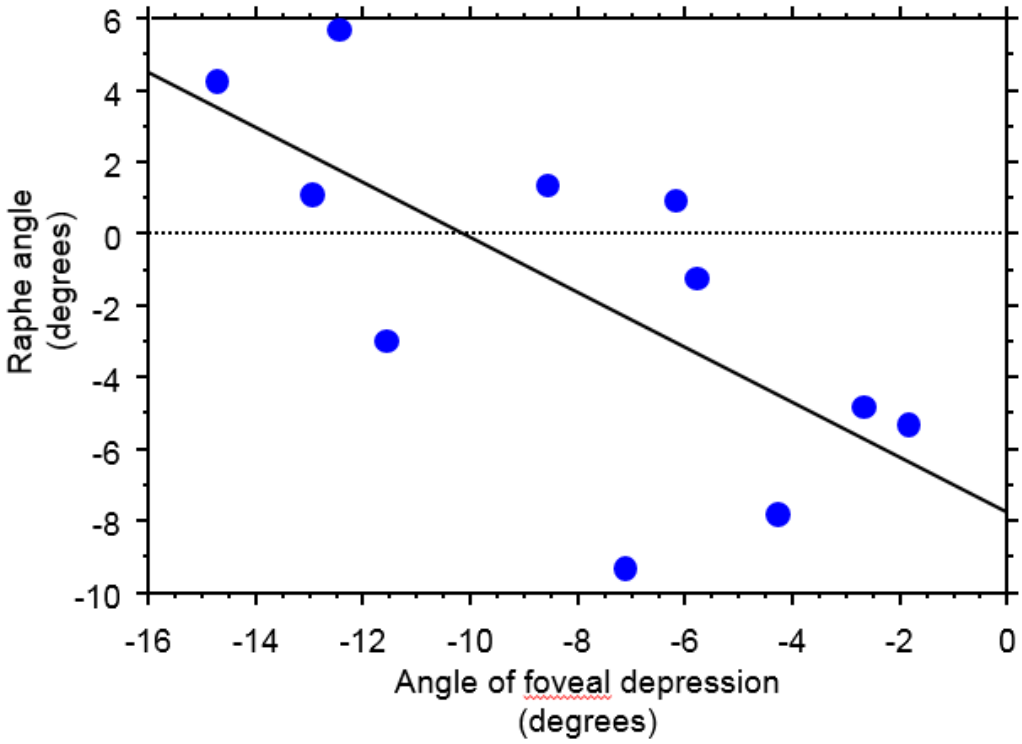

Figure 8. Relation of the raphe angle to the angle of foveal depression in the younger subjects (Group 1).

Aging effect on the raphe gap

While the raphe gap was quite small or even non-existent due to interleaving of the superior and inferior bundles in the young eyes, the gap increased in the older eyes and interleaving of bundles was not observed in any of these older subjects. As a result, the averaged raphe gap at 9-degree eccentricity was significantly different between the two

groups (Group 1, 1.93 ± 68.73 µm, Group 2, 230.83 ± 113.22 µm, p<0.0001), as shown in Figure 9.

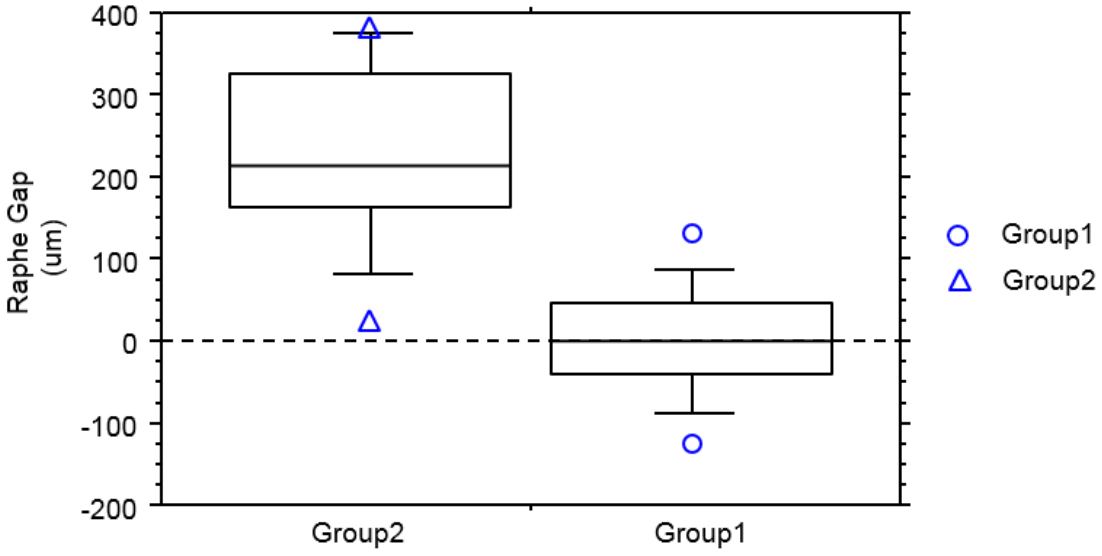

Figure 9. Box and whiskers plot for comparison of the raphe gap (defined in text) between the younger subjects (Group 1) and older subjects (Group 2). The averaged gap for each subject was computed by averaging the raphe gaps between 8 and 10-degree eccentricity. For each plot, the five horizontal lines represent 90%, 75%, 50%, 25%, 10% of the population distribution, and the individual data points above the 90% or below the 10% are also plotted individually in the plot. The raphe gap in the two groups are significantly different (Group 1: 1.93 ± 68.73 µm, Group 2: 230.83 ± 113.22 µm, t-test, p<0.0001).

4.4 Discussion

The purpose of this study was to explore the raphe's morphology in both younger and older healthy subjects. The *in vivo* images have shown that the raphe appearance can vary considerably with retinal eccentricity. The quantitative analysis suggests the raphe's geometry in the retina is neither strictly horizontal to the fovea nor to the optic disc. Instead, the lower the fovea is relative to the disc, the more downward the angle of the raphe, suggesting a new view of the raphe's geometry which could be important in the proper interpretation of visual fields.

The morphology of the raphe has been described in several independent *ex vivo* studies, although not all the reports were consistent with our findings(Ballantyne, 1947; Vrabec, 1966). Some studies reported that the superior and inferior bundles stopped right at the raphe while others reported that bundles could cross the raphe as we found in some of our subjects. The interleaving of bundles observed in our study confirmed that there could frequently be some degree of overlap between projections to the superior and inferior regions of the disc. The overlap could cause some blurring of the visual field deficit across the raphe. That is, for a person with glaucomatous damage localized to either the superior or inferior areas of the disc, this raphe anatomy could lead to visual field loss which did not respect a 'horizontal' meridian. In the older subjects, no such overlap of the superior and inferior bundles was visible. We interpret this as likely a consequence of the increased raphe gap, and we interpret the increased raphe gap as a

consequence of both a decreased visibility of bundles with age and perhaps as a sign of the ongoing loss of ganglion cells with age (see below).

The dark-band raphe that we observed in the region close to the fovea in the young eyes suggests that bundles were smaller here than in regions that were further away. While scatter or inadequate AO control could cause a failure to resolve these small fibers, this is unlikely because these eyes were young and we observed small bundles in nearby regions in the same eyes.

In all studies, including ours, a transitional area occurs where peripheral, radially oriented bundles begin to arc around the macula. Closer to the fovea than the transition area, ganglion cells will project their axons directly away from the raphe, with a course towards either the superior or inferior portion of the disc, with the probability of either projection depending on the location. Peripheral to the transition area, ganglion cells initially send axons approximately towards the disc, but those axons deviate from their radial traverse at the transition area and curve superiorly or inferiorly around the fovea.

Our data shows that the raphe's appearance is affected by aging. The enlarged raphe gap in the older subjects is presumably occurring due to either poor optics that we are not fully compensating (for instance very high frequency aberrations of the tear film), due to optical changes with age (McLellan, Marcos, & Burns, 2001), or due to axonal loss with aging (Curcio & Drucker, 1993; Gao & Hollyfield, 1992) . Because we still see quite small bundles, just displaced from the raphe center we do not believe it is fully

attributable to optical changes although the well-known change in the retinal reflex with age supports a change in overall reflectivity. We also know that there are changing numbers of ganglion cells and axonal bundles with age. It is possible that the thinning of the RNFL seen with aging in OCT images (Alasil et al., 2013), is manifest here by reducing bundle sizes to the point that they are not visible and thus form a larger gap. This sort of phenomenon likely would be visible only in a retinal area in which there is a transition from no visible bundles to definitely visible bundles and would not be measured in areas of densely overlapping bundles such as near the vascular arcades. This change is most likely the locally visible evidence of a global loss of nerve fibers due to aging.

Despite of the variance of the raphe's appearance across subjects, the shape of the raphe can be approximately described as a straight line. In our study, we further evaluated the goodness of straight-line fit by computing residual errors between the raphe's positions and fitted raphe line for eccentricities imaged in each young subject. The analysis showed that the residual errors ranged from -0.4 degrees to +0.4 degrees approximately, as shown in Figure 10. The error range could be neglected for some of clinical testing, for example, visual field testing, in which the raphe is typically assumed as a line in the temporal retina. A 24-2 visual field sets 3 degrees as a typical angular distance between the raphe's position and the nearest visual field testing points. The chance that a field defect pattern is misinterpreted due to a 0.4 degree modelling error is small.

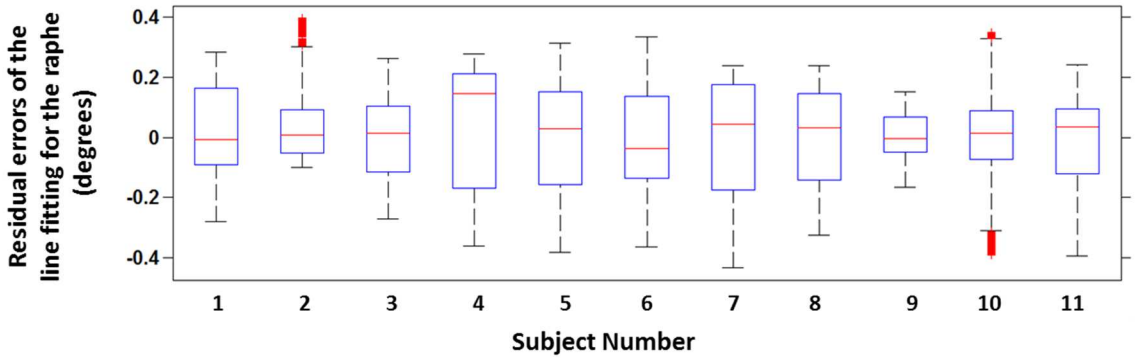

Figure 10. Box and whiskers plot for residual errors of the line fitting for the raphe across the younger subjects (Group 1). For each box, the three horizontal lines represent 75%, median and 25% of the error distribution. The ends of the whisker represent the lowest datum within 1.5 interquartile range (IQR) of the quartile and the highest datum within 1.5 IQR of the upper quartile respectively. The errors across the subjects range from approximately -0.4 to 0.4 degrees.

What remains unexplored in all *ex vivo* studies is the geometrical relation of the temporal raphe to other parts of the retina. Traditionally, there have been two theoretical models relating the temporal raphe location to overall retinal structure. The first model assumes that the temporal raphe is lined up with the center of the optic disc. The second one assumes the temporal raphe is a horizontal line extending from the fovea. Both models have been used for various clinical applications. For example, the first model is used in the Posterior Pole Asymmetry Analysis, and the second model is used to interpret visual field defects in the nasal visual field.

However, each model is inconsistent with the results of our study. The first model is very unlikely to be correct based on the result in Figure 7 where the total angle between the raphe and optic disc is on averaged 170 degrees, and never reaches 180 degrees for any subject of this study. The second model is also unlikely to be correct as suggested by Figures 6-8. Although the averaged angle of the raphe among subjects is close to zero degrees as shown in Figure 6, the individual variance across these subjects is relatively large, which is unlikely caused purely due to the angular deviation in the line model. For example, the angle in some individuals can reach more than 5 degrees off the horizontal midline.

There are several sources possibly attributed to the large individual variance of the raphe angle. The first one is the linkage between the raphe angle and foveal depression as suggested in Figure 8. The slope of the regression line for the relation between raphe and depression angles is much closer to the slope of 1 than the slope of 0. This is unlikely to be caused by a bias in the measured foveal depression angles because they varied from -2 degrees to -15 degrees across individuals in our study, very similar to results of other studies (Choi, Kim, Park, Park, & Park, 2014; Garway-Heath et al., 2000; Lamparter et al., 2013; Lefevre, Leroy, Delrieu, Lassale, & Pechereau, 2007).

Other possible sources attributed to the raphe angle variance include subjects' head position and measurement errors of identifying the disc center, fovea, and raphe. Future

studies are warranted to investigate the roles of these sources of variance on the raphe angle measurement.

Clinical Implications

The inconsistency of the two raphe models discussed above with the data suggests that there are clinical implications, since many measurements are based on these models. For example, glaucoma specialists use the horizontal raphe model to interpret results in the nasal field. However, for a subject who has an 8-degree raphe angle as shown for one of our subjects, the vertical deviation between the model and the subject's raphe can reach up to 2.8 degrees when we look at field locations that are beyond 20 degrees in the nasal field. This deviation is large enough that at least the two outermost nasal inferior locations of the 24-2 visual field should in fact be assigned to the opposite hemisphere for that subject. This could possibly explain some of the nasal steps that extend across the horizontal meridian. It is possible that they are not actually extending across the anatomic raphe in a particular patient.

Besides the visual field, there has been a trend of performing asymmetry analysis of the central macular thickness to evaluate glaucoma damage. The analysis uses the raphe as a retinal hemisphere boundary in the temporal retina, and compares the thickness of the regions that are located symmetric to the raphe. Obviously a choice of the wrong raphe model can cause incorrect pairing of regions and distort the asymmetry analysis.

We conclude that the raphe's geometry cannot be ignored as it might be closely related to how the clinical data is analyzed and interpreted. With rapid developments of retinal imaging devices, the identification of the raphe for individual patients in clinics can be realistic. For instance, recent studies reported imaging the raphe with medium lateral resolution using OCT transverse images (Laura de Polo AI, et al. IOVS 2013; 45: ARVO E-Abstract 4815). Although the resolution of those images is not as good as the AOSLO images, the raphe geometry can be measured. These individual raphe images could enable personalized visual fields and asymmetry analysis in the near future.

4.5 Conclusions

The detailed *in vivo* morphology of the temporal raphe was shown in AOSLO images. These *in vivo* images were generally in agreement with major findings of *ex vivo* studies. Further quantitative analysis showed a relatively large individual range of the raphe angle and indicated its possible linkage to the angle of foveal depression. The angle between the raphe and the line that connects the fovea and disc center was on average 170 degrees. These results were not consistent with the two classic raphe models; one that the raphe is horizontal and in line with the fovea, and the other that the raphe is lined up with the optic disc. For clinical diagnostic instruments and approaches that uses the raphe's geometry models, either a new model or an approach of getting a personalized raphe image may help to further improve understanding of the relation between visual field deficits and structural imaging.

4.6 Acknowledgements

The authors acknowledge William H Swanson Ph.D for helpful discussion; Luo Ting MS for her comments on data analysis. This work was supported by NIH grants R01 EY04395 and P30EY019008.

4.7 Reference

Alasil, T., Wang, K. D., Keane, P. A., Lee, H., Baniasadi, N., Boer, J. F., & Chen, T. C. (2013). Analysis of Normal Retinal Nerve Fiber Layer Thickness by Age, Sex, and Race Using Spectral Domain Optical Coherence Tomography. *J Glaucoma, 22*(7), 532-541. doi: Doi 10.1097/Ijg.0b013e318255bb4a

Armaly, M. F. (1971). Visual field defects in early open angle glaucoma. *Trans Am Ophthalmol Soc, 69*, 147-162.

Ballantyne, A. J. (1947). The nerve fiber pattern of the human retina. *Tr. Ophth. Soc. U. Kingdom,*, 66:179.

Bedggood, P., Daaboul, M., Ashman, R., Smith, G., & Metha, A. (2008). Characteristics of the human isoplanatic patch and implications for adaptive optics retinal imaging. *J Biomed Opt, 13*(2), 024008. doi: 10.1117/1.2907211

Choi, J. A., Kim, J. S., Park, H. Y., Park, H., & Park, C. K. (2014). The foveal position relative to the optic disc and the retinal nerve fiber layer thickness profile in myopia. *Invest Ophthalmol Vis Sci, 55*(3), 1419-1426. doi: 10.1167/iovs.13-13604

Chui, T. Y., Gast, T. J., & Burns, S. A. (2013). Imaging of vascular wall fine structure in the human retina using adaptive optics scanning laser ophthalmoscopy. *Invest Ophthalmol Vis Sci, 54*(10), 7115-7124. doi: 10.1167/iovs.13-13027

Chui, T. Y., Song, H., & Burns, S. A. (2008). Adaptive-optics imaging of human cone photoreceptor distribution. *J Opt Soc Am A Opt Image Sci Vis, 25*(12), 3021-3029. doi: 10.1364/josaa.25.003021

Curcio, C. A., & Drucker, D. N. (1993). Retinal Ganglion-Cells in Alzheimers-Disease and Aging. *Annals of Neurology, 33*(3), 248-257. doi: DOI 10.1002/ana.410330305

Dubra, A., & Sulai, Y. (2011). Reflective afocal broadband adaptive optics scanning ophthalmoscope. *Biomed Opt Express, 2*(6), 1757-1768. doi: 10.1364/BOE.2.001757

Ferguson, R. D., Zhong, Z., Hammer, D. X., Mujat, M., Patel, A. H., Deng, C., . . . Burns, S. A. (2010). Adaptive optics scanning laser ophthalmoscope with integrated wide-field retinal imaging and tracking. *J Opt Soc Am A Opt Image Sci Vis, 27*(11), A265-277. doi: 10.1364/JOSAA.27.00A265

Gao, H., & Hollyfield, J. G. (1992). Aging of the human retina. Differential loss of neurons and retinal pigment epithelial cells. *Invest Ophthalmol Vis Sci, 33*(1), 1-17.

Garway-Heath, D. F., Poinoosawmy, D., Fitzke, F. W., & Hitchings, R. A. (2000). Mapping the visual field to the optic disc in normal tension glaucoma eyes. *Ophthalmology, 107*(10), 1809-1815.

Hart, W. M., Jr., & Becker, B. (1982). The onset and evolution of glaucomatous visual field defects. *Ophthalmology, 89*(3), 268-279.

Hood, D. C., Raza, A. S., de Moraes, C. G., Johnson, C. A., Liebmann, J. M., & Ritch, R. (2012). The Nature of Macular Damage in Glaucoma as Revealed by Averaging

Optical Coherence Tomography Data. *Transl Vis Sci Technol, 1*(1), 3. doi: 10.1167/tvst.1.1.3

Hood, D. C., Raza, A. S., de Moraes, C. G., Liebmann, J. M., & Ritch, R. (2013). Glaucomatous damage of the macula. *Prog Retin Eye Res, 32*, 1-21. doi: 10.1016/j.preteyeres.2012.08.003

Huang, D., Swanson, E. A., Lin, C. P., Schuman, J. S., Stinson, W. G., Chang, W., . . . et al. (1991). Optical coherence tomography. *Science, 254*(5035), 1178-1181.

Huang, G., Qi, X., Chui, T. Y., Zhong, Z., & Burns, S. A. (2012). A clinical planning module for adaptive optics SLO imaging. *Optom Vis Sci, 89*(5), 593-601. doi: 10.1097/OPX.0b013e318253e081

Jansonius, N. M., Nevalainen, J., Selig, B., Zangwill, L. M., Sample, P. A., Budde, W. M., . . . Schiefer, U. (2009). A mathematical description of nerve fiber bundle trajectories and their variability in the human retina. *Vision Res, 49*(17), 2157-2163. doi: 10.1016/j.visres.2009.04.029

Jansonius, N. M., Schiefer, J., Nevalainen, J., Paetzold, J., & Schiefer, U. (2012). A mathematical model for describing the retinal nerve fiber bundle trajectories in the human eye: average course, variability, and influence of refraction, optic disc size and optic disc position. *Exp Eye Res, 105*, 70-78. doi: 10.1016/j.exer.2012.10.008

Kocaoglu, O. P., Cense, B., Jonnal, R. S., Wang, Q., Lee, S., Gao, W., & Miller, D. T. (2011). Imaging retinal nerve fiber bundles using optical coherence tomography with adaptive optics. *Vision Res, 51*(16), 1835-1844. doi: 10.1016/j.visres.2011.06.013

Lamparter, J., Russell, R. A., Zhu, H., Asaoka, R., Yamashita, T., Ho, T., & Garway-Heath, D. F. (2013). The influence of intersubject variability in ocular anatomical variables on the mapping of retinal locations to the retinal nerve fiber layer and optic nerve head. *Invest Ophthalmol Vis Sci, 54*(9), 6074-6082. doi: 10.1167/iovs.13-11902

Lee, A. J., Wang, J. J., Rochtchina, E., Healey, P., Chia, E. M., & Mitchell, P. (2003). Patterns of glaucomatous visual field defects in an older population: the Blue Mountains Eye Study. *Clin Experiment Ophthalmol, 31*(4), 331-335.

Lefevre, F., Leroy, K., Delrieu, B., Lassale, D., & Pechereau, A. (2007). [Study of the optic nerve head-fovea angle with retinophotography in healthy patients]. *J Fr Ophtalmol, 30*(6), 598-606.

McLellan, J. S., Marcos, S., & Burns, S. A. (2001). Age-related changes in monochromatic wave aberrations of the human eye. *Invest Ophthalmol Vis Sci, 42*(6), 1390-1395.

Merino, D., Duncan, J. L., Tiruveedhula, P., & Roorda, A. (2011). Observation of cone and rod photoreceptors in normal subjects and patients using a new generation adaptive optics scanning laser ophthalmoscope. *Biomed Opt Express, 2*(8), 2189-2201. doi: 10.1364/BOE.2.002189

Nowakowski, M., Sheehan, M., Neal, D., & Goncharov, A. V. (2012). Investigation of the isoplanatic patch and wavefront aberration along the pupillary axis compared to the line of sight in the eye. *Biomed Opt Express, 3*(2), 240-258. doi: 10.1364/BOE.3.000240

Roorda, A., Romero-Borja, F., Donnelly Iii, W., Queener, H., Hebert, T., & Campbell, M. (2002). Adaptive optics scanning laser ophthalmoscopy. *Opt Express, 10*(9), 405-412. doi: 68843 [pii]

Schiefer, U., Flad, M., Stumpp, F., Malsam, A., Paetzold, J., Vonthein, R., . . . Sample, P. A. (2003). Increased detection rate of glaucomatous visual field damage with locally condensed grids: a comparison between fundus-oriented perimetry and conventional visual field examination. *Arch Ophthalmol, 121*(4), 458-465. doi: 10.1001/archopht.121.4.458

Schuman, J. S., Hee, M. R., Puliafito, C. A., Wong, C., Pedut-Kloizman, T., Lin, C. P., . . . Fujimoto, J. G. (1995). Quantification of nerve fiber layer thickness in normal and glaucomatous eyes using optical coherence tomography. *Arch Ophthalmol, 113*(5), 586-596.

Song, H., Chui, T. Y., Zhong, Z., Elsner, A. E., & Burns, S. A. (2011). Variation of cone photoreceptor packing density with retinal eccentricity and age. *Invest Ophthalmol Vis Sci, 52*(10), 7376-7384. doi: 10.1167/iovs.11-7199

Takayama, K., Ooto, S., Hangai, M., Arakawa, N., Oshima, S., Shibata, N., . . . Yoshimura, N. (2012). High-resolution imaging of the retinal nerve fiber layer in normal eyes using adaptive optics scanning laser ophthalmoscopy. *PLoS One, 7*(3), e33158. doi: 10.1371/journal.pone.0033158

Takayama, K., Ooto, S., Hangai, M., Ueda-Arakawa, N., Yoshida, S., Akagi, T., . . . Yoshimura, N. (2013). High-resolution imaging of retinal nerve fiber bundles in glaucoma using adaptive optics scanning laser ophthalmoscopy. *Am J Ophthalmol, 155*(5), 870-881. doi: 10.1016/j.ajo.2012.11.016

Tam, J., Tiruveedhula, P., & Roorda, A. (2011). Characterization of single-file flow through human retinal parafoveal capillaries using an adaptive optics scanning laser ophthalmoscope. *Biomed Opt Express, 2*(4), 781-793. doi: 10.1364/BOE.2.000781

Vrabec, F. (1966). The temporal raphe of the human retina. *Am J Ophthalmol, 62*(5), 926-938.

Weber, J., & Ulrich, H. (1991). A perimetric nerve fiber bundle map. *Int Ophthalmol, 15*(3), 193-200.

Werner, E. B., & Drance, S. M. (1977). Early visual field disturbances in glaucoma. *Arch Ophthalmol, 95*(7), 1173-1175.

Zhong, Z., Huang, G., Chui, T. Y., Petrig, B. L., & Burns, S. A. (2012). Local flicker stimulation evokes local retinal blood velocity changes. *J Vis, 12*(6), 3. doi: 10.1167/12.6.3

Zhong, Z., Song, H., Chui, T. Y., Petrig, B. L., & Burns, S. A. (2011). Noninvasive measurements and analysis of blood velocity profiles in human retinal vessels. *Invest Ophthalmol Vis Sci, 52*(7), 4151-4157. doi: 10.1167/iovs.10-6940

Chapter 5: Imaging Glaucomatous Damage across the Temporal Raphe

ABSTRACT

Purpose: To image and analyze anatomical differences at the temporal raphe between normal and glaucomatous eyes using adaptive optics scanning laser ophthalmoscopy (AOSLO) and optical coherence tomography (OCT), and to relate these differences to visual field measurements.

Methods: Nine glaucomatous eyes of 9 patients (Age: 54-78, Mean deviation of visual field (MD): -5.03 to -0.20 dB) and ten normal eyes of 10 controls (Age: 54-81, MD: -1.13 dB to +1.39 dB) were enrolled. All the participants were imaged in a region that was centered approximately 9° temporal to the fovea. The size of imaging region was at least 10° vertically by 4° horizontally. The raphe gap, defined as the distance between the superior and inferior RNFL bundles was measured. A bundle index was computed to quantify the relative reflectivity and density of the nerve fiber bundles. We also measured thickness of the ganglion cell complex (GCC) and retinal nerve fiber layer (RNFL).

Results: The raphe gap was larger in glaucomatous eyes than control eyes. Specifically, 8 glaucomatous eyes with local averaged field loss no worse than -3.5 dB had larger raphe gaps than all control eyes. The bundle index, GCC thickness, and RNFL thickness were on average reduced in glaucomatous eyes, with the first two showing statistically significant differences between the two groups.

Conclusion: Structural changes in the temporal raphe were observed and measured even when local functional loss was mild. It opened the possibility of using the raphe as a site for glaucoma research and clinical assessment.

5.1 Introduction

Glaucoma is a group of blinding optic neuropathies that represent a major irreversible cause of vision loss in the elderly. The disease is characterized by damage to the ganglion cells and their axons and a resulting thinning of the retinal nerve fiber layer (RNFL) and cupping of the optic disc. The damage leads to a related loss in visual function.

Because the vision loss resulting from glaucoma is irreversible, it is important to detect glaucoma in its early stages and to carefully monitor status as the disease progresses. In practice, this requires both functional and structural measurements. The current "gold" standard for testing visual function is visual field testing performed using static automated perimetry (SAP). For a given eye, visual sensitivity is measured at discrete retinal locations, and compared to normative values. As glaucoma progresses, the visual defects often appear in certain distinct locations, for instance, arcuate defects, paracentral scotomas, and nasal steps. A major disadvantage of visual field testing is that there is large individual variability (Artes, Iwase, Ohno, Kitazawa, & Chauhan, 2002; Heijl, Lindgren, & Lindgren, 1989; Piltz & Starita, 1990), and this variability, because it lowers the sensitivity for detecting glaucoma, has led to an increased emphasis on measurements of changes to retinal structure as a complement to visual field testing.

Traditionally, structural measures of glaucomatous damage relied on fundus cameras and confocal scanning laser ophthalmoscopy (SLO) for evaluating the optic disc and

imaging RNFL defects (Airaksinen & Alanko, 1983; Airaksinen, Drance, Douglas, Mawson, & Nieminen, 1984; Airaksinen, Drance, Douglas, Schulzer, & Wijsman, 1985; Hoyt, Frisen, & Newman, 1973; Rohrschneider, Burk, Kruse, & Volcker, 1994; Sommer, D'Anna, Kues, & George, 1983; Wollstein, Garway-Heath, & Hitchings, 1998), and scanning laser polarimetry for evaluation of the peripapillary RNFL(Dreher & Reiter, 1992). Recently, optical coherence tomography (OCT) has been increasingly used to detect and monitor glaucomatous damage to the RNFL (Schuman et al., 1995), because of its high axial resolution and ability to quantify changes in the thickness of individual retinal layers. Another technique that was brought to the retinal imaging field is adaptive optics (AO) imaging, which allows for high-resolution retinal imaging without degradation by ocular aberrations (Liang, Williams, & Miller, 1997). AO retinal imaging has been employed for investigation of glaucomatous damage of nerve fiber bundles in human eyes (Chen et al., 2015; Takayama et al., 2013). However, most of current imaging-based measures were applied near the optic disc, where the RNFL is the thickest. Imaging at this location has the advantage that all ganglion cell axons must exit the eye at the optic disc, so the analysis can concentrate on this area and provide a summed measure of the axons. However it also has the disadvantage that while there are general spatial relations between locations in the visual field and the thickness of the RNFL at particular portions of the optic disc and peripapillary region, there is large individual variability in this relation and so relating a particular structural measurement to a particular region of the visual field can be challenging (Anton, Yamagishi, Zangwill, Sample, & Weinreb, 1998; Denniss, Turpin, & McKendrick, 2014; Garway-Heath, Poinoosawmy, Fitzke, & Hitchings, 2000; Jansonius, Schiefer, Nevalainen, Paetzold, &

Schiefer, 2012; Lamparter et al., 2013; Weber, Dannheim, & Dannheim, 1990; Wirtschafter, Becker, Howe, & Younge, 1982; Yamagishi et al., 1997).

An apparent solution is to look at structural changes to the RNFL closer to the locations of the measured visual field defects. One portion of the retina where this becomes possible is near the temporal raphe in the temporal retina. In this region, the ganglion cell axons are first incorporated into axon bundles, and then course across the retina towards the optic disc. For eccentricities around 9° temporal to the fovea, the ganglion cells have relatively small displacement from the position of their cone inner segments, and thus there is a close spatial relation between the local sensitivity and the local RNFL (Curcio & Allen, 1990; Drasdo, Millican, Katholl, & Curcio, 2007). This region also has an advantage for studying the relation of early structural and functional loss because the raphe region is believed to be one of the major sites where early visual function abnormalities appear (Armaly, 1971; Hart & Becker, 1982; Lee et al., 2003; Werner & Drance, 1977).

Unfortunately most clinical techniques cannot measure the RNFL reliably near the raphe because the RNFL is relatively thin and has low contrast. In the past few years, efforts have been made to image and measure the RNFL in this region using high-resolution imaging techniques. In particular, the adaptive optics scanning laser ophthalmoscope (AOSLO) has demonstrated the ability to image the temporal raphe in healthy young subjects (Huang, Gast, & Burns, 2014; Huang, Qi, Chui, Zhong, & Burns,

2012). Similarly, the latest OCT techniques have been demonstrated to image the temporal raphe (Chauhan, Sharpe, & Hutchison, 2014).

The current study used an AOSLO to measure *en face* structure of the RNFL near the raphe and a commercial OCT to measure the thickness of the RNFL and ganglion cell complex (GCC) in the same region, and related these measurements to visual sensitivity as measured using SAP in patients with glaucoma and control subjects.

5.2 Methods

Subjects

For the current study, we selected 9 glaucomatous eyes of 9 patients (54-78 years old, mean 65.6 years, SD 6.7; 4 men and 5 women) and 10 control eyes of 10 age-similar subjects (54-81 years, mean 66.3 years old, SD 6.8; 5 men and 5 women). All these subjects were drawn from the subject pool of an recently completed multicenter glaucoma longitudinal study (Swanson et al., 2014), which adhered to the tenets of the Declaration of Helsinki and was approved by the institutional review boards at SUNY College of Optometry and at Indiana University. Common inclusion criteria for both groups were: best corrected visual acuity of 20/20 or better (20/25 for subjects over age 70), spherical equivalent within -6 D to +2 D, cylinder correction less than 3 D, absence of known ocular or systemic disease known to affect the visual field (except for glaucoma

in the patient group), and history of reliable visual fields. Common exclusion criteria for both groups were: failure of pupil dilation, significant cataract, or inability to stably fixate for OCT or AOSLO imaging.

All patients had abnormal appearing discs consistent with glaucoma, both on clinical examinations and OCT images. Among these 9 glaucomatous eyes, 7 eyes had asymmetric visual field sensitivity loss across the horizontal midline in the nasal field and 2 eyes had no visual field loss in the nasal field. The MD ranged from -5.03 dB to -0.20 dB (mean -1.88 ± 1.64 dB) in the glaucoma group, and ranged from -1.13 dB to +1.39 dB (mean 0.03 ± 0.64 dB) in the control group. The vertical cup/disc ratio was 0.40-0.74 (mean 0.49 ± 0.14) in the patient group, and 0.23-0.47 (mean 0.39 ± 0.09) in the control group. The mean axial length was 22.89-26.16mm (mean 25.1 ± 1.4 mm) in the patient group, and was 22.88-25.98mm (mean 24.5 ± 1.2 mm) in the control group.

All subjects went through a full eye examination by an ophthalmologist prior to the imaging sessions. Consent forms were signed by each subject, after a full explanation of procedures and consequen1ces of this study. All studied eyes were dilated using 0.5% tropicamide. The study protocol was approved by Indiana University Institutional Review Board and is in accordance with the Declaration of Helsinki.

The Indiana Adaptive Optics Scanning Laser Ophthalmoscope with clinical planning module

The wide-field AOSLO equipped with a clinical planning module (Huang et al., 2012) has been presented previously. In brief, the AOSLO employed a super-continuum laser source (NKT Photonics, Birkerød, Denmark) as the illumination source, which can provide imaging wavelengths from 450-900 nm, although we only used 820-840 nm in this study. The AOSLO uses two deformable mirrors and a wave-front sensor to correct ocular monochromatic aberrations in a close-loop feedback system. The imaging field is approximately 2° by 1.8° and can be steered over at least 20° on the retina. A digital projector was incorporated in the system to provide a programmable fixation target for subjects. To image retinal regions larger than 2° by 1.8°, it is necessary to steer the AOSLO imaging beam across the retina, acquiring sequential video images at multiple positions to cover the area of interest.

Procedures

1) Imaging

An imaging session consisted of three portions. Firstly, the axial length was measured with an IOLMaster (Carl Zeiss Meditec, Dublin, CA). Secondly, the eye was imaged

with a Heidelberg Spectralis ™ SLO/OCT system (Heidelberg Engineering, Heidelberg, Germany), and thirdly the eye was imaged with the AOSLO.

For SLO/OCT imaging, we first obtained 30° by 30° SLO images with the Spectralis, which are centered at the fovea and at approximately 12° temporal to the fovea respectively. These two images were used to construct a mosaic fundus image using the Heidelberg built-in software, as indicated in Figure 1. Then, we performed OCT imaging in the temporal retina and macular region. For the temporal retina, the OCT imaging field size was 15° horizontally by 15° vertically, and the imaging field was centered at approximately 12° temporal to the fovea. Each B-scan was oriented in the vertical direction. The distance between adjacent B-scans was 60 μm. The macular region was imaged using two perpendicular OCT volume scans to allow accurate localization of the fovea. The first used vertical B-scans while the other had horizontal B-scans. The scanning size was 15° by 5°. Adjacent B-scans were separated by 30 μm. Imaging locations for OCT are indicated in Figure 1.

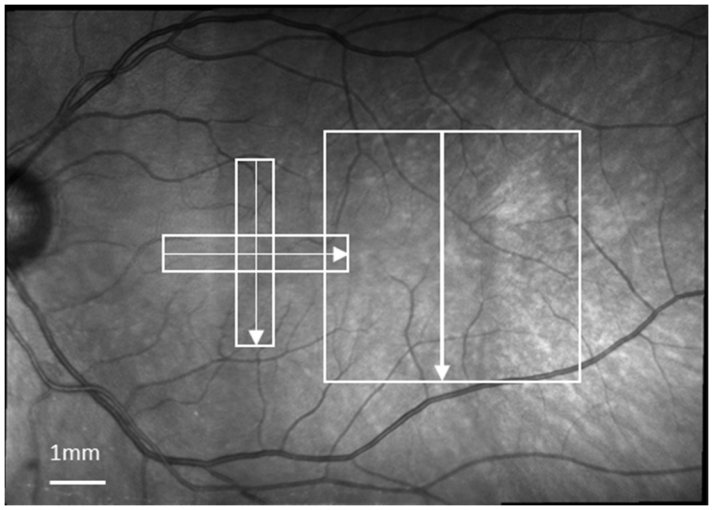

Figure 1. A fundus mosaic constructed from two 30° by 30° wide-field SLO images, using the Heidelberg built-in software. The white boxes in the mosaic indicate the regions and directions (arrows) of OCT scans. The two orthogonal OCT volume scans were centered on the fovea. The third volume scan was centered at approximately 12° temporal to the fovea.

For AOSLO imaging, the imaging region was centered approximately 9° temporal to the fovea, and the size of the region was at least 10° vertically by 4° horizontally. For each imaging field location, the AOSLO collected 75 images at a 30Hz frame rate. The adjacent fields had approximately 0.5° or more of overlap. Subjects were allowed to take breaks during imaging. The whole procedure for AOSLO imaging including the subject's break time took between 20 and 50 minutes depending on the subject.

2) Post-processing of AOSLO images and formation of montages

Removal of eye movements and averaging of video frames were performed in MATLAB™ (the Mathworks Inc, Natick, MA). Montages were then created manually using Photoshop CS6 (Adobe Systems, San Jose, CA). Images from spatially-adjacent regions were first aligned. Then, for each raw montage, we adjusted the brightness of images to match neighboring images visually, using a Photoshop built-in brightness adjustment which is a linear process. Finally, we used Photoshop to manually register the resulting AOSLO montage with the wide-field SLO image acquired by the Spectralis (see Figure 2a and 2b).

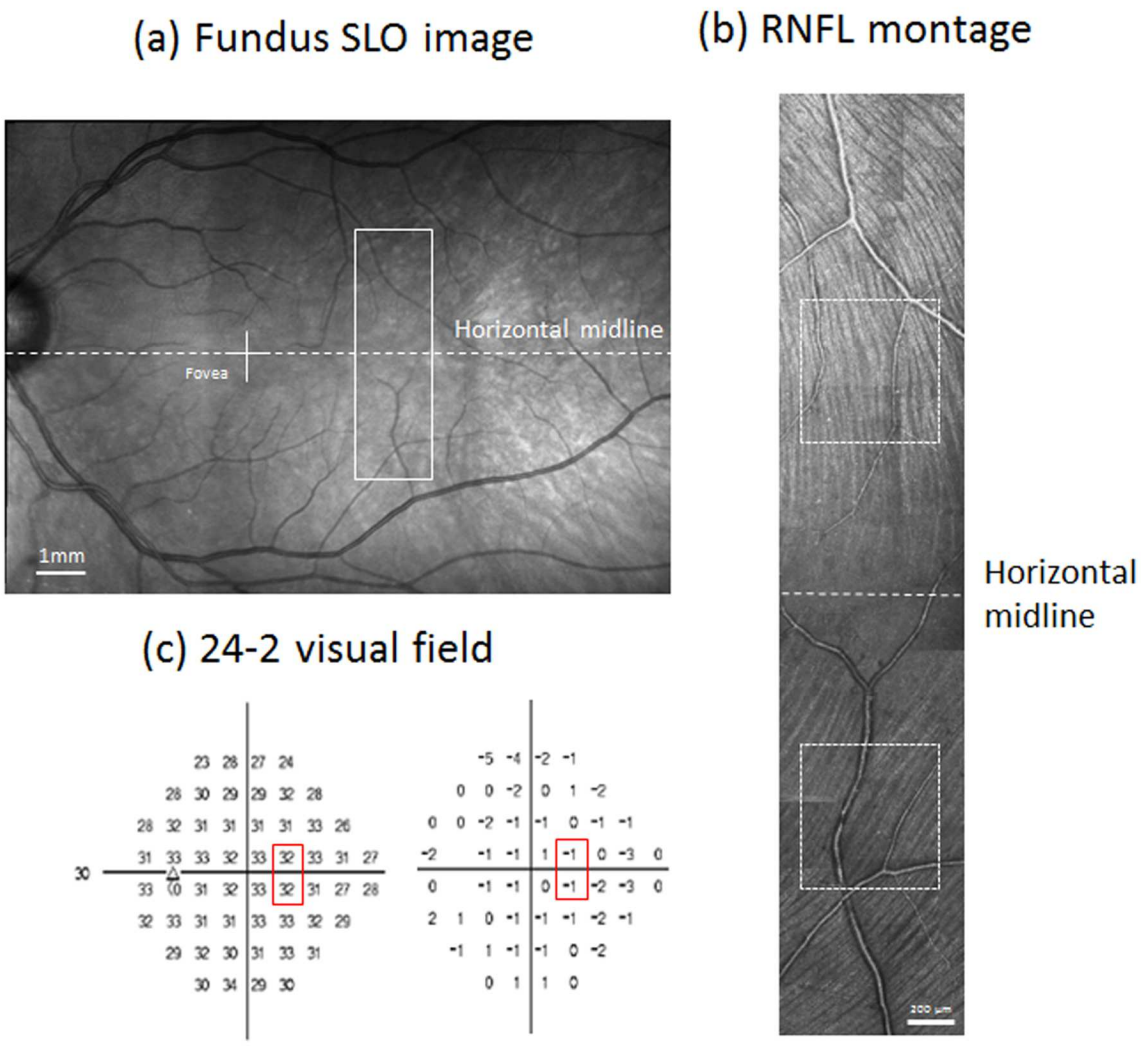

Figure 2. (a) A wide-field fundus mosaic of a control subject. The white cross indicates the fovea. The white box with solid lines indicates approximately where AOSLO imaging was performed. The horizontal dashed line is the horizontal midline of the retina drawn through the fovea and defines the horizontal midline for the visual field. (b) RNFL montage of the same control subject constructed from AOSLO images. Brightness of each image was adjusted to minimize the transition between images. The white boxes

indicate regions where the bundle index was computed for this subject (see text for details). The dashed line indicates the midline of the retina. (c) Sensitivity map (left) and total deviation map (right) of a 24-2 visual field for the same control subject. The red boxes indicate the stimulus locations that fell within the AOSLO imaging region.

3) Alignments between the AOSLO, OCT and visual field

To compare outcomes that were acquired from these three techniques, it was necessary to set up a common coordinate system. This was performed in two steps. First, the fovea was identified in SLO/OCT images. Using the horizontal and vertical OCT cross sections of the fovea, we identified the center of the foveal depression and referred this to the SLO image using Heidelberg's built-in OCT/SLO display. Next, we assumed that the horizontal scan of the OCT/SLO corresponded to the horizontal axis of the visual field, and thus we could equate the visual field location to the OCT/SLO images and measurements. AOSLO montages had been registered to SLO images and thus can be related to the visual field locations by using SLO images as bridges.

4) Regions/locations of measurements

For visual fields, we selected the one at 9°nasal, 3°superior field, and the one at 9°nasal, 3°inferior field for analysis. For each AOSLO montage, we picked two regions that are central to these two visual field locations respectively. The size of each region was set as

~2 by 2 degrees. For OCT B-scan images that were across each region, we selected the image that is closest to the center of the region, and then we selected another two images that were each approximately 180 μm away from the central one. The parts of these three OCT images that fall in the region were used for further analysis.

Quantitative Measurements

1) Measurement of the raphe gap

For each RNFL AOSLO montage, we manually measured the raphe gap defined as the vertical distance between the boundaries of visible superior and inferior nerve fiber bundles. Specifically, for each side of the raphe (superior or inferior), a grader, masked to all relevant clinical information including all visual field reports and diagnostic reports, identified the three longest bundles that could be observed in the montage. Then, the tip of each bundle was marked, and their averaged vertical position was used as the boundary for the side. The raphe gap of a given eccentricity was then computed as the mean vertical distance between the superior and inferior bundle boundaries at that eccentricity (e.g., Figure 3). To compare data across subjects, distances were adjusted for individual differences in axial length, according to the Gullstrand model eye. To improve the reliability of the grading we had two graders independently make these measurements and used the averaged results. Note that the measured raphe gap may not necessarily represent a region totally lacking bundles and axons. The diameters of ganglion cell axons in the RNFL can range from 0.1 μm to more than 2 μm (FitzGibbon & Taylor, 2012; Ogden, 1984) and thus axons and bundles could be unrecognizable in AOSLO

images. Thus, the measured gap could contain axons too small to be resolved. That is, our measurements could be larger than the 'true gap' lacking any bundles, however this same limitation is present for both glaucomatous and control eyes, assuming the optics and other aspects controlling the contrast of images are similar and are independent of glaucoma.

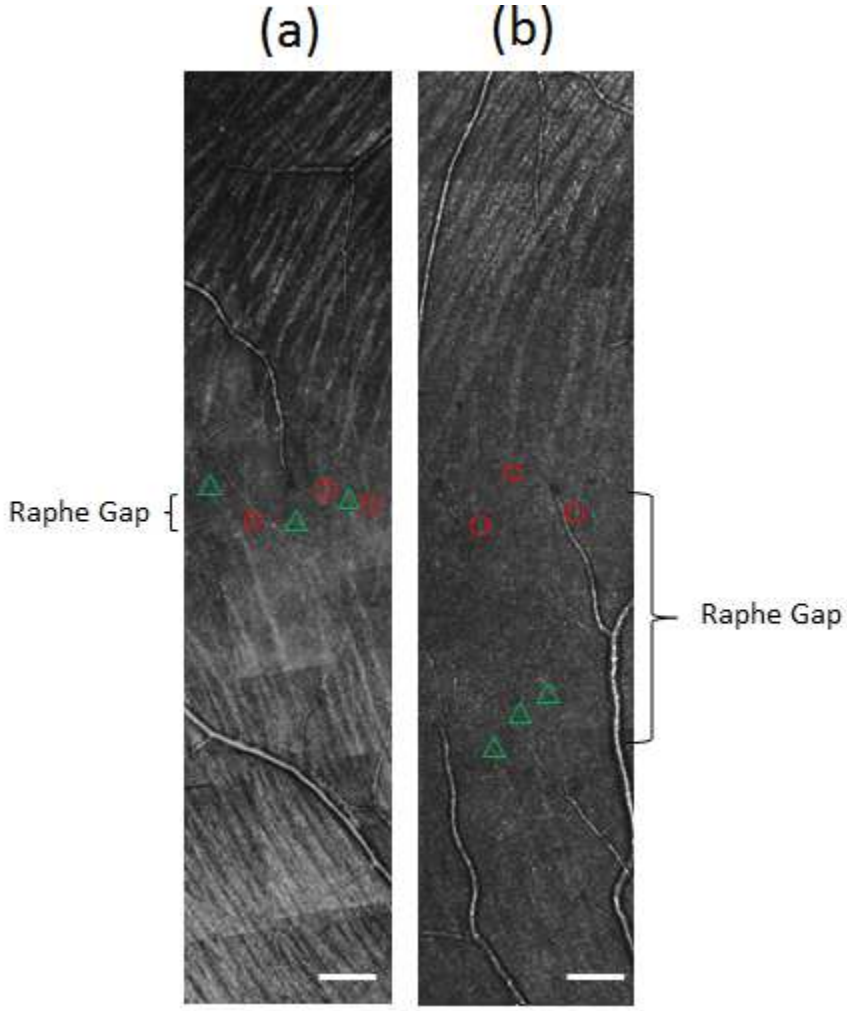

Figure 3. Example of nerve fiber imaging and the raphe gap measurements in a normal and glaucomatous eye. (a) AOSLO montage of the temporal raphe in a control subject. (b) A raphe image from a patient with a nasal step. Contrast of these two montages was adjusted to further enhance the visualization of bundles for readers. The total deviation (TD) of field sensitivity was -0.67 dB corresponding to the superior part of the montage where the nerve fiber bundles are still visible. The TD was -1.67 dB corresponding to the inferior part of the montage, where nerve fiber bundles are barely seen. The raphe gap in (b) is larger than in (a). For both images, the red circles, as marked by human graders,

represent visible ends of three longest RNFL superior bundles. The green circles represent the counterparts of inferior bundle. Scale bar: 200 μm.

2) Measurement of bundle reflectivity and density by bundle index

To evaluate the reflectivity and density of RNFL bundles, we developed an image descriptor we named the 'bundle index'. The bundle index captures the response of steerable first-order Gaussian derivative filters (Freeman & Adelson, 1991) (see Figure 4). These filters are designed for extracting oriented edge contrast in an image and thus are suitable to extract the relative reflectivity of oriented RNFL bundle patterns by computing the contrast between the bundle area and its adjacent non-bundle area. Information about density of RNFL bundles can be incorporated by integrating these filters' responses over a larger region.

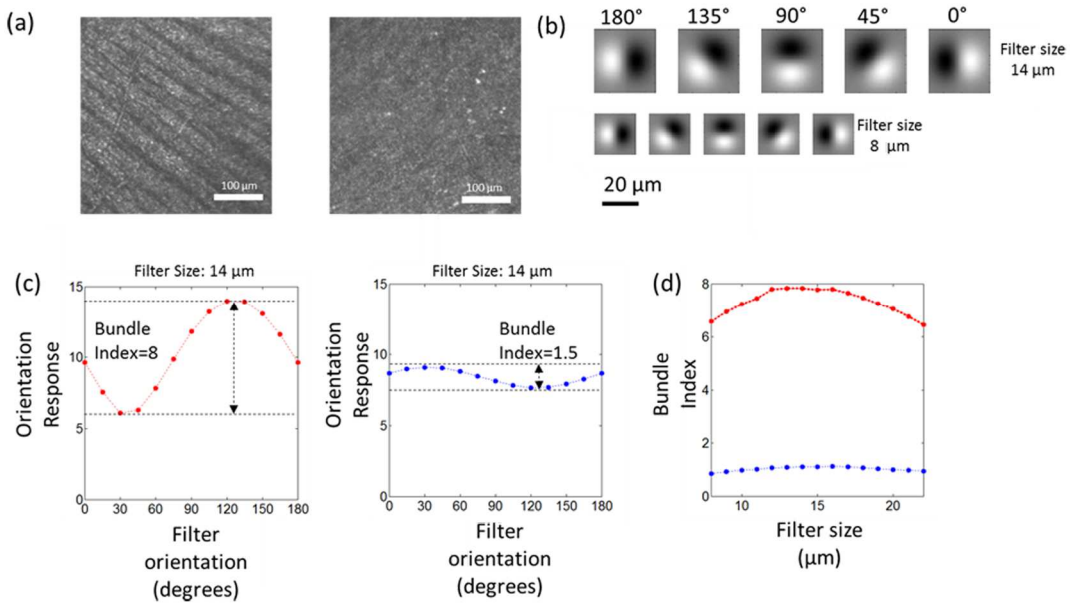

Figure 4. Illustration of bundles index computation. (a) Two RNFL images. Nerve fiber bundles are reflective in the left image and barely recognizable in the right image. (b) The spatial profiles for two sets of steerable Gaussian filters with two different sizes. See text for definition of filter size. For illustration purpose, we only show five orientations of each set. (c) The orientation responses when the first filter set in (b) is convolved with each image in (a). See text for details of computation. The red line in the left graph represents the responses from the left image in (a), and the blue line in the right graph presents the responses from the right image in (a). The difference between the maximum and minimum orientation responses of each filter set is the bundle index for this filter set. (d) The bundle index changes across all filter sizes for both images in (a). The red curve on the top corresponds to the left image in (a). The blue one corresponds to the right

image in (a). The maximum bundle index across filter sizes is used for further quantitative analysis.

While absolute reflectivity seems a more direct descriptor for bundles, in practice the absolute reflectivity would be affected by a number of factors that are difficult to control during imaging. Two obvious factors are media clarity in aging eyes and illumination power difference between different imaging sessions. In contrast, relative reflectivity has the advantage that it essentially normalizes for some of these individual sources of variation, by comparing the relative reflectivity of bundles with adjacent non-bundle areas. If we assume that non-bundle regions are not affected by glaucoma, then relative reflectivity is directly related to absolute reflectivity of bundles.

For a given RNFL region in AOSLO montages, we computed a bundle index in MATLAB using the following steps: 1) We created a set of steerable first-order 2D Gaussian filters containing 12 orientations (0 to 165° in 15° steps) at each of 15 spatial scales. The size of the filter is defined as the distance between the pixel of the most positive intensity and the pixel of the most negative intensity. The spatial scales of the filters were varied such that the size of the filters ranged from 8 to 22 μm in 1 μm steps. 2) Each set of filters was then convolved with the RNFL region, generating a filter response series for each pixel. Normalization was performed by dividing pixel responses over the averaged intensity of the local region that the filter was convolved with. 3) Pixels containing blood vessels or on boundaries between neighboring images were manually marked as invalid. Correspondingly, the filter responses obtained in the previous step in which these invalid pixels were involved were also marked as invalid to

reduce responses that are irrelevant to bundles. For image boundaries, the responses are high because we manually adjusted image brightness during montage construction, and therefore the brightness transition between neighboring images could be unsmooth, forming artificial contrast and high filter responses. 4) The response at each orientation for the whole region was then computed by averaging the responses of that orientation from all valid pixels within the region. 5) The bundle index for each size of filter was computed as the absolute difference between maximum and minimum orientation responses of that given size of filter. 6) The maximum bundle index across filter sizes was then employed as the bundle index for the region. Figure 4 presents two examples of this process. One example contains an image with highly-reflective bundles and the other with barely-visible bundles.

3) Measurement of RNFL and GCC thickness

For a given region in an OCT B-scan image, the boundaries of the RNFL and GCC were identified manually. The thickness of the RNFL and GCC for the region were then computed and averaged. To improve the reliability of measurements, we had two graders independently make the segmentation and averaged the results.

4) Visual field

For the 24-2 visual field, two test locations fall on the region that was imaged using the AOSLO imaging: the one at 9° nasal, 3° superior field, and the one at 9° nasal, 3° inferior field.

For each subject, we computed total deviation (TD) for each of these two test locations by averaging the TDs for that location from three visual field tests over an interval of approximately 6 months. To compare the field loss with the raphe gap, we further averaged the values of these two test locations for each studied eye because only one raphe gap was obtained for the corresponding region. In particular, for each studied eye, the antilog values of TD for these two locations were averaged, and then logged. This logged value was defined as averaged field loss. This computation was consistent with how other studies calculated averaged TD over regions (Hood, Anderson, Wall, & Kardon, 2007; Hood & Greenstein, 2003; Hood & Kardon, 2007; Hood & Zhang, 2000).

Statistics

We used both unpaired t-tests and Mann-Whitney U tests to compare the bundle index, RNFL thickness, GCC thickness and raphe gap between the patients and controls. To minimize Type 1 errors when using multiple tests, a P value of 0.0125 was used for statistical significance. Two-way random Intraclass Correlation Coefficient (ICC) with absolute agreement was used to assess the reliability of measurements of RNFL thickness, GCC thickness as well as raphe gap(Shrout & Fleiss, 1979).

5.3 Results

Difference in RNFL appearance between glaucomatous and control eyes

The appearance of the RNFL differed between control and glaucomatous eyes. In control eyes, nerve fiber bundles were highly reflective and readily distinguished from the spaces between bundles. In contrast, bundles in glaucomatous eyes were often less crisp in

appearance and the boundaries with the spaces between bundles were less sharply defined. The raphe gap in glaucomatous eyes appeared different from control subjects, with a notable lack of nerve fiber bundles near the raphe, although they could often be seen further from the raphe (Figure 5). Within the raphe gap, we did not see any reflective source, other than blood vessels, that showed reflectance comparable to the reflectance of bundles.

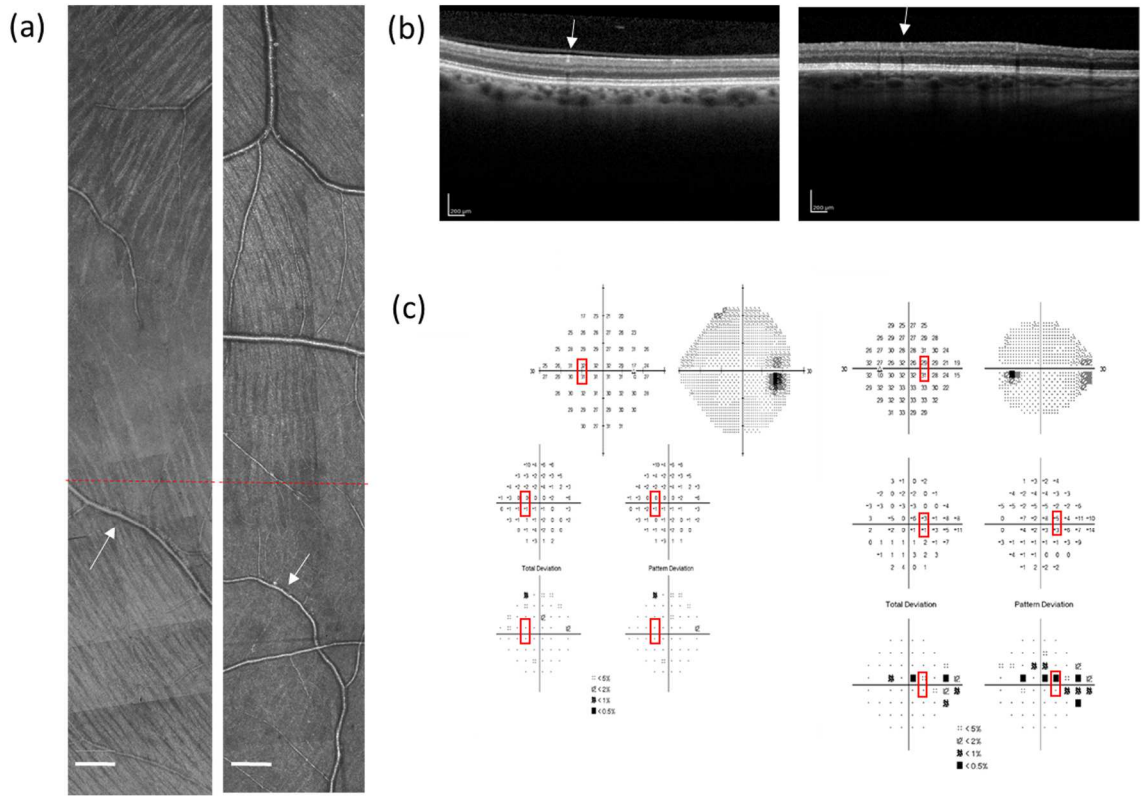

Figure 5. Example of AOSLO montages, OCT images and visual fields from two subjects. (a) RNFL montages constructed from AOSLO images. The left image is from a control subject and the right from a patient, where bundles are barely observed in the lower half of the image. Red dashed lines in both montages indicate the horizontal midline. Scale bar: 200 μm. (b) OCT images in the same region. Left is from the control and the right is from the patient. The white arrows in (a) and (b) point to the same vessels in AO montages and OCT images. (c) Corresponding 24-2 visual field reports. Left and right are from the control and the patient respectively. For the control, the averaged TD over three reports (visits) was -0.67 dB at 9° nasal, 3° superior field, and -1

dB at 9° nasal, 3° inferior field. For the patient, the corresponding averaged TD over three reports (visits) was -2.33 dB at 9° nasal, 3° superior field, and -0.33 dB at 9° nasal, 3° inferior field. Red boxes indicate testing locations that fall within the region of the AOSLO imaging.

Quantitative Differences between glaucomatous and control eyes.

The averaged field loss, which is the average of the total 6 visual-field points in three visual-field reports, as defined above, was lower in the patient group than in the control group (-1.48 ± 1.13 dB, as opposed to 0.18 ± 0.65 dB; t-test P = 0.002, Mann-Whitney U test P=0.005). The raphe gap was larger in glaucomatous eyes than control eyes (585.1 ± 281.3 μm, versus 230.8±107.2 μm; t-test P< 0.0001, Mann-Whitney U test P=0.001). The bundle index was smaller in glaucomatous eyes than control eyes (2.8 ± 1.9, versus

4.9 ± 1.9; t-test P = 0.0025, Mann-Whitney U test P=0.004). RNFL thickness as measured with OCT was thinner in glaucomatous eyes than control eyes (20.38 ± 5.24 μm, versus 23.324 ± 3.07 μm; t-test P=0.032, Mann-Whitney U test P=0.087). GCC thickness was thinner in glaucomatous eyes than controls (68.56 ± 25.20 μm, versus 80.16 ± 18.28 μm; t-test P<0.0001, Mann-Whitney U test P=0.0001). The ICC was 0.96 (95% CI 0.88 to 0.98) for measurements of raphe gap, 0.73 (95% CI 0.53 to 0.85) for measurements of RNFL thickness, and 0.95 (95% CI 0.90 to 0.97) for measurements of GCC thickness. The mean measurement difference between the two graders was 4.52± 44.71 μm for measurements of the raphe gap, 0.04 ± 0.84 μm for RNFL thickness, and 0.13 ± 0.81 μm for GCC thickness.

The raphe gap was larger for patients with greater field loss, as shown in Figure 6(a). 8 out of nine eyes showed larger raphe gaps than all the control eyes. The bundle index, RNFL thickness, and GCC thickness exhibit large individual variability between subjects, as shown in Figure 6(b-d). For 2 glaucomatous eyes with more than -5 dB total deviation, results of all these measurements were smaller than ones for all other glaucomatous eyes as well as control eyes.

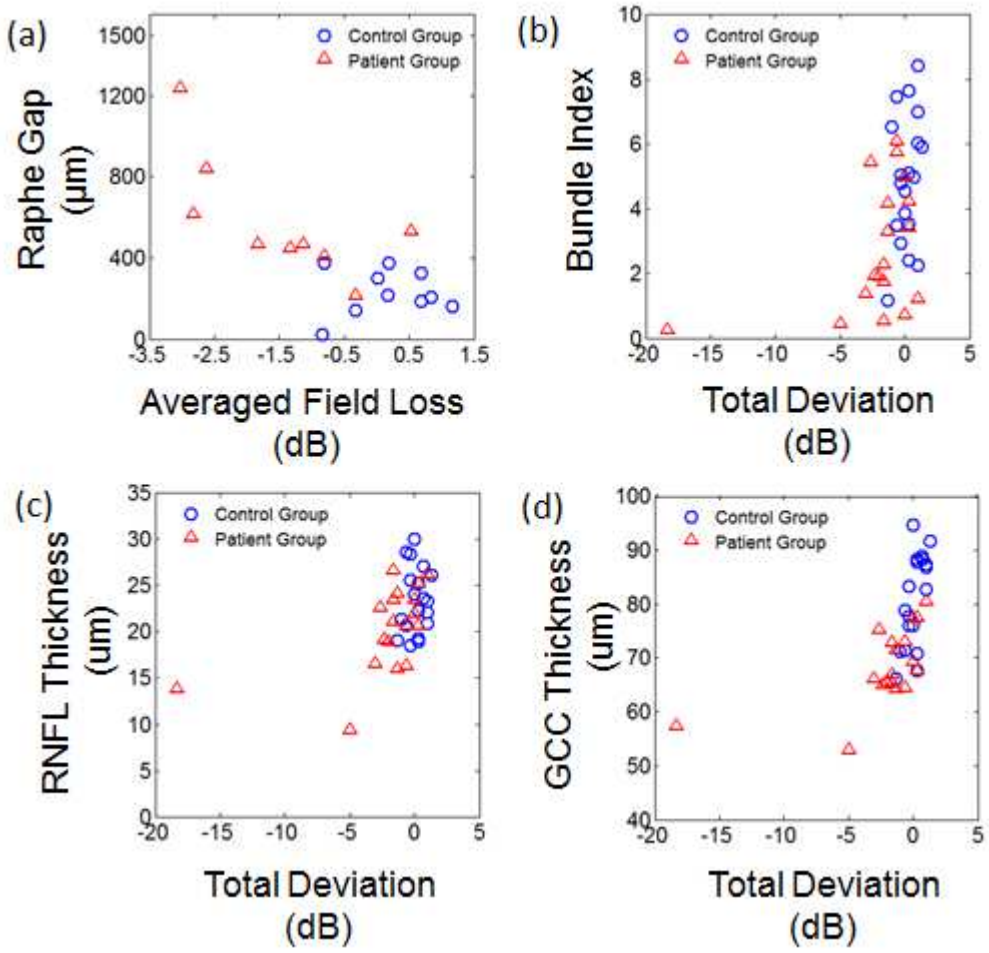

Figure 6. Comparison of imaging measurements to local visual field results. (a) Raphe gap as a function of averaged field loss. (b) Bundle index as a function of total deviation. (c) RNFL thickness as a function of total deviation. (d) GCC thickness as a function of total deviation. Blue circles represent data of the controls and the red triangles represent data of the patients with glaucoma. The two groups in (a), (b), and (d) are significantly different, with p values less than the alpha level 0.0125.

5.4 Discussion

The results of the study provide evidence that structural changes occur to the temporal raphe even when local functional loss is mild. While the decreased bundle index taken alone could be explained by either decreased reflectivity or low density of remaining bundles, the enlarged raphe gap and reduced GCC thickness suggest that there is a loss of the bundles and ganglion cells in this area. More importantly, we found statistically significant differences in three out of four measurements, even when the local TD of the field sensitivity was relatively small and subject number for the study was small. In particular, the enlarged raphe gap was found in eight out of nine glaucomatous eyes with local averaged field loss no worse than -3.5 dB.

Finding statistically differences between these two small groups can be partially attributed to the fact that ganglion cell axons are close to their cell bodies in the temporal raphe, and therefore visual field sensitivities can be mapped more accurately to the RNFL arising from ganglion cells with receptive fields in this region and have more direct relation to structural changes.

The three measurements that showed statistically significant differences between control and patient groups each have their own strengths and weakness. The lack of detectable non-vessel residual tissue within the increased raphe gap suggests that measuring the raphe gap in *en face* plane is relatively insensitive to effects of RNFL remnants. It has been shown that, for eyes under conditions of severe field loss, the residual RNFL thicknesses in the peripapillary region were still about 33% or more of the

mean values for healthy eyes(Hood & Kardon, 2007), and showed considerable variation between individuals. This could further complicate the evaluation of loss in RNFL thickness around the optic disc in patients with glaucoma. In contrast, this did not become a challenge for evalution of the raphe gap.

While there are various possible reasons for this, we suggest that the RNFL in the temporal raphe, which is thinner than in most of the retina, has a lower requirement for the support from glial cells. This can be supported by the histological finding that astrocytes, which are a major glial component of RNFL bundles (Bussow, 1980; Ogden, 1978, 1983; Trivino, Ramirez, Salazar, Ramirez, & Garcia-Sanchez, 1996), were found at high density near the optic disc region while its density fell when the RNFL becomes thin (Ogden, 1978; Reichenbach, 1987; Stone & Dreher, 1987).

In contrast to the raphe gap which describes only one property of the RNFL, the bundle index combines multiple properties of the RNFL into only one number. This is because theoretically the AOSLO with a proper optical configuration can achieve an axial resolution of approximately 50-75 μm (Gray et al., 2008; Venkateswaran, Roorda, & Romero-Borja, 2004). This axial range is slightly larger than or equal to the RNFL thickness in this region. As a result, pixels in AOSLO images may contain information about both bundle intrinsic properties and bundle density along the depth. During bundle index computation, we integrated filter responses over a region, which further incorporated information on *en face* bundle density providing us with a descriptor which, while localized, still incorporated information averaged over a region of RNFL in all three dimensions. An obvious tradeoff for this measurement is that we are not able to

decouple changes in individual properties of the RNFL. Future studies are needed to explore the optimal use of the index.

Compared to the first two measurements that only reflect changes in the RNFL, the measurement of the GCC adds information about ganglion cells and has potential to explore how ganglion cells are impacted in this region in future studies.

Compared to the GCC measurement, measuring the thickness of the RNFL is relatively challenging. RNFL thickness corresponded to only 4 to 8 pixels in OCT images of the control group, and the averaged thickness difference between the two groups was only about 4 microns, which was equivalent to ~1 pixel in images. Therefore RNFL thickness measurements exhibited a limited dynamic range. Even worse, the contrast of the RNFL layer relative to ganglion cell layer was low, which further increases the difficulty of RNFL segmentation. To increase the accuracy of measuring RNFL thickness changes, an OCT imaging system with higher axial resolution is necessary.

The between-subject variability of the bundle index as well as RNFL and GCC thickness in our control group was large. This could be partially attributed to the fact that we compared locations at equal distances above and below the horizontal midline of the retina, but there is considerable between-subject variability in how far the raphe deviates from the horizontal midline of the retina (Chauhan et al., 2014; Huang et al., 2014). Future studies are warranted to investigate how the raphe's deviation from the horizontal midline affects the variability of the measurements.

Our study was restricted to only a small portion of the raphe due to the small imaging fields of the current AOSLO. This could be improved by using an AOSLO with larger field (Mujat, Ferguson, Iftimia, & Hammer, 2009). Also, it is worth pointing out that AOSLO is not the only means to image the RNFL in the raphe. The improved *en face* OCT technique is able to extract *en face* information of the temporal raphe (Chauhan et al., 2014), although *en face* resolution of OCT is lower than AOSLO. Future research is needed to explore and compare the capabilities of both imaging approaches for glaucoma assessment.

In conclusion, structural changes occur to the temporal raphe even when local functional loss is mild. These changes can be visualized and measured using high-resolution imaging techniques and proper metrics. The study opens the possibility of using the temporal raphe as a site for glaucoma research and clinical assessment.

5.5 Appendix

5.5.1 Analysis of AOSLO imaging resolution

The visibility of bundles in AO images can be affected by imaging resolution. To ensure the loss of nerve fiber bundles we observed in patients was not primarily caused by poor imaging resolution in the eyes, we estimated imaging resolution using at least one of the two following ways.

First, we used small vessels and moving blood cells in the AOSLO videos to estimate imaging resolution. These smaller vessels and blood cells are generally smaller than nerve fiber bundles near the temporal raphe. Hence, they require higher imaging resolution than what is needed for bundles. In all patients we tested, we were able to observe small vessels and individual blood cells in the same videos of imaging nerve fiber bundles. Seeing these details indicates that imaging resolution was enough to image bundles if they exist. Examples of individual vessels and blood cells, and estimation of corresponding imaging resolution are shown in Figure 7. Examples of small vessels were also presented in Figure 2, 3, and 5.

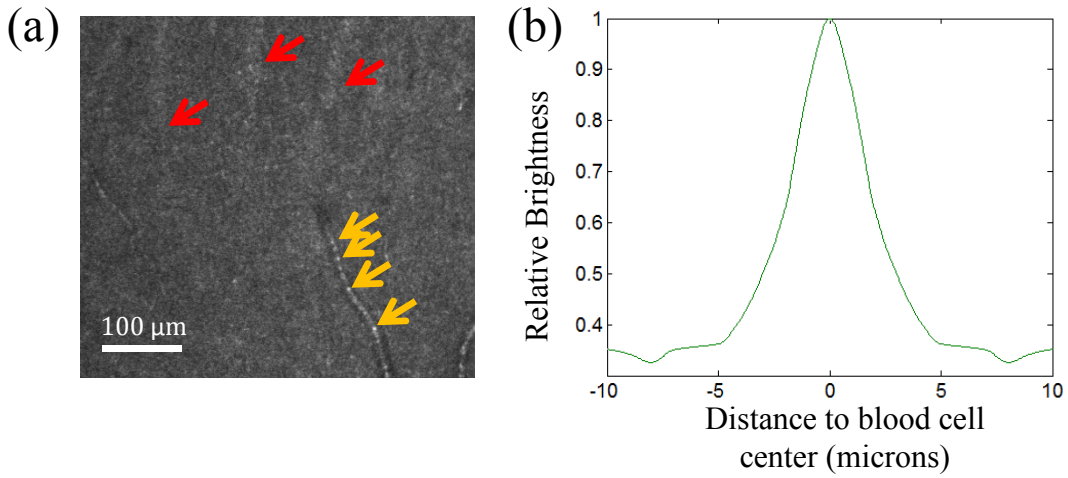

Figure 7(a) Small vessels and individual blood cells were observed within a single frame of an AOSLO video. Yellow arrows point to individual cells within a vessel. Red arrows point to individual bundles near the vessel. This video imaged the raphe gap of a subject, whose RNFL montage was shown in Figure 3(b) in the previous section 5.2. (b) The averaged reflectance profile for the four blood cells, which are indicated by yellow arrows, is displayed in the left panel. The profile was created in the following way: For each selected cell, a 20-by-20-pixel window centered at the cell center was extracted. The windows of these cells were aligned and averaged along all meridians, resulting in a 1-dimensional reflectance profile. We then normalized the profile with its central peak, and smoothed it with a Gaussian filter. Full width of half maximum intensity of this profile was about 5 µm, and full width of the profile is about 10 µm. This, when

combined with the fact that the diameter of a red blood cell is about 6-8 μm (Price-Jones, 1910, 1920), indicates that imaging resolution for this image is about 5 μm or less.

Another way of estimating resolution is analysis of images of photoreceptors in the same eyes. Photoreceptors in this region are generally smaller than bundles, requiring higher resolution to image than bundles. Figure 8 shows one of these cone photoreceptor images from a subject in the study. We performed an analysis similar to that for Figure 7 (b) to estimate the resolution. The resolution was similar to what we obtained in the analysis of blood cells. In practice, we only performed photoreceptor imaging on a few patients, because photoreceptors reside in a deeper layer than the RNFL and therefore require additional imaging acquisition, which extended imaging time for subjects.

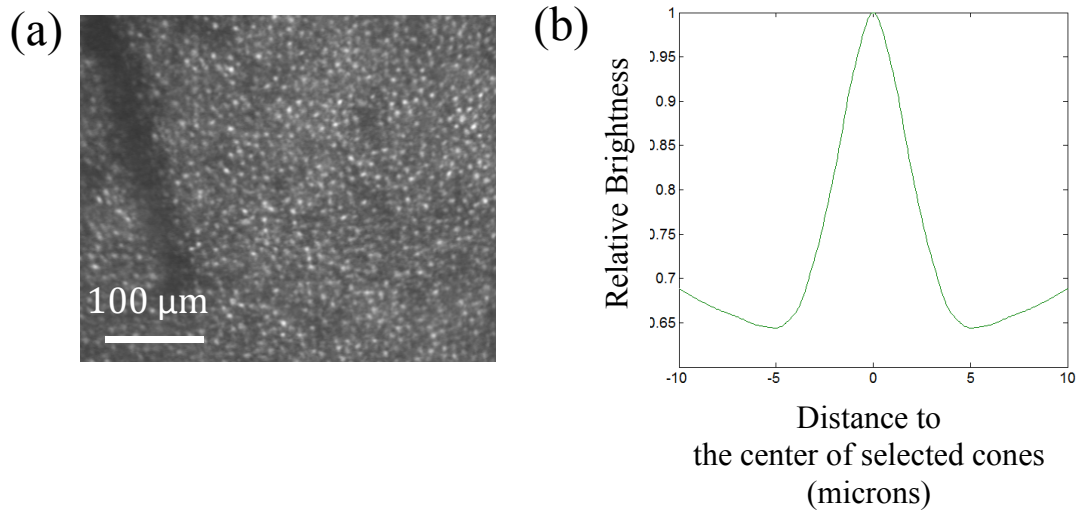

Figure 8. (a) A processed cone photoreceptor image of a patient with glaucoma. Bright cells in the image are individual cones. (b) An averaged reflectance profile for cones in the image on the left. In particular, 10 cones were randomly selected in the image. Their corresponding reflectance profiles were extracted and processed in the same way we did for Figure 7 (b). The full width at maximum intensity of this profile is about 4 microns, and full width is about 9 µm. Given the diameter of cones in this region is about 6-8 µm, the imaging resolution is about 4 µm or less.

5.5.2 Imaging operations by human operators

What were unavoidable for AOSLO imaging were subjective imaging adjustments by human operators. During imaging, operators often need to adjust several parameters of AOSLO systems to optimize the imaging quality. The two most common adjustments are the focus of the system and the gain of the detector. Although these two adjustments can generally improve imaging quality, they are adjusted based on image quality perceived by operators, which could be subjective and introduce variation of imaging conditions between different imaging sessions.

To reduce the side-effects of subjective adjustments, we set up several objective rules for adjustments in the study. For adjustments of focus, operators needed to start the focus at the most inner surface of the retina where bundles was barely seen, and gradually shifted the focus deeper until the focus reached a zone where operators saw the best reflectance of bundles and where the reflectance was insensitive to minor focusing adjustments (e.g., ±0.08 diopters). The zone existed because of the large depth of focus of the AOSLO. Specifically, given a 6mm pupil, the AOSLO's axial resolution is usually around 50-75um, larger than the whole depth of the RNFL in this region. This large depth of focus would allow for minor focus deviation off the optimal focus with minimum effects on reflectance seen in images.

For the diseased regions where bundles had low visibility and therefore the optimal focus was hard to be determined, operators started with the imaging of neighboring regions where bundles were well observed, and then applied similar focusing power back

to the diseased regions. This rule is based on an assumption that there is no disrupt depth/thickness changes for the RNFL in this region.

As for adjustment of gains of a detector, operators were allowed to adjust the gain to help find bundles. However, when operators acquire videos/images, the gain must be set back to be a standard value to ensure a uniform gain setting across the subjects in the study. This standard gain was 210-volt voltage for the APD module (C30659-900-R8AH, Excelitas Inc, USA), comparable to gains used for all previous studies that employed the same AOSLO system (Zou, Qi, & Burns, 2011).

Nevertheless, future studies are warrantied to investigate approaches of objectively evaluating image quality in real-time, which can further reduce variation of imaging conditions between imaging sessions.

5.5.3 Procedure of Identification of bundles during subjective grading

To identify a bundle in AOSLO montages, a grader traced a bundle from the furthest superior or inferior side of the montage, where bundles often show best reflectance, and then the grader followed the trajectory of the bundle all way to the bundle's tip near the raphe.

5.5.4 Unknown features within the raphe gap

Within the raphe gap we still observed features that did not look like bundles. Their reflectance was generally weak. One possible origin of these features is the reflectance

returned from underlying layers, like GCC, because the axial resolution of the AOSLO is larger than the whole depth of the RNFL. Future studies are warrantied to evaluate the reproducibility of the results in the study.

5.5.5 Reproducibility of imaging and image analysis

This is one of the limitations of the study. Given limited time we had for each subject, we did not image the same region twice if imaging quality was acceptable. Therefore there was no enough data to investigate reproducibility of results. This would be an interesting study for the future.

5.5.6 Variation of the four quantitative measurements:

The four types of measurements in the previous sections of this chapter seemed exhibit considerable variation. To explore which measurement has the least variation, we computed coefficients of variance (CV) using data from the control group. The CV was 0.14 for RNFL thickness, 0.10 for GCC thickness, 0.39 for bundle index, and 0.47 for the raphe gap respectively. This suggests that, although the latter three measurements that showed statistically significant difference between the control and patient groups, the variation of the data actually compromises their sensitivity. Future studies are warrantied to identify and reduce sources of data variation, and further improve the sensitivity of these measurements.

5.5.7 Comparisons between bundle index, RNFL thickness and GCC thickness

Since bundle index, GCC thickness, RNFL thickness are all structural measurements, we further explore the relations between them. A weak correlation was found between the bundle index and GCC thickness measurement, as shown in Figure 9(b). As the bundle index decreases, the GCC thickness decreases as well. This correlation can be explained by structural loss occurring in both the RNFL and GCC. The R square (0.28) was small, possibly because these two measurements are focused on different physical properties of ganglion cells, and these properties are not necessarily linearly related.

5.5.8 Confounding effects of age

It is well known that aging can affect various physical properties of human retina. Since all the subjects were senior adults in the study, aging effects on all the measurements was explored with linear regression. RNFL thickness, GCC thickness or raphe gap did not show significant linear relations with age. A larger sample pool would be needed to further test their relations with age.

A weak correlation was found between the bundle index and age, as shown in Figure 9(c). It indicates aging may decrease the reflectance of bundles. Given the small sample size of the study, future studies are warrantied to confirm this relation.

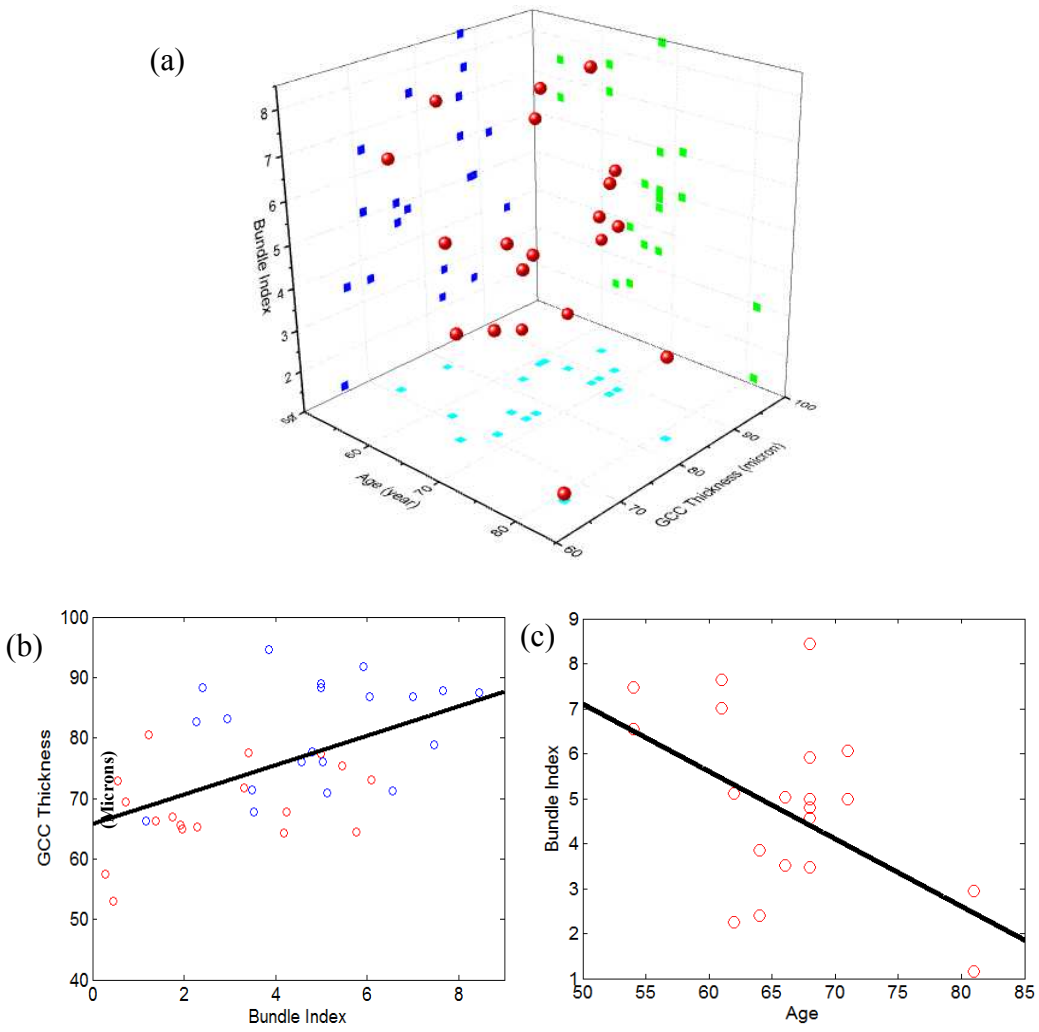

Figure 9. Relation between bundle index, GCC thickness and Age. (a) A 3D plot for bundle index, GCC thickness and age. The blue, green and cyan squares represent corresponding 2D projections in the three planes respectively (GCC thickness vs Bundle Index, Bundle index vs Age, Age versus GCC thickness). (b) Relation between GCC thickness and bundle index. The slope of the regression line is 2.43, and R square is 0.28. (c) Relation between the bundle index and age. The slope of the regression line is 0.14, and R square 0.27.

5.5.9 Bundle Index map

To explore how the bundle index varies across the raphe, we developed the bundle index map based on the bundle index. For an AOSLO montage, we created a window of 300 μm by 300 μm, and moved it at the step of 30 μm across the whole montage. At each step, we computed the bundle index of the region within the window. In the end, all these bundle indices were registered into a map based on their relative spatial locations. Two examples of the bundle index map were shown in Figure 10. The bundle index within the raphe gap in the bundle index map was in the same order of the index in regions of glaucomatous damage shown in previous sections of this chapter. This opens a possibility of using the bundle index to grade the raphe gap objectively.

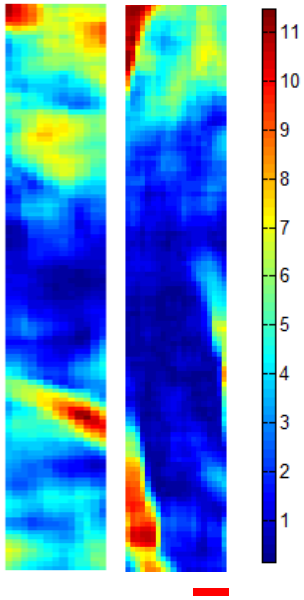

Figure 10. Bundle index maps. (Left) Bundle index map for figure 3(a). (Right) Bundle index map for figure 3(b). The red scale bar represents 200 µm. Both maps are 150 µm smaller on each side than their original montages because of the window size we set up for computation of the bundle index map. In addition, for display purpose, the vessels' responses were reserved in the map. These responses, however, were excluded from all related analysis in previous sections 5.2-5.4.

5.6 Acknowledgements

The work was supported by NIH Grants R01 EY04395, R01 P30EY019008, R01 EY007716, and R01 EY024542.

5.7 References

Airaksinen, P. J., & Alanko, H. I. (1983). Effect of retinal nerve fibre loss on the optic nerve head configuration in early glaucoma. *Graefes Arch Clin Exp Ophthalmol, 220*(4), 193-196.

Airaksinen, P. J., Drance, S. M., Douglas, G. R., Mawson, D. K., & Nieminen, H. (1984). Diffuse and localized nerve fiber loss in glaucoma. *Am J Ophthalmol, 98*(5), 566-571.

Airaksinen, P. J., Drance, S. M., Douglas, G. R., Schulzer, M., & Wijsman, K. (1985). Visual field and retinal nerve fiber layer comparisons in glaucoma. *Arch Ophthalmol, 103*(2), 205-207.

Anton, A., Yamagishi, N., Zangwill, L., Sample, P. A., & Weinreb, R. N. (1998). Mapping structural to functional damage in glaucoma with standard automated perimetry and confocal scanning laser ophthalmoscopy. *Am J Ophthalmol, 125*(4), 436-446. doi: Doi 10.1016/S0002-9394(99)80183-4

Armaly, M. F. (1971). Visual field defects in early open angle glaucoma. *Trans Am Ophthalmol Soc, 69*, 147-162.

Artes, P. H., Iwase, A., Ohno, Y., Kitazawa, Y., & Chauhan, B. C. (2002). Properties of perimetric threshold estimates from Full Threshold, SITA Standard, and SITA Fast strategies. *Invest Ophthalmol Vis Sci, 43*(8), 2654-2659.

Bussow, H. (1980). The astrocytes in the retina and optic nerve head of mammals: a special glia for the ganglion cell axons. *Cell and Tissue Research, 206*(3), 367-378.

Chauhan, B. C., Sharpe, G. P., & Hutchison, D. M. (2014). Imaging of the Temporal Raphe with Optical Coherence Tomography. *Ophthalmology*. doi: 10.1016/j.ophtha.2014.06.023

Chen, M. F., Chui, T. Y., Alhadeff, P., Rosen, R. B., Ritch, R., Dubra, A., & Hood, D. C. (2015). Adaptive optics imaging of healthy and abnormal regions of retinal nerve fiber bundles of patients with glaucoma. *Invest Ophthalmol Vis Sci, 56*(1), 674-681. doi: 10.1167/iovs.14-15936

Curcio, C. A., & Allen, K. A. (1990). Topography of Ganglion-Cells in Human Retina. *Journal of Comparative Neurology, 300*(1), 5-25. doi: DOI 10.1002/cne.903000103

Denniss, J., Turpin, A., & McKendrick, A. M. (2014). Individualized structure-function mapping for glaucoma: practical constraints on map resolution for clinical and research applications. *Invest Ophthalmol Vis Sci, 55*(3), 1985-1993. doi: 10.1167/iovs.13-13758

Drasdo, N., Millican, C. L., Katholl, C. R., & Curcio, C. A. (2007). The length of Henle fibers in the human retina and a model of ganglion receptive field density in the visual field. *Vision Res, 47*(22), 2901-2911. doi: DOI 10.1016/j.visres.2007.01.007

Dreher, A. W., & Reiter, K. (1992). Retinal Laser Ellipsometry - a New Method for Measuring the Retinal Nerve-Fiber Layer Thickness Distribution. *Clinical Vision Sciences, 7*(6), 481-&.

FitzGibbon, T., & Taylor, S. F. (2012). Mean retinal ganglion cell axon diameter varies with location in the human retina. *Jpn J Ophthalmol, 56*(6), 631-637. doi: 10.1007/s10384-012-0185-9

Freeman, W. T., & Adelson, E. H. (1991). The Design and Use of Steerable Filters. *IEEE Trans Pattern Anal Mach Intell, 13*(9), 891-906. doi: Doi 10.1109/34.93808

Garway-Heath, D. F., Poinoosawmy, D., Fitzke, F. W., & Hitchings, R. A. (2000). Mapping the visual field to the optic disc in normal tension glaucoma eyes. *Ophthalmology, 107*(10), 1809-1815. doi: Doi 10.1016/S0161-6420(00)00284-0

Gray, D. C., Wolfe, R., Gee, B. P., Scoles, D., Geng, Y., Masella, B. D., . . . Merigan, W. H. (2008). In vivo imaging of the fine structure of rhodamine-labeled macaque retinal ganglion cells. *Invest Ophthalmol Vis Sci, 49*(1), 467-473. doi: 10.1167/iovs.07-0605

Hart, W. M., Jr., & Becker, B. (1982). The onset and evolution of glaucomatous visual field defects. *Ophthalmology, 89*(3), 268-279.

Heijl, A., Lindgren, A., & Lindgren, G. (1989). Test-retest variability in glaucomatous visual fields. *Am J Ophthalmol, 108*(2), 130-135.

Hood, D. C., Anderson, S. C., Wall, M., & Kardon, R. H. (2007). Structure versus function in glaucoma: an application of a linear model. *Invest Ophthalmol Vis Sci, 48*(8), 3662-3668. doi: 10.1167/iovs.06-1401

Hood, D. C., & Greenstein, V. C. (2003). Multifocal VEP and ganglion cell damage: applications and limitations for the study of glaucoma. *Prog Retin Eye Res, 22*(2), 201-251.

Hood, D. C., & Kardon, R. H. (2007). A framework for comparing structural and functional measures of glaucomatous damage. *Prog Retin Eye Res, 26*(6), 688-710. doi: 10.1016/j.preteyeres.2007.08.001

Hood, D. C., & Zhang, X. (2000). Multifocal ERG and VEP responses and visual fields: comparing disease-related changes. *Doc Ophthalmol, 100*(2-3), 115-137.

Hoyt, W. F., Frisen, L., & Newman, N. M. (1973). Fundoscopy of nerve fiber layer defects in glaucoma. *Invest Ophthalmol, 12*(11), 814-829.

Huang, G., Gast, T. J., & Burns, S. A. (2014). In-vivo Adaptive Optics imaging of the temporal raphe and its relationship to the optic disc and fovea in the human retina. *Invest Ophthalmol Vis Sci*. doi: 10.1167/iovs.14-14893

Huang, G., Qi, X., Chui, T. Y., Zhong, Z., & Burns, S. A. (2012). A clinical planning module for adaptive optics SLO imaging. *Optom Vis Sci, 89*(5), 593-601. doi: 10.1097/OPX.0b013e318253e081

Jansonius, N. M., Schiefer, J., Nevalainen, J., Paetzold, J., & Schiefer, U. (2012). A mathematical model for describing the retinal nerve fiber bundle trajectories in the human eye: average course, variability, and influence of refraction, optic disc size and optic disc position. *Exp Eye Res, 105*, 70-78. doi: 10.1016/j.exer.2012.10.008

Lamparter, J., Russell, R. A., Zhu, H., Asaoka, R., Yamashita, T., Ho, T., & Garway-Heath, D. F. (2013). The influence of intersubject variability in ocular anatomical

variables on the mapping of retinal locations to the retinal nerve fiber layer and optic nerve head. *Invest Ophthalmol Vis Sci, 54*(9), 6074-6082. doi: 10.1167/iovs.13-11902

Lee, A. J., Wang, J. J., Rochtchina, E., Healey, P., Chia, E. M., & Mitchell, P. (2003). Patterns of glaucomatous visual field defects in an older population: the Blue Mountains Eye Study. *Clin Experiment Ophthalmol, 31*(4), 331-335.

Liang, J., Williams, D. R., & Miller, D. T. (1997). Supernormal vision and high-resolution retinal imaging through adaptive optics. *J Opt Soc Am A Opt Image Sci Vis, 14*(11), 2884-2892.

Mujat, M., Ferguson, R. D., Iftimia, N., & Hammer, D. X. (2009). Compact adaptive optics line scanning ophthalmoscope. *Opt Express, 17*(12), 10242-10258.

Ogden, T. E. (1978). Nerve fiber layer astrocytes of the primate retina: morphology, distribution, and density. *Invest Ophthalmol Vis Sci, 17*(6), 499-510.

Ogden, T. E. (1983). Nerve fiber layer of the primate retina: thickness and glial content. *Vision Res, 23*(6), 581-587.

Ogden, T. E. (1984). Nerve-Fiber Layer of the Primate Retina - Morphometric Analysis. *Invest Ophthalmol Vis Sci, 25*(1), 19-29.

Piltz, J. R., & Starita, R. J. (1990). Test-retest variability in glaucomatous visual fields. *Am J Ophthalmol, 109*(1), 109-111.

Price-Jones, C. (1910). The variation in the sizes of red blood cells. *Br Med J, 1910*, 1418-1419.

Price-Jones, C. (1920). The diurnal variation in the sizes of red blood cells. *Journal of Pathology and Bacteriology, 23*(4), 371-383. doi: DOI 10.1002/path.1700230402

Reichenbach, A. (1987). Quantitative and qualitative morphology of rabbit retinal glia. A light microscopical study on cells both in situ and isolated by papaine. *J Hirnforsch, 28*(2), 213-220.

Rohrschneider, K., Burk, R. O., Kruse, F. E., & Volcker, H. E. (1994). Reproducibility of the optic nerve head topography with a new laser tomographic scanning device. *Ophthalmology, 101*(6), 1044-1049.

Schuman, J. S., Hee, M. R., Arya, A. V., Pedut-Kloizman, T., Puliafito, C. A., Fujimoto, J. G., & Swanson, E. A. (1995). Optical coherence tomography: a new tool for glaucoma diagnosis. *Curr Opin Ophthalmol, 6*(2), 89-95.

Shrout, P. E., & Fleiss, J. L. (1979). Intraclass correlations: uses in assessing rater reliability. *Psychol Bull, 86*(2), 420-428.

Sommer, A., D'Anna, S. A., Kues, H. A., & George, T. (1983). High-resolution photography of the retinal nerve fiber layer. *Am J Ophthalmol, 96*(4), 535-539.

Stone, J., & Dreher, Z. (1987). Relationship between astrocytes, ganglion cells and vasculature of the retina. *J Comp Neurol, 255*(1), 35-49. doi: 10.1002/cne.902550104

Swanson, W. H., Malinovsky, V. E., Dul, M. W., Malik, R., Torbit, J. K., Sutton, B. M., & Horner, D. G. (2014). Contrast Sensitivity Perimetry and Clinical Measures of Glaucomatous Damage. *Optom Vis Sci*. doi: 10.1097/OPX.0000000000000395

Takayama, K., Ooto, S., Hangai, M., Ueda-Arakawa, N., Yoshida, S., Akagi, T., . . . Yoshimura, N. (2013). High-resolution imaging of retinal nerve fiber bundles in

glaucoma using adaptive optics scanning laser ophthalmoscopy. *Am J Ophthalmol, 155*(5), 870-881. doi: 10.1016/j.ajo.2012.11.016

Trivino, A., Ramirez, J. M., Salazar, J. J., Ramirez, A. I., & Garcia-Sanchez, J. (1996). Immunohistochemical study of human optic nerve head astroglia. *Vision Res, 36*(14), 2015-2028.

Venkateswaran, K., Roorda, A., & Romero-Borja, F. (2004). Theoretical modeling and evaluation of the axial resolution of the adaptive optics scanning laser ophthalmoscope. *J Biomed Opt, 9*(1), 132-138. doi: 10.1117/1.1627775

Weber, J., Dannheim, F., & Dannheim, D. (1990). The Topographical Relationship between Optic Disk and Visual-Field in Glaucoma. *Acta Ophthalmol, 68*(5), 568-574.

Werner, E. B., & Drance, S. M. (1977). Early visual field disturbances in glaucoma. *Arch Ophthalmol, 95*(7), 1173-1175.

Wirtschafter, J. D., Becker, W. L., Howe, J. B., & Younge, B. R. (1982). Glaucoma Visual-Field Analysis by Computed Profile of Nerve-Fiber Function in Optic Disk Sectors. *Ophthalmology, 89*(3), 255-267.

Wollstein, G., Garway-Heath, D. F., & Hitchings, R. A. (1998). Identification of early glaucoma cases with the scanning laser ophthalmoscope. *Ophthalmology, 105*(8), 1557-1563. doi: 10.1016/S0161-6420(98)98047-2

Yamagishi, N., Anton, A., Sample, P. A., Zangwill, L., Lopez, A., & Weinreb, R. N. (1997). Mapping structural damage of the optic disk to visual field defect in glaucoma. *Am J Ophthalmol, 123*(5), 667-676.

Zou, W., Qi, X., & Burns, S. A. (2011). Woofer-tweeter adaptive optics scanning laser ophthalmoscopic imaging based on Lagrange-multiplier damped least-squares algorithm. *Biomed Opt Express, 2*(7), 1986-2004. doi: 10.1364/BOE.2.001986

CHAPTER 6: CONCLUSIONS AND FUTURE DIRECTIONS

In this thesis, we demonstrated that AOSLO imaging can be used as a new approach to image and analyze the temporal raphe. In normal eyes, AOSLO imaging was able to visualize individual nerve fiber bundles and bundle trajectory over a relatively large region of the retina with a concentration on the structure of the temporal raphe. The results were comparable to *ex vivo* observations in the literature. In glaucomatous eyes with relatively mild local visual-field loss, AOSLO imaging was capable of showing structural difference of bundles compared to normal eyes.

Imaging and measurements of the temporal raphe indicated that structural changes in this region are sensitive enough to be measurable on an individual basis, rather than requiring large sample- size studies. This opens several new paths for glaucoma research.

First, given that most patients enrolled were observed with locally mild visual function losses, it would be valuable to test a large number of glaucomatous eyes with a wide range of damage severity in the same region of the retina. This would allow us to improve models of how the structural damage is related to functional loss from early stages to late stages of glaucoma.

Second, function-structure relations could be explored with better spatial resolution. We can improve resolution of functional measurements for the temporal raphe by using smaller stimuli and setting up denser testing locations for perimeters. Higher-resolution functional measurements could then be correlated with structural measurements obtained with AOSLO images, which allows us to estimate function-structure local relation more accurately than previously.

Third, assessing blood flow as well as vasculature in the temporal raphe would provide complimentary information to accompany structural measurements of the RNFL. Both blood flow and the integrity of vasculature are believed indicative of normality of retinal functions. Recent studies showed blood flow and vasculature in the optic disc region were reduced in glaucomatous eyes (Jia et al., 2014; Wang, Bower, Izatt, Tan, & Huang, 2008). However, how these parameters change in the temporal raphe remains unknown. Association of their changes with the structural changes in the same region could further our understanding of overall changes of the temporal raphe in glaucoma.

Fourth, we could relate glaucomatous damage in the temporal raphe to damage in other regions of the retina. RNFL changes in the optic disc, macular region, and other regions could also occur as the RNFL in the temporal raphe showed glaucomatous damage. For example, most patients in our study showed RNFL changes in the optic disc. Exploration of how these changes are related to each other could greatly advance our understanding of glaucoma progression.

All these future studies would benefit from improvement of imaging techniques. One direction for improvement is to develop an imaging instrument that offers a large imaging field as well as a resolution that is good enough to visualize RNFL bundles. For example, given the relatively large diameters of the RNFL bundles, it may be feasible to sacrifice the resolution of AOSLO imaging in exchange of wider imaging field. A wide-field AOSLO would reduce the imaging time by 3 or 4 folds while still being able to image bundles (Mujat, Ferguson, Iftimia, & Hammer, 2009). Alternatively, high-speed OCT is another approach to pursue in the near future. A regular OCT imaging has a relatively coarse *en face* sampling density because of its relatively slow speed. Recent development of OCT imaging enables an imaging speed that is at least 3-fold faster than previous ones (Huo et al., 2015; Kocaoglu, Turner, Liu, & Miller, 2014; Lu et al., 2013; Zhi, Qin, Wang, Wei, & Wang, 2015). Higher speed would enable acquiring a 3-dimensional high-resolution image volume in a relatively short time, and therefore it is possible to image the RNFL over a large region. All these new developments hold promise of measuring changes in the RNFL in an unprecedented resolution and speed, opening new paths to glaucoma research and clinical assessment.

References

Huo, T., Wang, C., Zhang, X., Chen, T., Liao, W., Zhang, W., . . . Xue, P. (2015). Ultrahigh-speed optical coherence tomography utilizing all-optical 40 MHz swept-source. *J Biomed Opt, 20*(3), 30503. doi: 10.1117/1.JBO.20.3.030503

Jia, Y., Wei, E., Wang, X., Zhang, X., Morrison, J. C., Parikh, M., . . . Huang, D. (2014). Optical Coherence Tomography Angiography of Optic Disc Perfusion in Glaucoma. *Ophthalmology*. doi: 10.1016/j.ophtha.2014.01.021

Kocaoglu, O. P., Turner, T. L., Liu, Z., & Miller, D. T. (2014). Adaptive optics optical coherence tomography at 1 MHz. *Biomed Opt Express, 5*(12), 4186-4200. doi: 10.1364/BOE.5.004186

Lu, C. D., Kraus, M. F., Potsaid, B., Liu, J. J., Choi, W., Jayaraman, V., . . . Fujimoto, J. G. (2013). Handheld ultrahigh speed swept source optical coherence tomography instrument using a MEMS scanning mirror. *Biomed Opt Express, 5*(1), 293-311. doi: 10.1364/BOE.5.000293

Mujat, M., Ferguson, R. D., Iftimia, N., & Hammer, D. X. (2009). Compact adaptive optics line scanning ophthalmoscope. *Opt Express, 17*(12), 10242-10258.

Wang, Y., Bower, B. A., Izatt, J. A., Tan, O., & Huang, D. (2008). Retinal blood flow measurement by circumpapillary Fourier domain Doppler optical coherence tomography. *J Biomed Opt, 13*(6), 064003. doi: 10.1117/1.2998480

Zhi, Z., Qin, W., Wang, J., Wei, W., & Wang, R. K. (2015). 4D optical coherence tomography-based micro-angiography achieved by 1.6-MHz FDML swept source. *Opt Lett, 40*(8), 1779-1782. doi: 10.1364/OL.40.001779

Gang Huang

Ph.D Student, Physiological Optics/Vision Science, Indiana University

800 East Atwater Drive, Bloomington, Indiana, USA, 47405

Phone: (812) 361-8096

Email: octhuang@gmail.com

Education

2008-2015, PhD, ***Physiological Optics/Vision Science***,

School of Optometry, Indiana University Bloomington

2009-2015, PhD minor, ***Computer Science***,

Department of Computer Science, Indiana University Bloomington

2002-2008, ***Information/Optical Engineering***,

Zhejiang University, China

Award

2006 Best Undergraduate Thesis Award

2008-2012 Fellowship, Indiana University Bloomington

2012 ARVO Student Travel Fellowship (ALCON)

2014 ARVO MIT Outstanding Poster Award

Skills

Optical Imaging System Design, Modelling, Prototyping, and Testing;

Software Development; Image Processing and Image Analysis;

Software Skills

Zemax, Solidworks, Matlab, C, Visual Basic, Java, C++;

Statview;

Publications

Huang G., Luo T., Gast T. J., Burns S. A., Malinovsky V. E., Swanson W. H. (2015). Imaging Glaucomatous Damage Across the Temporal Raphe. *Invest Ophthalmol Vis Sci, 56*(15). doi: 10.1167

Huang, G., Gast, T. J., & Burns, S. A. (2014). In vivo adaptive optics imaging of the temporal raphe and its relationship to the optic disc and fovea in the human retina. *Invest Ophthalmol Vis Sci, 55*(9), 5952-5961. doi: 10.1167/iovs.14-14893

Huang, G., Qi, X., Chui, T. Y., Zhong, Z., & Burns, S. A. (2012). A clinical planning module for adaptive optics SLO imaging. *Optom Vis Sci, 89*(5), 593-601. doi: 10.1097/OPX.0b013e318253e081

Huang, G., Zhong, Z., Zou, W., & Burns, S. A. (2011). Lucky averaging: quality improvement of adaptive optics scanning laser ophthalmoscope images. *Opt Lett, 36*(19), 3786-3788. doi: 10.1364/OL.36.003786

Zhong, Z., Huang, G., Chui, T. Y., Petrig, B. L., & Burns, S. A. (2012). Local flicker stimulation evokes local retinal blood velocity changes. *J Vis, 12*(6), 3. doi: 10.1167/12.6.3

Zou, W., Qi, X., Huang, G., & Burns, S. A. (2011). Improving wavefront boundary condition for in vivo high resolution adaptive optics ophthalmic imaging. *Biomed Opt Express, 2*(12), 3309-3320. doi: 10.1364/BOE.2.003309